University of California
Santa Barbara

Improving *Ab-Initio* Simulations of Ordering Phenomena in Transition Metal Alloys

A dissertation submitted in partial satisfaction
of the requirements for the degree

Doctor of Philosophy
in
Chemical Engineering

by

Elizabeth Decolvenaere

Committee in charge:

Professor Anton Van der Ven, Chair
Professor Michael Gordon, Co-Chair
Professor M. Scott Shell
Professor Michael Doherty

September 2017

The Dissertation of Elizabeth Decolvenaere is approved.

Professor M. Scott Shell

Professor Michael Doherty

Professor Michael Gordon, Committee Co-Chair

Professor Anton Van der Ven, Committee Chair

September 2017

Improving *Ab-Initio* Simulations of Ordering Phenomena in Transition Metal Alloys

by

Elizabeth Decolvenaere

In memory of my grandmother, Regina Decolvenaere

Acknowledgements

Words cannot express the depths of gratitude and appreciation I have for my advisor, Professor Anton Van der Ven. He has shown more patience, wisdom, and faith with me than I thought possible, and without his guidence and mentorship I would have burned out. He believed in me when even I'd given up and always found something amazing even when I thought my work was worthless. I am also deeply grateful for the advising of Professor Michael Gordon. Even as I began my strange walk from microplasma experimentalist to electronic structure theorist, he never doubted my abilities, and always pushed me to succeed.

In both my research groups I've enjoyed the support of some truly fantastic friends. John Goiri, Anirudh Natarajan, Jon Bechtel, and Ivy Chen, and Katie Mackie, it is only by the combined power of your sass and banter that I've survived this long. In both Van der Ven and Gordon groups I've found incredible support, and I'm going to miss everyone dearly.

From IRG 3 I enjoyed an extended network of much-appreciated guidence. The camradarie I've felt among the other students of the grop has been unparalleled, and seeing the project end is bittersweet. Michael "Moustache Mike" Gaultois, thank you for the pancakes and wisdom. Emily Levin, thank you for beliving in me. Professors Tresa Pollock, Carlos Levi, and Chris Palmstrom, and especially Ram Seshadri: thank you for being my extended academic family.

I would also like to thank my committee members, Professors Michael Doherty and Scott Shell, for their time and interest in my research. My gratitude also goes to all of the other professors and staff in chemical engineering, materials, MRL, and CNSI who have made this journey possible. To Nathan "Fuzzy" Rogers and Paul Weakliem, thank you for putting up with all the weird ways I've broken the compute clusters.

While my time at Sandia was short, I learned a phenominal amount, and got to work with some phenominal scientists, especially Ann E. Mattsson who has continued to support and mentor me to this day. My summer in Albuquerque marked the point where I began to feel like a real scientist, rather than just a student. The experience has been invaluable.

To my friends beyond the laboratory, thank you for sticking with me. Sean Cray, Corinne Carpenter, and Abe Pressman, thank you for helping me survive. Will Sing for Food/San Clemente voices, especially Erik Bell, thank you for helping me find my (singing) voice. Niels Zussblatt, thank you for being a wonderful friend, a fantastic flatmate, and an impossibly reliable, generous, amazing human. Valentina, thank you for always being a spider. To everyone in #caltech: especially Alex Roper, thanks for always being around. Team Hat, especially Isaac Sheff and Jennifer Greco, and Samson Chen, thanks for sticking with me for all these years, and for understanding me.

Christopher Kennelly: I am thankful every day for having you as my friend and as my partner. My life is so much more spectacular for having you in it. You've been the person I've needed no matter how bad things have gotten, and I look forward to finally closing our "long-distance" gap (even if we see each other every weekend).

Finally, to my parents Demetra and Frank Decolvenaere: thank you for your perpetual encouragement and belief in my dreams and abilities. I didn't make things easy — disassembling household objects, challenging teachers, staying too late at robotics club, leaving for college on the other side of the country. . . but you supported me at every step. You raised me well, and I hope I can continue to make you proud.

Curriculum Vitæ

Elizabeth Decolvenaere

Education

2012–2017 Ph.D. in Chemical Engineering, University of California, Santa Barbara, Santa Barbara, CA, USA.

2008–2012 B.S. in Chemical Engineering, California Institute of Technology, Pasadena, CA, USA.

Publications from Work at UCSB

2017 **Elizabeth Decolvenaere**, Emily Levin, Michael J. Gordon, and Anton Van der Ven, "A Cluster Expansion Approach to Magnetic Hardening in (Mn,Fe)Ru_2Sn Solid Solutions", *Submitted to Phys. Rev. Lett.*

2017 **Elizabeth Decolvenaere**, Michael J. Gordon, Ram Seshadri, and Anton Van der Ven, "First-principles Investigation of Competing Magnetic Interactions in Heusler (Mn,Fe)Ru_2Sn Solid Solutions", *Accepted in Phys. Rev. B*

2017 Andrew Pebley, **Elizabeth Decolvenaere**, Tresa Pollock, and Michael J. Gordon, "Oxygen evolution on Fe-doped NiO electrocatalysts deposited via microplasma", *Submitted to Nanoscale*

2016 **Elizabeth Decolvenaere**, Michael J. Gordon, and Anton Van der Ven, "Recovering 0 Kelvin Effective Hamiltonian Parameters from High-Temperature Disordered Phases", *Prepared*

2015 **Elizabeth Decolvenaere**, Michael J. Gordon, and Anton Van der Ven, "Testing Predictions from Density Functional Theory at Finite Temperatures: β_2-Like Ground States in Co-Pt", *Phys. Rev. B*, **92** 8, 085119 (2015)

Selected Presentations from Work at UCSB

2017 **Elizabeth Decolvenaere**, Michael J. Gordon, Ram Seshadri, and Anton Van der Ven, "Ab Initio Insights into Novel Magnetic Behavior in the Mn1-xFexRu2Sn Pseudo-Binary Heusler", *2017 MRS Spring Meeting*, ED13.12.03

2017 **Elizabeth Decolvenaere**, Michael J. Gordon, Ram Seshadri, and Anton Van der Ven, "Ab Initio Insights into Novel Magnetic Behavior in the Mn1-xFexRu2Sn Pseudo-Binary Heusler", *APS March Meeting 2017*, S32.00002

2016 **Elizabeth Decolvenaere**, Michael J. Gordon, Ram Seshadri, and Anton Van der Ven, "A Novel Route to Phase Diagrams: Recovering 0 Kelvin Hamiltonian Parameters from High-Temperature Disordered Phases", *2016 AIChE Annual Meeting*, Accelerated Discovery and Development of Inorganic Materials

2016 **Elizabeth Decolvenaere**, Michael J. Gordon, Ram Seshadri, and Anton Van der Ven, "Testing DFT Predictions at Finite Temperatures: Anomalous Phase Behavior and Long-Range Superstructures of CoPt", *2015 AIChE Annual Meeting*, Thermophysical Properties and Phase Behavior III

2016 **Elizabeth Decolvenaere**, Michael J. Gordon, Ram Seshadri, and Anton Van der Ven, "Running Statistical Mechanics "In Reverse": Converting High-Temperature Measurements into 0 Kelvin Predictions", *Materials Science and Engineering Congress 2016*, E02.4: First Principles

2016 **Elizabeth Decolvenaere**, Michael J. Gordon, Ram Seshadri, and Anton Van der Ven, "Verifying Ab Initio Predictions in Co-Pt Alloys Using Multiscale Modeling", *2016 MRS Spring Meeting*, CM4.1.07

List of Abbreviations

1BZ	First Brillouin Zone (the Voronoi cell around the origin in reciprocal space)
(A)FM	(Anti)Ferromagnetic
CASM	a Clusters Approach to Statistical Mechanics (CLEX fitting and GCMC simulation package)
CE	Cluster Expansion
COHP	Crystal Orbital Hamilton Populations
DFT	Density Functional Theory
DOF	Degree-of-Freedom
DOS	Density of States (either electronic or vibrational)
ECI	Effective Cluster Interaction (an expansion coefficient)
FCC	Face-Centered Cubic (a crystal structure)
FrM	FerriMagnetic
GGA	Generalized Gradient Approximation (functionals utilizing $\nabla\rho(\overline{r})$)
HGGA	Hyper Generalized Gradient Approximation (functionals utilizing exact exchange)
HK	Hohenberg-Kohn (usually referring to the theorems)
HSE	Heyd, Scuseria, and Ernzerhof functional (a hybrid functional using screened Hartree-Fock exchange)
IBZ	Irreducible Brillouin Zone (a wedge within the 1BZ containing unique points under the symmetry operations of the lattice)
KS	Kohn-Sham
LDA	Local Density Approximation (functionals utilizing only $\rho(\overline{r})$)
(MC)MC	(Markov Chain) Monte Carlo
MGGA	Meta Generalized Gradient Approximation (functionals utilizing the kinetic energy)
((N)N)N	((Next-)Next-)Nearest Neighbor
PAW	Projector-Augmented Waves (a smoothed basis set utilizing a frozen-core approach)
PBE	Perdew, Burke, and Ernzerhof functional (a popular GGA-type functional)
RKKY	Ruderman-Kittel-Kasuya-Yosida (a type of magnetic interaction)
RPA	Random Phase Approximation (functionals utilizing a portion of exact correlation)
SIE	Self-Interaction Error (errors in DFT induced by an electron "seeing itself")

SOC	Spin-Orbit Coupling (coupling between an electron's spin-moment and orbital-induced moment)
TM	Transition Metal
VASP	Vienna *Ab-initio* Simulation Package (a DFT software package using plane-waves popular in solid-state calculations)
XC	Exchange and Correlation (the non-classical parts of an electron's energy)

Symbols

Electronic Structure

ϵ	One-electron eigenstate energy
ρ	Electron density
$\overline{\tau}$	An integer multiple of a lattice vector
$\mathbf{\Psi}$	Many-body electronic and nuclear wave function
ψ	One-electron wave function
$\mathbf{\Omega}$	A reciprocal or real space volume
$\mathbf{c}$	Expansion coefficient
$\mathbf{f}$	Band filling factor
$\overline{\mathbf{g}}$	A point in reciprocal 3-space (usually a displacement from a k-point)
$\mathbf{H}$	Hamiltonian
$\overline{\mathbf{k}}$	A point in reciprocal 3-space (usually a k-point)
$\mathbf{m}_\alpha$	The mass of species α
$\mathbf{N}$	Number of nuclei
$\mathbf{n}$	Number of electrons
$\overline{\mathbf{q}}$	Mode of a plane wave in 3-space
$\overline{\mathbf{R}}$	A point in real 3-space (usually a nuclei's coordinate)
$\overline{\mathbf{r}}$	A point in real 3-space (usually an electron's coordinate)
$\mathcal{T}$	Operator transforming true wave functions to smoothed wavefunctions
$\mathbf{T}$	Kinetic energy
$\mathbf{V}$	Potential energy
$\mathbf{v}$	Effective potential (usually $\frac{\delta V[\rho]}{\delta \rho}$)
$\mathbf{w}$	Weight of a k-point
$\mathbf{Z}_\alpha$	The charge of species α

Cluster Expansion

α	A prototype geometic cluster, i.e., a unique δ under the symmetry operations of the lattice
δ	A geometic cluster, i.e., a non-repeating set of lattice indices
η	An order parameter
$\sigma_\mathbf{i}$ or $\overline{\sigma}_\mathbf{i}$	A scalar or vector describing the degree(s)-of-freedom at site i
$\overline{\sigma}$	A microstate, usually a collection of lattice site degrees of freedom $\{\sigma_1, \sigma_2, \ldots, \sigma_n\}$

ϕ or $\mathbf{\Phi}$	An intensive or extensive cluster function, usually a product of the spin variables of the included sites
$\mathbf{\Omega}$	An orbit
$\mathcal{T}$	Symmetry operation of a lattice
$\mathbf{V}$	Effective cluster interaction

General Thermodynamics

μ	Chemical potential
$\mathcal{P}(\overline{\sigma})$	Probability of microstate σ
$\mathbf{\Upsilon}$	Free energy at constant cluster function values (T, N, N_A, $\overline{\Phi}$)
$\mathbf{A}$	Helmholtz free energy (N, V, T)
$\mathbf{C_V}$	Constant volume heat capacity
$\mathbf{E}$	Energy
$\mathbf{G}$	Gibbs Free energy (N, P, T)
$\mathbf{k_b}$	Boltzmann constant
$\mathbf{N}$	Number of particles
$\mathbf{P}$	Pressure
$\mathbf{S}$	Entropy
$\mathbf{T}$	Temperature
$\mathbf{V}$	Volume
$\mathbf{Z}$	Partition function

Abstract

Improving *Ab-Initio* Simulations of Ordering Phenomena in Transition Metal Alloys

by

Elizabeth Decolvenaere

Density functional theory (DFT) is undergoing a shift from a descriptive to a predictive tool in the field of solid state physics, with undertakings like the Materials Project, OQMD, and AFLOW leading the way in utilizing high-throughput data to predict and seek novel materials properties. However, methods to rigorously evaluate the *validity* and *accuracy* of these studies is lacking in both the availability and utilization of techniques. The natural disconnect between simulated and experimental length-scales and temperatures, combined with this lack of validation, raises serious questions when simulation and experiment disagree. In this thesis, we analyze several transition metal systems where simulations and experiments present unusual disagreements, and develop a new formalism for comparing high-temperature measurements to *ab-initio* calculations. Our work aims to broaden the understanding not only of the specific systems discussed, but of how presently available *ab-initio* methods perform for transition metal alloys across *all* systems.

Recent high-throughput ab-initio studies of transition metal binaries have suggested a great number of undiscovered stable phases present in well-studied systems. Co-Pt alloys, especially, have a long experimental history demonstrating three stable mixed phases: $L1_0$ CoPt and $L1_2$ Co_3Pt and $CoPt_3$, but density functional theory suggests a set of yet-unobserved long-period β_2-like superstructures at Pt-rich compositions. We analyze the Co-Pt system in-depth, calculating the energy of over 1,400 structures to thoroughly explore the series of unusual superstructures suggested by DFT. Simulated diffraction

patterns, analysis of magnetic behavior, and investigation of the density-of-states emphasize the stark differences between measured behaviors and *ab-initio* predictions. By moving up the Jacob's Ladder of functionals, we show that we only replace one set of discrepancies for another, and even the introduction of vibrational degrees of freedom fails to solve the massive differences in predicted phase stability. By fitting the *ab-initio* results to a cluster expansion Hamiltonian and performing Monte Carlo calculations, we show that the resulting high-temperature phase diagram is wholly incompatible with experimental results.

Like Co-Pt, Heusler compounds have unique magnetic properties, resulting in interest for their potential applications as spintronic materials. The pseudo-binary (Mn,Fe)Ru_2Sn, formed as a solid solution of the full Heuslers (Mn, Fe)Ru_2Sn, has been recently shown to exhibit exchange-hardening implicative of two *magnetic* phases, despite the presence of only one *chemical* phase. Using *ab-initio* calculations we show that the magnetic behavior of this alloy arises from a competition between AFM-favoring Sn-mediated superexchange and FM-favoring RKKY exchange mediated by spin-polarized conduction electrons. Changes in valency upon replacement of Mn with Fe shifts the balance from superexchange-dominated interactions to RKKY-dominated interactions. Using our electronic structure calculations, we parameterize a mixed-basis chemical-and-magnetic cluster expansion, and use Monte Carlo simulations to demonstrate a ferromagnetic (FM) to antiferromagnetic (AFM) behavior dependent on composition with the experimental study. By examining the low-temperature ensemble averages of magnetic and chemical correlations, we identify the mechanism behind magnetic hardening in the solid solution.

Our multiple successes in utilizing cluster expansions, both to deeply analyze failures and successfully describe complex chemical-magnetic interactions, motivates an experiments-driven approach to lattice Hamiltonians. For alloys, cluster expansion Hamiltonians reduce the complex, many-body electron problem of density functional theory to

a series of simple site-wise basis functions (e.g., products of site occupancy variables) on an atomic scale. The resulting energy polynomial is computationally inexpensive, and hence suitable for the (tens of) thousands of calculations of large systems required by stochastic methods. We present a new method to run the statistical mechanics problem "in reverse", using high-temperature observations and thermodynamic connections to construct an effective Hamiltonian and thereby predict the 0 Kelvin energy spectrum and associated ground states. By re-examining the cluster expansion coefficients as thermodynamic state variables and utilizing entropy-maximization approaches, we develop an algorithm to select clusters and determine cluster interactions using only a few, high-temperature experiments on disordered phases. We demonstrate that our approach can recover not only the stable ground states at 0 Kelvin, but also the full phase behavior for three realistic two-dimensional and three-dimensional alloy test-cases.

Contents

Chapter 1

Introduction

I HOPE YOU KNOW WHAT YOU ARE DOING

VASP, the last line of many warnings in "tutor.F"

There is little and less in materials science that digital computing has not revolutionized. Electronic structure calculations offer a particularly striking success story, beginning with the Schrödinger[1] and Dirac[2] equations derived in the late 1920's. These two related equations are, generally, lacking in closed-form solutions for systems containing more than one electron. Instead, they can only be solved *numerically*, making for an incredibly tedious, if not impossible, task to perform by hand. The first digital computers, invented in the 1940's[1], could calculate in seconds what previously took hours or days[3], and without making mistakes or growing fatigued. Finding high-precision, numerical solutions for the full wavefunction in an arbitrary system had become an achievable goal. While the first electronic structure calculations were carried out for atoms and small molecules[4] and pushed the limits of the primitive computers of the 1950's, modern calculations utilize supercomputing clusters capable of simulating hundreds of atoms and

[1] to replace their human counterparts, for example, many of the calculations required for the Manhattan Project were carried out not by computers, but by rooms full of women!

thousands of electrons.

1.1 A Too-Short History of Density Functional Theory

A large part of the success of *ab-initio* materials science can be traced to the development of Density Functional Theory (DFT) by Kohn, Sham, and Hohenberg in the mid 1960's[5, 6], building on the prior work of Hartree, Fock, and Slater[7–10]. When initially proposed, Kohn-Sham DFT[2] was largely ignored in favor of the Xα method[13]:

> "Well, we recognize it now as a big event, but it did not seem so at the time. That was the second big mistake of my life, not to see [DFT's] importance, but then neither I think did the authors judging from the talks they gave, nor anyone else."[14]

In the 1970's, solid-state physicists began to take an interest in DFT and its application to solids[15]. The Local Density Approximation (LDA) functional worked well for simple metals, even though it failed for simple molecules. In 1980, the quantum Monte Carlo calculations of Ceperley and Alder[16] allowed for an accurate calculation of the correlation energy of a uniform electron gas, and in 1986 the first successful gradient-corrected functional was developed by Perdew and Wang[17, 18], enabling significant improvements in the accuracy of predicted molecular properties. In the early 1990's the first general-purpose DFT codes became broadly available, such as the DFT option in Gaussian[19], and the immensely popular solid-state DFT code VASP[20–22]. At this point, popularity of DFT in both the computational chemistry and computational materials science fields skyrocketed[23], and has continued to increase almost exponentially

[2] As opposed to other "density functional" theories, such as the work of Thomas and Fermi[11, 12]

since then[24]. Walter Kohn (jointly with John Pople) was awarded the Nobel Prize in Chemistry in 1998 for his contributions to the field of computational chemistry, cementing once and for all the status of DFT as among the most valuable scientific advancements of the 20th century. This history is visited in-depth in References [15, 23–26], and an interested reader is also encouraged to read about Walter Kohn's life leading up to the pivotal year of 1964[27]. Walter Kohn passed away in 2016[3], but his contributions in tandem with Sham and Hohenberg have permanently altered the path of chemistry and materials science research.

1.2 Density Functional Theory and Cluster Expansion Hamiltonians

DFT as applied to solids offers an incredibly precise, broadly applicable materials science framework. However, significant fundamental limitations exist: the scaling goes as the number of electrons cubed and the properties described are accurate only at zero kelvin. For the calculation of thermodynamically-averaged properties representing real temperatures and length-scales, DFT itself becomes something to *approximate*. Cluster Expansion Hamiltonians[28–30] are one solution, trading flexibility for speed by projecting electronic ground-state properties onto an orthonormal basis set of cluster functions well-suited to Monte Carlo-type sampling techniques. Each Cluster Expansion must be built and trained for one specific chemical and crystallographic system, but once constructed, can be used to sample any property that is an entropy-maximized function of the ensemble. Via Monte Carlo simulations, Cluster Expansions offer a rigorous thermodynamic link between the microscale world of DFT and the mesoscale world of "real"

[3]It is among the author's greatest regrets that she never had an opportunity to meet him

systems[31–34].

1.3 Challenges in Transition Metals

Transition metals (TMs) pose unique challenges for *ab-initio* calculations[24, 35–38], possessing a large number of chemically-active valence electrons distributed between localized (d-electron) and delocalized (s-electron) states. The highly-localized d-electrons are also strongly correlated, making the accurate calculation of purely quantum effects such as exchange and correlation vital in predicting the properties of TMs. Despite the challenges, TMs and multi-TM alloys account for a significant fraction of current research effort in materials science. From superalloys[39–41] and high-entropy alloys[42, 43], to unique magnetic materials[44–47] and spintronics[48–51], to shape-memory materials[52, 53], to thermoelectrics[45, 48, 54, 55], to catalysts[56–59], and even into the exotic realm of topological phases[48, 60, 61], TMs offer an overwhelming amount of technological promise.

The temperatures, length- and time-scales relevant to the above litany of applications makes multi-scale modeling techniques vital to properly characterizing the novel properties of TM alloys. Even the simplest, most common TM alloy — steel — requires a full stack of multiscale modeling techniques[62–65]: (1) *ab-initio* calculations, (2) modeling dilute substitutions and interstitials, (3) dislocation dynamics and defect migration/diffusion, (4) modeling ripening and growth processes and phase-field simulations, (5) simulating the interaction of grains, and (6) finite-element models suitable for macroscale (e.g., architectural or civil engineering) design. The problem only grows more complex for materials intended to operate at extreme temperatures and stresses, such as turbine blades. When determining the properties of a multi-component TM alloy, especially at elevated temperatures, proper consideration of the configurational

degrees-of-freedom is vital.

1.4 Overview

In the following Chapters we will explore both DFT as applied to TMs, and how Cluster Expansions can be used to make equilibrium predictions from zero kelvin DFT calculations. Chapter 2.1 will cover the theoretical foundation of DFT, explore how DFT is applied to extended systems, discuss some of the approximations and simplifications used to make the theory tractable, and touch on problems encountered when DFT is applied to TMs. Following that, Chapter 2.2 will also give an overview of the Cluster Expansion formalism, with a few remarks on the problems one may encounter. A more in-depth discussion of specific failure modes of DFT is then found in Chapter 3, in addition to an example of a Cluster Expansion being used to construct a phase diagram. Chapter 4 offers a closer look at the thermodynamics of the Cluster Expansion formalism, and constructs an alternative model utilizing high-temperature experiments instead of *ab-initio* calculations for parametrizing the Hamiltonian. Chapters 5 and 6 form two halves of one story, demonstrating the predictive power of DFT calculations and the flexibility of Cluster Expansions through the process of developing an *ab-initio* model for novel magnetic behavior. Finally, we will conclude with a brief summary of Chapters 3 through 6, comparing and contrasting our results and drawing some general conclusions.

1.5 Permissions and Attributions

1. The content of Chapter 3 has previously appeared in Reference [32]:

   E. Decolvenaere, M. J. Gordon, A. Van der Ven, "Testing predictions from density functional theory at finite temperatures: β_2-like ground states in Co-Pt", *Phys.*

Rev. B **92** 085119 (2015) 2015 American Physical Society.

2. The content of Chapter 4 has previously appeared in Reference [66]:
   E. Decolvenaere, M. J. Gordon, A. Van der Ven, "Recovering 0 Kelvin Effective Hamiltonian Parameters from High-Temperature Disordered Phases", arXiv:1609.07175.

3. The contents of Chapters 5 and 6 appear substantially in manuscripts currently submitted to *Phys. Rev. B* and *Phys. Rev. Lett.*.

4. This work and Elizabeth Decolvenaere were supported by the MRSEC Program of the Natural Science Foundation under Award No. DMR-1121053.

5. Simulations were performed using resources from the Center for Scientific Computing in the CNSI and MRL, funded by NSF MRSEC (DMR-1121053), NSF CNS-0960316, and Hewlett Packard.

Chapter 2

Theoretical Background and Computational Methods

> We have not succeeded in answering all our problems. The answers we have found only serve to raise a whole set of new questions. In some ways we feel we are as confused as ever, but we believe we are confused on a higher level and about more important things.
>
> ---
>
> *Bernt Øksendal*, Stochastic Differential Equations

The universe that we live in is, generally, a *classical* universe. The length- and time-scales and temperatures we interact with yield macroscale, generally equilibrium dynamics obeying Newtonian physics. Any observation we make of a macroscale quantity, describing some equilibrium set of properties (referred to hereafter as a *macro*state), is nonetheless defined by a series of microscale phenomena. For any set of thermodynamic variables $\{X\}$, whether extensive (system-scaling) or intensive (scale-independent), and for any measured quantity y, the observed value of y can be expressed as:

$$\langle y \rangle (\{X\}) = \sum_{\overline{\sigma} \in \{X\}} \mathcal{P}(\overline{\sigma})\, y(\overline{\sigma}) = \langle y \rangle, \tag{2.1}$$

Where $\overline{\sigma}$ is a microstate (one system snapshot satisfying the conditions given by $\{X\}$) and $\mathcal{P}(\overline{\sigma})$ is a probability of that microstate. Depending on which set of thermodynamic variables one wants to control, $\mathcal{P}$ can take on different forms. All forms follow the general form given below for the case of a set of microstates with a constant number of particles N, a constant volume V, and constant temperature T:

$$\mathcal{P}(\overline{\sigma}) = \frac{1}{Z(N,V,T)} \exp\left(-\frac{E(\overline{\sigma})}{k_b T}\right) \tag{2.2}$$

$$Z(N,V,T) = \sum_{\overline{\sigma} \in N,V} \exp\left(-\frac{E(\overline{\sigma})}{k_b T}\right), \tag{2.3}$$

such that $\sum_{\overline{\sigma}} \mathcal{P}(\overline{\sigma}) = 1$, where Z, the partition function, is a normalizing factor, and k_b is the Boltzmann constant. The probability function $\mathcal{P}$, called a Boltzmann or Gibbs distribution, takes its exponential form from solving for the distribution that maximizes the entropy S, which contains a logarithmic component:

$$S(\{X\}) = -K \sum_{\overline{\sigma} \in \{X\}} \mathcal{P}(\overline{\sigma}) \log\left(\mathcal{P}(\overline{\sigma})\right). \tag{2.4}$$

This function defines a measure of information S that satisfies Shannon's required properties[67]:

1. continuous in the space of $\overline{\sigma}$,

2. monotonically increases with increasing numbers of unique microstates,

3. additive for sub-divisions of the space of $\overline{\sigma}$ (such that the entropy of one ensemble

of $\overline{\sigma}$ is a weighted sum of the constituent sub-ensembles, $\overline{\sigma}_A$ and $\overline{\sigma}_B$).

While K can be any positive scalar in Shannon's definition (used in computer science contexts), for our purposes $K = k_b$, i.e., Boltzmann's constant. A rigorous proof of this equality, as well as a more in-depth discussion of the connections between information theory and statistical mechanics/thermodynamics, is given by Jaynes in the course of several publications[68–72].

Thus far, we have placed no restriction on what $\{X\}$ or y can be, nor given any advice on the form of $E(\overline{\sigma})$. Generally, $\{X\}$ is a set of thermodynamic variables constraining the system to some space of microstates. In our above example we chose N, V, T to constrain the number of particles, the volume those particles reside in, and a temperature the system is at. Each thermodynamic variable has a conjugate variable; the conjugate set of variables for our system are μ, P, S which stand for chemical potential, pressure, and entropy, respectively. At temperatures greater than zero kelvin, both a variable and its conjugate cannot be controlled/specified simultaneously. The identity of y can be any observable microstate property, e.g., composition, volume, or total magnetic moment. The ensemble value of y is then given by a weighted average of microstate values, as described in Equation 2.1.

Intensive variables, such as chemical potential, pressure, or magnetic field, are *not* defined in individual microstates. Instead, these intensive variables measure the relationship between their extensive conjugate and the ensemble free energy. In the case of the canonical ensemble (N, V, T), the Helmholtz free energy:

$$A(N, V, T) = -k_b T \log\left(Z(N, V, T)\right)$$

is connected to the pressure via the following thermodynamic relationship:

$$P(N,V,T) = -\frac{\partial A}{\partial V}\bigg|_{T,N} = -\sum_{\sigma \in N,V} \mathcal{P}(\overline{\sigma}) \frac{\partial E}{\partial V}(\overline{\sigma}).$$

Free energies, such as the Helmholtz free energy A or the Gibbs free energy G (T, P, N), are also ensemble properties of a specified set of thermodynamic variables. Using free energies, we can determine the relative stability of various groupings of microstates, and begin to define phases. Where free energies intersect, phase transitions occur.

Any measurable thermodynamic variable or energy, whether extensive or intensive, can then be calculated for a given $\{X\}$, given we know the form of $E(\overline{\sigma})$. However, we often do not have a "nice" closed-form expression for $E(\overline{\sigma})$, and even when we do, it is impractical to calculate the properties of *every* possible microstate. For even a simple 2D spin system with a scant 1,000 particles, the number of unique microstates (assuming no symmetry) is $2^{1000} \sim 10^{301}$.

Instead, given a form for $E(\overline{\sigma})$, we utilize Markov-Chain[73] Monte Carlo (MCMC, or just MC) using the Metropolis-Hastings algorithm[74, 75] to obtain a Boltzmann-weighted sample of microstates with thermodynamic properties equal to those of the full ensemble. For our system of 1,000 particles, reasonable estimates for thermodynamic averages can be achieved with only 1,000,000 or so evaluations [1]. Though significantly smaller than 10^{301}, 10^6 is still far too large for any *ab-initio* method to calculate in a reasonable period of time. Instead, our approach is to sample an even smaller set of microstates (usually 100 to 1,000) using first-principles methods, and then to train a simplified Hamiltonian utilizing a reduced set of degrees-of-freedom (DOFs) for use in MC sampling.

In the following sections we will explain how one goes from first principles to phase diagrams. The first section covers Density Functional Theory[5, 6] (DFT), a workhorse

[1] Convergence is usually achieved in a few thousand passes, one pass being a number of attempted moves equal to the numbers of sites in the system

electronic structure calculation technique used extensively in materials science. We will explain both how DFT operates, the assumptions being made, and where the assumptions can lead to trouble. The second section explains the Cluster Expansion (CE) formalism[28], an elegant yet powerful approach to constructing computationally inexpensive, *ab-initio*-accurate Hamiltonians. We will explain how the cluster functions form a complete, orthonormal basis set, and how by utilizing a reduced (compared to DFT) set of DOFs, all of the equilibrium properties of a system can be reproduced. Our review will also briefly touch on the methods used to construct CEs, including a discussion of regression techniques and sparsity.

2.1 Electronic Structure Calculations

When performing *ab-initio* calculations, our goal is to make a meaningful prediction using *no* empirical parameters. Starting with a set nuclei and their associated coordinates, all of the ground-state properties of the system can be calculated from Schrödinger's equation[1]. A general (if deceptively simple) representation of the problem is given by the time-independent Schrödinger equation:

$$\hat{H}|\mathbf{\Psi}\rangle = E|\mathbf{\Psi}\rangle, \tag{2.5}$$

where $\hat{H}$ is the Hamiltonian operator, $\mathbf{\Psi}$ is a wave function containing the electronic and nuclear DOFs, and E is the energy. This is an eigenvalue problem, with $|\mathbf{\Psi}\rangle$ being an eigenvector of the matrix operator $\hat{H}$, and E is an eigenvalue.

The trouble lies in the forms of $\hat{H}$ and $|\mathbf{\Psi}\rangle$. $|\mathbf{\Psi}\rangle$ is a many-body wave function, which has $3(n+N)$ DOFs describing the location of each of the n electrons and each of the N nuclei[2]: $\hat{r}|\mathbf{\Psi}\rangle = \mathbf{\Psi}(\overline{r}_1, \overline{r}_2, \ldots, \overline{r}_n, \overline{R}_1, \overline{R}_2, \ldots, \overline{R}_N)$. For a non-relativistic treatment,

[2]If we considered time-dependent properties we would also need the momentum DOFs, giving us

Equation 2.5 becomes: [3]

$$\left[-\sum_{\alpha}^{n}\frac{1}{2}\nabla_i^2-\sum_{\alpha}^{N}\frac{1}{2m_\alpha}\nabla_\alpha^2+\sum_{i}^{n}\frac{1}{2}\sum_{j\neq i}^{n}\frac{1}{|\overline{r}_i-\overline{r}_j|}+\sum_{\alpha}^{N}\frac{1}{2}\sum_{\beta\neq\alpha}^{N}\frac{Z_\alpha Z_\beta}{|\overline{R}_\alpha-\overline{R}_\beta|}-\sum_{\alpha}^{N}\sum_{i}^{n}\frac{Z_\alpha}{|\overline{R}_\alpha-\overline{r}_j|}\right]\mathbf{\Psi}(\{\overline{r}_n\},\{\overline{R}_N\})=E\mathbf{\Psi}(\{\overline{r}_n\},\{\overline{R}_N\}).$$

The four summations inside the Hamiltonian are, in order, the electronic kinetic energy $\hat{T}_n$, the nuclear kinetic energy $\hat{T}_N$, the electron-electron interaction $\hat{V}_{nn}$, the nuclear-nuclear interaction $\hat{V}_{NN}$, and the electronic-nuclear interaction $\hat{V}_{Nn}$. As the nuclei are many orders of magnitude heavier than the electrons, we can take the electronic and nuclear parts of the wave function $\mathbf{\Psi}$ as separable: $\mathbf{\Psi}(\{\overline{r}_n\},\{\overline{r}_N\}) = \mathbf{\Psi}_{elec.}(\{\overline{r}_n\}) \times \mathbf{\Psi}_{nucl.}(\{\overline{r}_N\})$. The coupling term $\hat{V}_{Nn}$ containing $\frac{1}{|\overline{r}_\alpha - r_i|}$ ensures that the electrons still feel the background potential of the nuclei, and vise-versa. We can further assume that the separations of mass scales results in a separation of time scales: for equal distributions of *momentum*, the electron velocities are orders of magnitude greater than the nuclear velocities. The result is that for any nuclear configuration the electrons can always instantaneously equilibrate (with respect to the time scale of the nuclei). These assumptions comprise the Born-Oppenheimer approximation[76], which allows us to describe the nuclei as a collection of classical point-charges interacting with each other and with the electrons *only* as a background charge density. The remaining quantum part, the electronic wave function Ψ_{elec} (simply called Ψ) now solves:

$6(n+N)$

[3] We use Hartree atomic units ($\hbar = e^2 = m_e = 1$) to keep our equations free of extraneous symbols.

$$\left[-\frac{1}{2}\sum_{\alpha}^{n}\nabla_i^2+\frac{1}{2}\sum_{i}^{n}\sum_{j\neq i}^{n}\frac{1}{|\overline{r}_i-\overline{r}_j|}-\sum_{\alpha}^{N}\sum_{i}^{n}\frac{Z_\alpha}{|\overline{r}_\alpha-\overline{r}_j|}\right]\Psi(\{\overline{r}_n\})=E_n\Psi(\{\overline{r}_n\}). \quad (2.6)$$

Here, the $\{\overline{r}_N\}$ are taken as fixed parameters, such that the coupling term $\hat{V}_{Nn} = \hat{V}(\{\overline{r}_N\})$. The expectation value of the second sum, $\langle\Psi|\sum_i^n\sum_{j\neq i}^n\frac{1}{|\overline{r}_i-\overline{r}_j|}|\Psi\rangle$, contains both a classical electron-electron interaction, as well as all of the quantum complexity associated with the fermionic nature of the electrons.

No exact solutions exist for $\Psi(\{\overline{r}_n\})$ for $n > 1$. However, even if we could solve for the exact form of $\Psi(\{\overline{r}_n\})$, we would not be able to use it. Consider an observable O, which we wish to calculate. The expectation value of O relies on the operator $\hat{O}$, such that:

$$\langle O\rangle=\langle\Psi|\hat{O}|\Psi\rangle=\int \mathrm{d}\overline{r}_1\int \mathrm{d}\overline{r}_2\cdots\int \mathrm{d}\overline{r}_n\Psi^*(\{\overline{r}_n\})\hat{O}\Psi(\{\overline{r}_n\}). \quad (2.7)$$

Unless we can determine some simplification that allows us to separate $\Psi(\{\overline{r}_n\})$, this (numerical) integration will scale as $\mathcal{O}(k^{3n})$, where k is the number of divisions along each direction in space. For an extremely rough integration using a $10\times10\times10$ grid, in an extremely modest 10-electron system, this is 10^{30} evaluations. If we could use the entire computational might of the Cori[4] supercomputer at NERSC, this calculation would take a not-so-modest 1,000,000 *years*!

For this reason, nearly all approaches to solving Equation 2.6 involve decomposing $\Psi(\{\overline{r}_n\})$ into a series of one-particle wave functions $\psi(\overline{r}_i)$, such that evaluations of Equation 2.7 can be performed on 3-dimensional grids, and the number of evaluations will scale more reasonably as (something like) $\mathcal{O}(nk^3)$[5]. While many methods exist, perhaps

[4]Rated at a theoretical peak performance of 31.4 PFlops as of 2017

[5]Note that this is the time complexity of evaluating $\langle O\rangle$, *not* of determining $\Psi(\{\overline{r}_n\})$!

the most popular (owing to a confluence of [relative] computational ease and reasonably high accuracy) technique is DFT, or Density Functional Theory. In this approach, an auxiliary non-interacting system described using single-particle wave functions $\psi_i^{KS}(\overline{r}_i)$ is solved for, such that the electron energy E_n and the electron density $\rho(\overline{r})$ of the auxiliary system correspond to the energy and density of the *real* system. This approach, as well as the assumptions and approximations made and the problems they can cause, will be discussed in-depth in the subsequent subsections. Case studies of DFT applied to real systems are described in Chapters 3 and 5.

2.1.1 Density Functional Theory

The foundation for DFT builds upon two fundamental theorems, known as the Hohenberg-Kohn (HK) theorems:

1. The full many-particle ground state relies solely upon, and is a unique functional of, the electron density $\rho(\overline{r}) : E = E[\rho(\overline{r})]$

2. The density $\rho(\overline{r})$ which minimizes $E[\rho(\overline{r})]$ is the unique ground-state density, such that $E[\rho(\overline{r})] > E[\rho_0(\overline{r})]$ for all $\rho(\overline{r}) \neq \rho_0(\overline{r})$, where $\rho_0(\overline{r})$ is the ground-state density

A pair of simple, beautiful proofs of the above two theorems can be found in Hohenberg and Kohn's 1964 paper[6]. Equation 2.6 can be reformulated in terms of energy functionals, instead of operators. The resulting Hamiltonian looks like:

$$E[\rho(\overline{r})] = T[\rho(\overline{r})] + V_{Nn}[\rho(\overline{r})](\{\overline{r}_N\}) + V_{nn}[\rho(\overline{r})], \tag{2.8}$$

where T is the kinetic energy functional, V_{Nn} is the potential energy functional of the electrons interacting with the nuclei, and V_{nn} is the potential energy functional of the electrons interacting with other electrons, both classically and quantum-mechanically.

Prior approximations to T and V_{nn}, such as the Thomas-Fermi model[11, 12], failed due to the presence of strong quantum-mechanical effects[77]. To route around this problem, Kohn and Sham divided the kinetic energy and the electron-electron potential energy into two parts: (1) an approximation using a non-interacting/classical system $T_S[\rho(\overline{r})]$ and $V_H[\rho(\overline{r})]$, and (2) a set of correction terms that represent the differences $T_C[\rho(\overline{r})] = T[\rho(\overline{r})] - T_S[\rho(\overline{r})]$ and $V_X[\rho(\overline{r})] = V_{nn}[\rho(\overline{r})] - V_H[\rho(\overline{r})]$[5]. These last two terms are usually combined into one exchange-and-correlation (XC) functional, $V_{XC}[\rho(\overline{r})] = V_X[\rho(\overline{r})] + T_C[\rho(\overline{r})]$. The energy expression is then:

$$E[\rho(\overline{r})] = T_S[\rho(\overline{r})] + V_{Nn}[\rho(\overline{r})](\{\overline{r}_N\}) + V_H[\rho(\overline{r})] + V_{XC}[\rho(\overline{r})]. \tag{2.9}$$

Utilizing HK theorem two, we can solve for the density $\rho(\overline{r})$ by finding the density which minimizes the energy, given the constraint that $\int \mathrm{d}\overline{r}\rho(\overline{r}) = n$ where n is the number of electrons. To do that, we take a functional derivative of $E[\rho(\overline{r})]$ with respect to the density, and use a Lagrange multiplier μ:

$$\frac{\delta}{\delta\rho(\overline{r})}\left(T_S[\rho(\overline{r})] + V_{Nn}[\rho(\overline{r})](\{\overline{r}_N\}) + V_H[\rho(\overline{r})] + V_{XC}[\rho(\overline{r})] - \mu\left(\int \mathrm{d}\overline{r}\rho(\overline{r}) - n\right)\right) = 0,$$

$$\begin{aligned}\mu &= \frac{\delta T_S[\rho(\overline{r})]}{\delta\rho(\overline{r})} + \frac{\delta V_{Nn}[\rho(\overline{r})](\{\overline{r}_N\})}{\delta\rho(\overline{r})} + \frac{\delta V_H[\rho(\overline{r})]}{\delta\rho(\overline{r})} + \frac{\delta V_{XC}[\rho(\overline{r})]}{\delta(\rho)}, \\ &= \frac{\delta T_S[\rho(\overline{r})]}{\delta\rho(\overline{r})} + v_{Nn}(\overline{r};\{\overline{r}_N\}) + v_H(\overline{r}) + v_{XC}(\overline{r}).\end{aligned}$$

This equation is, however, just the Hamiltonian for the non-interacting system in a background potential $v_{\text{eff}}(\overline{r}) = v_{Nn}(\overline{r};\{\overline{r}_N\}) + v_H(\overline{r}) + v_{XC}(\overline{r})$. In effect, this tells us that for a perfect $v_{XC}(\overline{r})$, we can solve the *separable* eigenvalue problem of a non-interacting

system, and the resulting density is the *real* density. The unknown function $v_{XC}(\overline{r})$ accounts for all the differences between the non-interacting system and the real system.

We solve the non-interacting, auxiliary Kohn-Sham (KS) system by starting with an auxiliary wave function $\Psi_{KS}(\{\overline{r}_n\})$. The simplest available wave function for a series of non interacting fermions is a Slater determinant[9, 78, 79], made up of orthonormal one-electron eigenstates $\psi_{i,KS}(\overline{r}_i)$:

$$\Psi_{KS}(\{\overline{r}\}) = \frac{1}{\sqrt{n}} \begin{vmatrix} \psi_1(\overline{r}_1) & \psi_2(\overline{r}_1) & \cdots & \psi_n(\overline{r}_1) \\ \psi_1(\overline{r}_2) & \psi_2(\overline{r}_2) & \cdots & \psi_n(\overline{r}_2) \\ \vdots & \vdots & \ddots & \vdots \\ \psi_1(\overline{r}_n) & \psi_2(\overline{r}_n) & \cdots & \psi_n(\overline{r}_n) \end{vmatrix}. \tag{2.10}$$

The non-interacting energy for a background potential of $v_{\text{eff}}(\overline{r}) = v_{Nn}(\overline{r}; \{\overline{r}_N\}) + v_H(\overline{r}) + v_{XC}(\overline{r})$ is:

$$\begin{aligned} \langle \Psi_{KS}| -\frac{1}{2}\sum_i^n \nabla_i^2 + v_{\text{eff}}(\overline{r})|\Psi_{KS}\rangle = \\ \sum_i^n \int \mathrm{d}\overline{r} \left(-\psi_i^*(\overline{r})\frac{1}{2}\nabla^2\psi_i(\overline{r}) - \sum_\alpha^N \left(\frac{Z_\alpha}{|\overline{r}_\alpha - \overline{r}|}\right)\psi_i^*(\overline{r})\psi_i(\overline{r}) \right. \\ \left. + \int \mathrm{d}\overline{r}' \left(\frac{\psi_i^*(\overline{r})\psi_i(\overline{r})\rho(\overline{r}')}{|\overline{r} - \overline{r}'|}\right) + \psi_i^*(\overline{r})\psi_i(\overline{r})v_{XC}(\overline{r}) \right). \end{aligned}$$

Because of the orthonormality of the one-electron eigenstates, most terms drop out under $\langle\psi_i|\psi_j\rangle = \delta_{i,j}$. What remains is a separable equation decomposable into an eigenvalue problem solving for single-electron eigenstates. By variationally minimize the expectation value of the energy with respect to the one-electron eigenstates and using another Lagrange multiplier to ensure that orthonormality is preserved:

$$\frac{\delta}{\delta\langle\psi_i|}\left(\langle\Psi_{KS}| - \frac{1}{2}\sum_i^n \nabla_i^2 + v_{\text{eff}}(\overline{r})|\Psi_{KS}\rangle - \sum_i\sum_j \epsilon_{ij}\left(\langle\psi_i|\psi_j\rangle - \delta_{ij}\right)\right) = 0$$

$$\left(-\frac{1}{2}\nabla^2 - \sum_\alpha^N\left(\frac{Z_\alpha}{|\overline{r}_\alpha - \overline{r}|}\right) + \int \mathrm{d}\overline{r}'\frac{\rho(\overline{r}')}{|\overline{r} - \overline{r}'|} + v_{XC}(\overline{r})\right)\psi_i(\overline{r}) = \epsilon_i\psi_i(\overline{r}) = \hat{h}_{KS}\psi_i(\overline{r}). \tag{2.11}$$

Equation 2.11 is a one-particle Schrödinger equation that can be solved to produce the KS eigenfunctions. The KS eigenfunctions are used to define the density $\rho(\overline{r})$, which is used to update $\hat{h}_{KS}$ in Equation 2.11. At each step, Equation 2.9 is used to calculate the total energy; when the energy differences become sufficiently small the algorithm is terminated. Computationally, the most expensive step is integrating functionals of the density, which is $\mathcal{O}(k^3)$ where k is, as before, the number of divisions along each dimension in space. Compared to $\mathcal{O}(k^{3n})$ for evaluations of properties of the full n-electron wave function, this is an incredible improvement!

The one remaining unknown is the form of $V_{XC}[\rho(\overline{r})]$. DFT is exact for a perfect $V_{XC}[\rho(\overline{r})]$, but unfortunately, the perfect functional is not known[80]. Instead, we have the "alphabet soup" of V_{XC} approximations, each coming with their own built-in assumptions and failure modes[26, 35, 36]. These functionals occupy a rough hierarchy, referred to as the "Jacob's Ladder of Functionals" by J. Perdew and K. Schmidt[81]. Each rung of the ladder adds more complexity to V_{XC}, but also (theoretically) gets closer to the perfect functional. General forms of each rung of functionals, and a short explanation of what each one means, are given in Table 2.1.

Other popular approximations/approaches exist which do not neatly fit into the Jacob's ladder. LDA+U[82–85], which adds an empirical on-site Coulomb repulsion term U intended to encourage electrons to localize onto (atomic) orbitals with integer oc-

Table 2.1: Various forms of $E_{XC}[\rho]$ for different approximations used in solid-state DFT.

Approximation	Form	Represents
Local Density (LDA)	$\int \mathrm{d}\overline{r}\rho(\overline{r})f(\rho(\overline{r}))$	Uniform electron gas
Generalized Gradient (GGA)	$\int \mathrm{d}\overline{r}\rho(\overline{r})f(\rho(\overline{r}), \nabla\rho(\overline{r}))$	Slowly-varying (small) gradients
meta-Generalized Gradient (MGGA)	$\int \mathrm{d}\overline{r}\rho(\overline{r})f(\rho(\overline{r}), \nabla\rho(\overline{r}), \tau(\overline{r}))$	GGA + self-correlation corrections
hyper-Generalized Gradient (HGGA)	$\int \mathrm{d}\overline{r}\rho(\overline{r})f(\rho(\overline{r}), \nabla\rho(\overline{r}), \tau(\overline{r}), \epsilon_x(\overline{r}))$	(M)GGA + exact exchange, uses $\langle\phi_i\|v(\overline{r})\phi_j\rangle$
Random Phase (RPA)	$\int \mathrm{d}\overline{r}\rho(\overline{r})f(\rho(\overline{r}), \nabla\rho(\overline{r}), \tau(\overline{r}), \epsilon_x(\overline{r}), \{\psi_k\}_{empty})$	HGGA + long-range correlation, uses unoccupied orbitals $\|\phi_k\rangle_{empty}$

cupations, utilizes projections onto localized orbitals of a subset of the KS eigenstates but can otherwise be tacked-on to other methods. Determination of the parameter U is an open problem whose solution is hotly debated[86]. Sub-system functions, such as AM05[87, 88], divide up the problem into different regions (e.g., "edge" vs "interior") and apply a different $V_{XC}[\rho(\overline{r})]$ to each. Such sub-system functionals can utilize (in theory) any of the functional forms found in Table 2.1 to each of the subsystems, or entirely new forms suited only to specific geometries.

Of the alphabet soup of functionals used in solid-state physics [6], the vast majority of calculations are performed using a surprisingly small number of techniques[24]. In materials science, especially for metals, the most popular functional is the PBE[89] (Perdew, Burke, and Ernzerhof) implementation of the GGA. Materials Project[90], AFLOWLIB[91], and OQMD[92], three popular high-throughput DFT databases of alloys and oxides, utilize PBE and PBE+U (utilizing an empirically-determined on-site Hubbard correction) for their millions of calculated structures. PBE is a "parameter

[6] if one includes functionals developed for molecular systems, the space goes from "soup" to "ocean"

free" functional, meaning free of *empirical* parameters: every parameter involved is instead derived in some fashion from exact theoretical conditions or constraints.

2.1.2 Density Functional Theory for Extended Systems

DFT applied to bulk, periodic, solid systems provides an additional set of challenges far beyond "merely" finding $V_{XC}[\rho(\overline{r})]$. First is the choice of an appropriate basis set. Periodicity provides a periodic external potential from the nuclei and enforces a corresponding periodicity in the probability density of the one-electron eigenstates:

$$v_{Nn}(\overline{r};\{\overline{R}\}) = v_{Nn}(\overline{r}+\overline{\tau};\{\overline{R}\}),$$
$$|\psi_i(\overline{r})|^2 = |\psi_i(\overline{r}+\overline{\tau})|^2,$$

where $\overline{\tau}$ is some integer multiple of a lattice vector of the primitive cell, i.e., equivalent locations in different copies of the primitive cell must "look" the same. Bloch's theorem[93] tells us that rather than assigning electrons atomic orbitals of specific nuclei, points in reciprocal space, $\overline{k}$, provide us with good quantum numbers. Our electrons live in Bloch States, indexed by reciprocal vector $\overline{k}$:

$$\psi_{\overline{k}}(\overline{r}) = e^{\mathrm{i}\overline{k}\cdot\overline{r}} u_{\overline{k}}(\overline{r}), \tag{2.12}$$

where $u_{\overline{k}}(\overline{r})$ is periodic function (like $v_{Nn}(\overline{r};\{\overline{R}\})$). Then, for offsets of the form $\overline{r}+\overline{\tau}$, $\psi_{\overline{k}}(\overline{r}+\overline{\tau})$ only differs by a phase factor, $e^{\mathrm{i}\overline{k}\cdot\overline{\tau}} = (-1)^t$ where t is an integer. If $\overline{k}$ falls outside of the first Brillouin zone (1BZ), we can define a new $\overline{k}' = \overline{k} + \overline{g}$, where $\overline{g}$ is an integer multiple of a reciprocal lattice vector of the primitive cell. The exponential part of Equation 2.12 again differs only by a phase factor for $\overline{k}+\overline{g}$, while for $u_{\overline{k}'}(\overline{r}) = u_{\overline{k},n}(\overline{r})$.

The meaning of the second subscript on u indicates which eigenstate solution to u we will use; the periodic nature of $v_{Nn}(\overline{r};\{\overline{R}\})$ results in a *spectrum* of solutions for $u_{\overline{k}}(\overline{r})$, indexed by n. Each n makes up one band, which provides (over the whole 1BZ) one one-electron state.

The density expression, utilizing the Bloch states, is:

$$\rho(\overline{r}) = \frac{1}{\Omega_{1BZ}} \sum_n \int \mathrm{d}\overline{k} \psi^*_{\overline{k},n}(\overline{r}) \psi_{\overline{k},n}(\overline{r}) f_{\overline{k},n}, \tag{2.13}$$

where Ω_{1BZ} is the volume of the 1BZ, and $f_{\overline{k},n}$ is a band filling factor dependent on the electron temperature and the band energy relative to the Fermi energy. We can expand $u_{\overline{k},n}(\overline{r})$, and hence $\psi_{\overline{k},n}(\overline{r})$ and $\rho(\overline{r})$ in a basis of plane waves, such that:

$$u_{\overline{k},n}(\overline{r}) = \sum_{\overline{q}} c_{\overline{q},\overline{k},n} e^{\mathrm{i}\overline{q}\cdot\overline{r}} \qquad \psi_{\overline{k},n}(\overline{r}) = \sum_{\overline{q}} c_{\overline{q},\overline{k},n} e^{\mathrm{i}(\overline{q}+\overline{k})\cdot\overline{r}}$$

$$\rho(\overline{r}) = \frac{1}{\Omega_{1BZ}} \sum_n \int \mathrm{d}\overline{k} f_{\overline{k},n} \sum_{\overline{q}'} \sum_{\overline{q}} c^*_{\overline{q}',\overline{k},n} c_{\overline{q},\overline{k},n} e^{\mathrm{i}(\overline{q}-\overline{q}')\cdot\overline{r}} = \sum_{-2\overline{q}_{max}}^{2\overline{q}_{max}} \rho(\overline{r})_{\overline{q}} e^{\mathrm{i}\overline{q}\cdot\overline{r}}.$$

A cutoff energy is specified to limit the size of the basis set, such that q_{max} solves $E_{cut} = \frac{1}{2}\left|\overline{q}+\overline{k}\right|^2$. A finite grid of k-points is also specified, transforming $\int \mathrm{d}\overline{k} \to \sum_{\overline{k}} \tilde{w}_{\overline{k}}$, where $\tilde{w}_{\overline{k}}$ are the weights of the k-points such that $\sum_{\overline{k}}^{1BZ} \tilde{w}_{\overline{k}} = \Omega_{1BZ}$. Symmetries of the crystal lattice can also be applied to the k-point mesh, making the calculation of $c_{\overline{q},\overline{k},n}$ at many points redundant and reducing the sum over all $\overline{k}$ in the 1BZ to a sum over the irreducible Brillouin zone (IBZ) with $\tilde{w}_{\overline{k}} \forall \overline{k} \in \text{1BZ} \to s_{\overline{k}} \tilde{w}_{\overline{k}} = w_{\overline{k}} \forall \in IBZ$, where $s_{\overline{k}}$ is a symmetry-dependent factor and $\sum_{\overline{k}}^{IBZ} w_{\overline{k}} = \Omega_{1BZ}$.

Computationally, this allows for (relatively) inexpensive calculations of the coefficients $c_{\overline{q},\overline{k},n}$. The efficacy of fast Fourier transforms (FFTs) means that each part of the KS Hamiltonian can be evaluated in the best possible space, and the results then combined.

For example, the non-interacting kinetic energy operator $-\frac{1}{2}\nabla^2$ applied to the Bloch states simply yields an energy of:

$$\frac{1}{2\Omega_{1BZ}} \sum_n \sum_{\overline{k}}^{IBZ} w_{\overline{k}} f_{\overline{k},n} \sum_{\overline{q}}^{\overline{q}_{max}} \left|\overline{q}+\overline{k}\right|^2 \left|c_{\overline{q},\overline{k},n}\right|^2,$$

when evaluated in reciprocal space. The Hartree energy is also easily evaluated in reciprocal space, as

$$2\pi\Omega_{1BZ} \sum_{\overline{q}\neq 0}^{q_{max}} \frac{\left|\rho(\overline{q})\right|^2}{\overline{q}^2}.$$

However, other parts of the Hamiltonian (e.g., the XC energy) are not easily evaluated in reciprocal space. A mixed approach: evaluating some portions of the Hamiltonian in reciprocal space, and others in real space, can often speed up calculations so far as to make the FFTs the rate-limiting step.

2.1.3 Pseudopotentials

Unfortunately, for any element heavier than lithium, the basis set size required to accurately predict the ground-state energy becomes infeasibly large. This is because of the presence of nodes in the wavefunctions of the non-valence electrons, which require a large number of terms to converge. Adding more electrons also require adding more states, and hence also increases the max n which must be considered when developing the $\psi_{\overline{k},n}(\overline{r})$. Additionally, in heavier elements, the core electrons can reach relativistic kinetic energies, requiring use of the Dirac equation[2] instead of the Schrödinger equation. All of these problems, however, can be avoided by moving from an all-electron calculation to one involving *pseudopotentials*: collective potentials describing nuclei and their core electrons that yield smoother overall potentials[94]. This approach assumes the frozen-core approximation, only valence electrons are presumed to respond to changes in local

chemical environment.

Many varieties of pseudopotential exist, each solving or guaranteeing a different set of constraints. The three most common varieties are the so-called "norm-conserving"[95, 96] and "ultrasoft"[97] pseudopotentials as well as the projector augmented-wave (PAW) method[98]. We briefly focus here on PAWs, though a more through treatment of each approach be found in the works cited above.

The KS one-electron Bloch states $\psi_{\overline{k},n}(\overline{r})$, with their many oscillations and nodes near the core, are related to a better-behaved set of smooth wave functions $\tilde{\psi}_{\overline{k},n}(\overline{r})$ by an operator $\mathcal{T}$:

$$|\psi_{\overline{k},n}\rangle = \mathcal{T}|\tilde{\psi}_{\overline{k},n}\rangle,$$

$$\mathcal{T} = \mathbf{1} + \sum_{\alpha}^{N} \sum_{i} \left(|\psi_i^{(\alpha)}\rangle - |\tilde{\psi}_i^{(\alpha)}\rangle \right) \langle p_i|, \tag{2.14}$$

where α are the nuclei, $|\psi_i^{(\alpha)}\rangle$ are (usually) the KS eigenstate solutions for an isolated atom α, $|\tilde{\psi}_i^{(\alpha)}\rangle$ are a basis of smooth functions, and $\langle p_i|$ are projector functions with the property $\langle p_i|\tilde{\psi}_j^{(\alpha)}\rangle = \delta_{i,j}$. The transformation $\mathcal{T}$ allows us to solve for the smooth function $\tilde{\psi}_{\overline{k},n}(\overline{r})$ instead of the oscillating function $\tilde{\psi}_{\overline{k},n}(\overline{r})$ when calculating the KS Bloch states, drastically reducing the required size of the basis set. The trade-off is in knowing the isolated-atom KS eigenstates $\psi_i^{(\alpha)}(\overline{r})$, but these must only be calculated once per element. Via the frozen-core approximation, the isolated-atom core electron eigenstates from each atom α are used as the first n KS eigenstates of the calculation, and are never allowed to change.

2.1.4 The Trouble with Transition Metals

Despite the complex stack of assumptions and approximations made to get to this point, DFT works spectacularly well and is considered an "incredible success"[24]. In addition to the tens of thousands of papers[7] successfully utilizing DFT to predict the properties of real materials, many broader studies of DFT applied to a general *class* of materials have been published, demonstrating the (generally) small errors between the results of a suitably-chosen approach and reality[88, 99–108]. Even more reassuring is the work of Lejaeghere, *et al*, who have demonstrated the excellent agreement in calculated properties using vastly different implementations of DFT across broad classes of materials[109]. However, several "spectacular failures"[36] also persist, nearly all of which are related to the limitations of presently available XC functionals.

Transition metals (TMs), especially alloys of *multiple* TMs, pose an especially challenging problem for DFT[38]. The electronic structure of TMs, characterized by a partially-filled localized d-shell and a partially or fully filled delocalized s-shell, yields metals with a rainbow of colored oxidation states. The interplay of strongly localized d and delocalized s electrons (shown in Figure 2.1) are also what make TMs especially problematic for the development of accurate yet transferable functionals and pseudopotentials. A more complete treatment of the subject is covered in References [24, 35–38], and an in-depth example can be found in Chapter 3. Here, we will provide only the briefest overview of the types and origins of issues DFT calculations of TMs can run into.

The most consequential error present in modern functionals applied to TMs is the self-interaction error (SIE)[36]. In layman's terms, SIE is the unphysical effect of an electron "seeing itself", an effect of the $\rho(\overline{r})\rho(\overline{r}')$ term in the Hartree energy. If we briefly

[7] the list of papers citing Reference [20] is a good start; as of September 2017 Elsevier counts more than 20,000 citations!

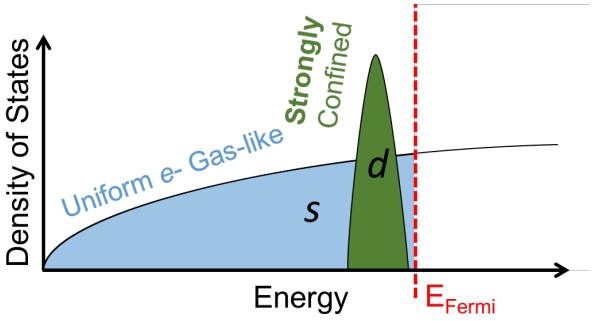

Figure 2.1: Cartoon showing the delocalized nature of the s states and the localized nature of the d states. The LDA functional can very effectively treat the uniform-electron-gas-like s electrons, but not the d electrons, which more closely resemble a harmonic potential.

consider electrons as distinguishable point charges, this is equivalent to an electron i at $\overline{r}$ feeling the effect of *all* point charges at every $\overline{r}'$... including the electron i itself! This erroneous contribution results in a fictitious delocalization of the electron density, leading to significant errors when simulating TMs, where the chemically significant d-states should be tightly bound. But if SIE originates from the Hartree term, how is it related to the XC functional?

The answer is subtle, and is most easily demonstrated by considering the exact Hartree-Fock electron-electron interaction energy of the Slater-determinant wavefunction, and comparing it to the Hartree energy used in DFT:

$$\langle \Psi_{KS} | \frac{1}{2} \sum_i \sum_{j \neq i} \frac{1}{|\overline{r} - \overline{r}'|} | \Psi_{KS} \rangle =$$

$$\frac{1}{2} \sum_i \sum_{j \neq i} \int \mathrm{d}\overline{r} \mathrm{d}\overline{r}' \frac{\psi_i^*(\overline{r}) \psi_i(\overline{r}) \psi_j^*(\overline{r}') \psi_j(\overline{r}')}{|\overline{r} - \overline{r}'|} - \frac{1}{2} \sum_i \sum_{j \neq i} \int \mathrm{d}\overline{r} \mathrm{d}\overline{r}' \frac{\psi_i^*(\overline{r}) \psi_j(\overline{r}) \psi_j^*(\overline{r}') \psi_i(\overline{r}')}{|\overline{r} - \overline{r}'|} =$$

$$\frac{1}{2} \sum_i \sum_{j} \int \mathrm{d}\overline{r} \mathrm{d}\overline{r}' \frac{\psi_i^*(\overline{r}) \psi_i(\overline{r}) \psi_j^*(\overline{r}') \psi_j(\overline{r}')}{|\overline{r} - \overline{r}'|} - \frac{1}{2} \sum_i \sum_{j} \int \mathrm{d}\overline{r} \mathrm{d}\overline{r}' \frac{\psi_i^*(\overline{r}) \psi_j(\overline{r}) \psi_j^*(\overline{r}') \psi_i(\overline{r}')}{|\overline{r} - \overline{r}'|} =$$

$$\int \mathrm{d}\overline{r} \mathrm{d}\overline{r}' \frac{\rho(\overline{r}) \rho(\overline{r}')}{|\overline{r} - \overline{r}'|} - \frac{1}{2} \sum_i \sum_{j} \int \mathrm{d}\overline{r} \mathrm{d}\overline{r}' \frac{\psi_i^*(\overline{r}) \psi_j(\overline{r}) \psi_j^*(\overline{r}') \psi_i(\overline{r}')}{|\overline{r} - \overline{r}'|}$$

Something very subtle has happened when going between the second and third lines. Specifically, we have changed the interior sum over the eigenstates from $j \neq i$ to all j, to be able to substitute in $\rho(\overline{r}) = \sum_i \psi_i^*(\overline{r})\psi_i(\overline{r})$. This adds a pair of terms of the form:

$$\pm \int \mathrm{d}\overline{r}\mathrm{d}\overline{r}' \frac{\psi_i^*(\overline{r})\psi_i(\overline{r})\psi_i^*(\overline{r}')\psi_i(\overline{r}')}{|\overline{r} - \overline{r}'|}.$$

As we can see, in Hartree-Fock theory this self-interaction term, present in the Coulomb energy sum, is exactly cancelled by an equal but opposite term in the exchange energy sum. But in DFT, where the exchange energy sum over inner products between different eigenstates is replaced by a mean-field approximation of the exchange, the exact cancellation is lost. The perfect functional would, by definition, exactly account for the SIE of the Hartree term, but thus far even imperfect functionals promising zero SIE have been "around the corner" for several decades[26].

The correlation portion of the XC energy can also be troublesome, especially in functionals *above* the LDA level of complexity. This error arises from the way in which many functionals rely on a measure of correlation developed originally for use with LDA exchange. In LDA, the correlation is fit to the difference between Ceperley and Alder's quantum MC calculation of the total energy of the uniform electron gas[16], and a calculation of $T_S + V_H + V_{X,LDA}$ for the uniform electron gas. For the uniform electron gas, the exchange term can be directly calculated. This means, however, that the residual correlation term pairs with the LDA exchange energy, such that any cancellation of errors that may exist is lost if either the exchange or correlation parts are changed. However, the space of correlation functionals is far less well-developed than that of exchange functionals, and so, the LDA correlation is often embedded into more sophisticated functionals either verbatim or with minor adjustments[35]. One example is the very popular PBE functional, which utilizes the LDA correlation as a parameter in the PBE correlation

expression[89]. While not unique to TMs, the very localized and highly correlated nature of the d electrons present in TMs exaggerates the importance of correctly estimating the correlation energy.

Construction or choice of a good pseudopotential is, often, as much art as science[35]. Despite being considered an *ab-initio* technique in materials science, there are many DOFs, and hence choices to be made, when selecting a pseudopotential. In TMs especially, the phrase "valence electron" can be very ambiguous. Naively, the localized d electrons could be presumed not to participate in bonding, and therefore should be held constant. Instead, it is often necessary to leave the s and p electrons *below* those d electrons as valence states to get the correct[8] answer! The problem only grows worse for magnetic materials (having neglected the concept of "spin" in our analysis until now), where different polarizations of the d electron levels can strongly influence otherwise inert semi-core states. This issue has, however, been partially resolved with the advent of inexpensive computing making large, complex basis sets computationally feasible, and as the results of Lejaeghere, *et al*, demonstrate, the most modern pseudopotential approaches are indistinguishable from equivalent all-electron calculations.

Heavier TMs experience non-trivial spin-orbit coupling (SOC) and relativistic effects. The influence of either (or both) require use of the Dirac equation rather than the Schrödinger equation as a starting point for DFT. Among other challenges, a DFT approach to the Dirac equation requires functionals of the *current*, of which presently there are exceptionally few. However, the Dirac question can be broken up via the Gordon decomposition[110], yielding a spin-dependent and orbital-dependent term, the latter of which is then neglected. What results is called the "scalar relativistic" treatment, and utilizes four-component spinors instead of the usual spin-up and spin-down wave functions. The orbital momentum, yielding the SOC, is then added back in as a corrective

[8] "correct" meaning "matching an all-electron calculation"

term. Standard DFT software, e.g., VASP, allows for calculations with SOC corrections, but the computational expense is immense and often impractical[9]. The validity of adding on the SOC as a perturbation is also dubious:

> "Simply put, if the [spin-orbit] coupling is large enough to make a difference in the calculations, it is also too large to be treated as a perturbation."[38]

The electronic structure of TMs generally necessitates additional computational complexity and cost. Compared to insulators, an order of magnitude more k-points in the IBZ are required to accurately simulate TMs, as the Fermi surface must be densely sampled. In addition, a large basis set may be required in order to represent d and s states simultaneously. Finally, TM calculations can require smearing of states near the Fermi surface, to stabilize the correct occupations at the cost of more k-points. While a computational rather than scientific problem, the resource use of TM calculations poses problems by impeding the practical applicability of more accurate, yet technically complex, functionals.

Despite these issues, even in TMs DFT (usually) performs exceedingly well. Although Chapter 3 focuses on a failure case, Chapters 5 and 6 detail a success story where DFT was used to explain unusual and unexpected experimentally-observed behaviors. More generally, the future for DFT is incredibly bright! The accuracy and reliability of the technique, combined with new high-throughput approaches, are beginning to make DFT a *replacement for*, rather than a *supplement to*, experiment. Moore's law continues to hold, and with that, techniques deemed computationally impractical a decade prior are being reexamined as larger and larger calculations become practical. Projects requiring calculations of thousands of configurations, containing between a dozen and a hundred

[9]Quoting from the VASP wiki on the LSORBIT tag: "Generally be extremely careful, when using spin-orbit coupling: energy differences are tiny, k-point convergence is tedious and slow, and the computer time you require might be infinite"

atoms, are now routine. And machine learning techniques are being applied to the mountains of data already produced[111–116], and new insights about fundamental materials relationships are being derived.

2.2 Cluster Expansions

We now have all the tools necessary to calculate the electronic ground state of a complex, many-atom, many-many-electron system. However, DFT is orders of magnitudes too slow to use directly in a stochastically-evaluated thermodynamic calculation. Instead, we can use the results of a set of DFT calculations to parameterize a faster, but more limited, Hamiltonian specialized for *one* problem in *one* system. The approach used in this work, the CE (Cluster Expansion) formalism[28–30, 117, 118], coarse-grains the electronic and ionic DOFs in 3D space onto an occupation variable inside a microstate vector. Three assumptions are made here:

1. all atoms live on a lattice, and do not significantly deviate from their equilibrium lattice sites,

2. each microstate, defined as a vector of occupations on the lattice, uniquely defines the energy,

3. the total energy is an additive function of local configurations.

Assumption 1 encodes two properties: that our system hasn't melted or sublimated, and that our system hasn't undergone a structural phase transition. As long as this assumption is satisfied, our Hamiltonian will not undergo any surprising changes in functional form while exploring thermodynamic state space. Assumption 2 is a result of the HK theorems: although the density $\rho(\overline{r})$ is not used in the CE formalism, there is still one

$\rho(\overline{r})$ which minimizes the energy for a given atomic configuration, and the many-body ground state is still a unique functional of $\rho(\overline{r})$. The ground state here is assumed to include structural relaxations, which are also uniquely defined by the occupation of the lattice (otherwise the first assumption is violated). We therefore do not need to keep track of, or even have a concept of, atomic position vectors; every relevant DOF is defined by the lattice site indices and their occupants. Assumption 3 allows us to define a *local* energy expression, then sum over all primitive cells in the supercell, making the Hamiltonian trivially extensive and linearly scaling in time complexity with the number of primitive cells.

The sites of the lattice are indexed from 0 to $N-1$, using index i. Each site contains an occupational DOF, σ_i, which can be expressed in either a spin ($\sigma_i \in \{-1,+1\}$) or occupation ($\sigma_i \in \{0,1\}$) basis. The microstate is defined as $\overline{\sigma} = \{\sigma_0, \sigma_1, \ldots, \sigma_{N-1}\}$. We can define clusters on the lattice as a collection of indices, $i \in \delta$, and the corresponding cluster functions as operations that take the microstate $\overline{\sigma}$ and produce a scalar dependent only on the occupations of sites in cluster δ:

$$\phi_\delta(\overline{\sigma}) = \prod_{i\in\delta} \sigma_i. \tag{2.15}$$

An example of cluster functions being constructed on a lattice is illustrated in Figure 2.2.

The cluster functions form a complete, orthonormal basis over state space: $\langle \phi_a, \phi_b \rangle = \delta_{a,b}$. We can therefore expand any scalar property, e.g., the energy E, in the basis of clusters:

$$E(\overline{\sigma}) = \sum_\delta V_\delta \phi_\delta(\overline{\sigma}), \tag{2.16}$$

$$V_\delta = \langle \phi_\delta | E \rangle, \tag{2.17}$$

where the V_δ are effective cluster interactions (ECIs) with units of energy. The sum

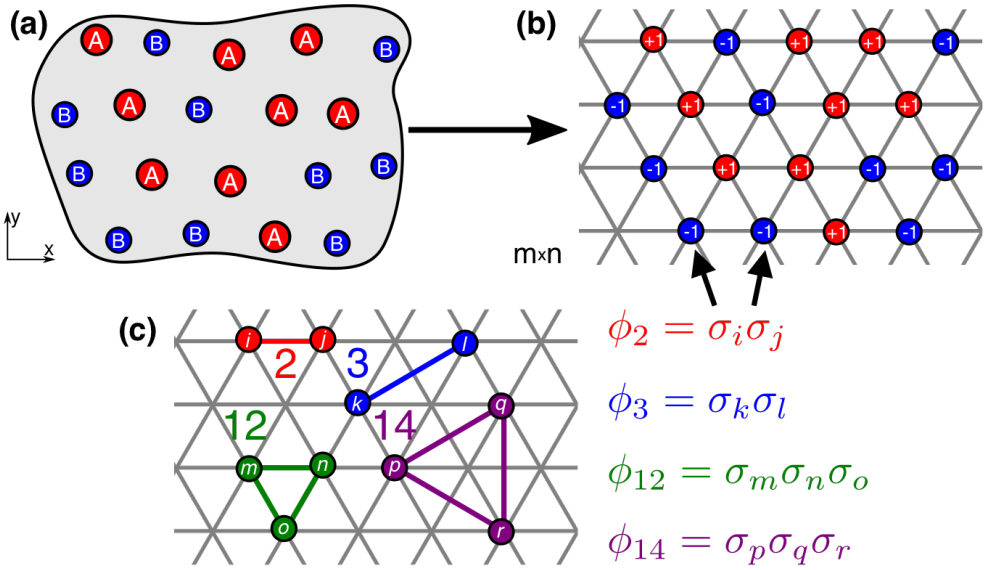

Figure 2.2: Starting with atoms in a box (a), the relaxed sites are mapped onto their equilibrium lattice positions (b). Lattice sites are assigned a σ_i of ± 1 depending on whether an A or a B sits on the site. Cluster functions, shown in (c), are defined as products of spins belonging to a collection of sites, e.g., the nearest-neighbor pair (ϕ_2).

runs over all unique clusters δ in the simulation supercell, which for a supercell containing n sites, equals $\sum_{i=0}^{n} \binom{n}{i} = 2^n$. To store 2^n floating-point ECIs for a trivial system with 100 sites would require more than 10^{21} GB of memory[10]! However, the vast majority of the ECIs are redundant. To ensure that a microstate $\overline{\sigma}$ uniquely defines the energy, we require that operations that produce degenerate microstates also produce degenerate energies, i.e., $E(\overline{\sigma}) = E(\mathcal{T}\overline{\sigma})$, where $\mathcal{T}$ is some transformation re-indexing the lattice sites. As our systems are periodic supercells of primitive lattices, the set of available degenerate operations $\{\mathcal{T}\}$ is defined by the symmetries of the lattice, including translational symmetry. What does this mean for our ECIs?

Consider a 1D periodic chain of three sites, indexed as 1, 2, and 3. The energy is:

[10] and *running* enough DFT calculations to solve for that many ECIs would take a lifetime

$$E(\overline{\sigma}) = V_0 + V_1\sigma_1 + V_2\sigma_2 + V_3\sigma_3 + V_{1,2}\sigma_1\sigma_2 + V_{2,3}\sigma_2\sigma_3 + V_{3,1}\sigma_3\sigma_1 + V_{1,2,3}\sigma_1\sigma_2\sigma_3.$$

Now apply a translation $\mathcal{T}$, such that the labels shift $1 \rightarrow 2$, $2 \rightarrow 3$, and $3 \rightarrow 1$. The energy is then:

$$E(\mathcal{T}\overline{\sigma}) = V_0 + V_1\sigma_2 + V_2\sigma_3 + V_3\sigma_1 + V_{1,2}\sigma_2\sigma_3 + V_{2,3}\sigma_3\sigma_1 + V_{3,1}\sigma_1\sigma_2 + V_{1,2,3}\sigma_2\sigma_3\sigma_1.$$

This energy $E(\mathcal{T}\overline{\sigma})$ must be the same as $E(\overline{\sigma})$ for every available microstate in state space. The same is also true of the energy of $(\mathcal{T}\mathcal{T}\overline{\sigma})$ (where $1 \rightarrow 3$, etc.). The only condition that satisfies the energy equality for every microstate and for every translation is $V_1 = V_2 = V_3$ and $V_{1,2} = V_{2,3} = V_{3,1}$. Our energy expression is now:

$$E(\mathcal{T}\overline{\sigma}) = V_0 + V_a(\sigma_1 + \sigma_2 + \sigma_3) + V_b(\sigma_1\sigma_2 + \sigma_2\sigma_3 + \sigma_3\sigma_1) + V_c(\sigma_1\sigma_2\sigma_3),$$

which contains three collective pieces of information: the site clusters, the pair clusters, and the triplet cluster. This is the same amount of information originally present in our microstate: $\sigma_1, \sigma_2, \sigma_3$. The original set of seven clusters, with no symmetry operations applied, contained *too much* information.

Taking this principle and applying it more generally: clusters that are identical under a symmetry operation of the lattice must also have identical ECIs. We can define a series of prototype clusters which are unique under symmetry operations of the lattice. Each prototype cluster α defines an orbit Ω_α, containing all clusters δ that map onto α via the symmetry operations of the lattice. The energy expanded in the basis of clusters is now:

$$E(\overline{\sigma}) = \sum_{\alpha} V_{\alpha} \sum_{\delta \in \Omega_{\alpha}} \prod_{i \in \delta} \sigma_i. \tag{2.18}$$

The space of possible α depends on the size of the simulation cell, the connectivity of the primitive cell, and the symmetry of the primitive cell. However, it is virtually never the case that more than 100 clusters are needed, with 20-50 usually being sufficient. We hope that the V_{α} are monotonically decreasing both with increasing cluster radius ($\max[r_{i,i'} \forall i, i' \in \delta]$) and/or with cluster complexity ($\sum_{i \in \delta} 1$). This is a repeat of assumption 3, in claiming that the energy is a sum of *local* properties (or at least, that any long-range interactions have $V_{\alpha} <$ our error tolerance). All that remains is to determine which clusters are required, and solve for their ECIs.

Construction of a CE Hamiltonian proceeds, typically, via the following steps:

1. Define a primitive cell and specify the DOFs of each lattice site
2. Define a CE Hamiltonian via a maximum cluster radius r_{cut} and a maximum complexity C
3. Enumerate symmetrically-distinct configurations containing up to $C + \Delta$ atoms, plus any experimentally-known thermodynamic ground state configurations
4. Calculate the formation energies of the configurations in step 3, usually using DFT
5. Fit Hamiltonian of step 2 using the energies of step 3
6. If the Hamiltonian does a poor job of predicting energies, increase its size or complexity and return to step 3
7. Enumerate additional symmetrically-distinct configurations containing up to $D > C + \Delta$ atoms, and evaluate their energies using the Hamiltonian

8. If the Hamiltonian predicts thermodynamic ground states which do not have DFT-calculated energies, add those ground states to the set of configurations, then return to step 3.

Most of the actual work involved in constructing a Hamiltonian is in steps 4 and 5. Traditionally, DFT calculations are performed for 100-300 configurations, yielding approximately two orders-of-magnitude more data points than goal number of clusters, and two to three times as many data points as clusters should be present. A good rule of thumb is for the system to be overdetermined by at least a factor of three. Higher numbers are better to ensure a well-conditioned solution, because the problem is sparse, that is, most clusters in the Hamiltonian should have $V_\alpha \sim 0$. The general regression problem being solved in step 5 is:

$$\overline{E}_{DFT} = \overline{\overline{\Phi}} \cdot \overline{V}^{\mathsf{T}}, \tag{2.19}$$

where $\overline{E}$ is a vector of energies, with rows equaling different microstates, $\overline{\overline{\Phi}}$ is a matrix of cluster functions, with rows equaling microstates and columns equaling different clusters α, and $\overline{V}$ is a vector of ECIs, which we want to solve for. The use of capital Φ denotes the extensive cluster function, $\Phi_\alpha(\overline{\sigma}) = \sum_{\delta \in \Omega_\alpha} \prod_{i \in \delta} \sigma_i$. The Φ_α, differ from the correlations $\varphi_\alpha(\overline{\sigma})$ conventionally defined in the literature[28]:

$$\varphi_\alpha(\overline{\sigma}) = \frac{\sum_{\delta \in \Omega_\alpha} \phi_\delta(\overline{\sigma})}{m_\alpha N_P}, \tag{2.20}$$

where N_P is the number of primitive unit cells in the crystal and m_α is the multiplicity of cluster α per primitive unit cell. Φ_α and φ_α are then related by a factor of $m_\alpha N_P$, such that Φ_α scales with the size of the crystal. This extensive property will prove useful in applying Legendre transforms to develop thermodynamic potentials for ensembles

of fixed extensive cluster functions. Otherwise, the vectors and matrices entering into Equation 2.19 are usually normalized to be per primitive cell.

Once we have *a* model, we continue with the loop above until we have a *satisfactory* model. A satisfactory model generally predicts energies of low-energy structures with accuracies on the order of ± 5 meV, with acceptable errors increasing as one looks at higher-energy microstates. High energy microstates have very low probabilities of being observed in an ensemble average, and hence, a larger error is more acceptable, as it is unlikely likely to be sampled in a statistically significant fashion. A satisfactory model should, ideally, correctly predict the set of thermodynamic ground states forming the lower half of the convex polytope in energy-composition space, i.e., the lower convex hull. In reality, if one is only concerned with sampling compositions in a neighborhood around some composition x^* $x = x^* \pm \delta$, poor performance far from x^* is acceptable, including the prediction of incorrect ground states (especially if the real material undergoes a structural transformation sufficiently far from x^*).

The final step is using the fitted Hamiltonian in MC simulations. The computational appeal of the CE becomes obvious here: to calculate the *change* in energy for a proposed move, one needs only to calculate the change in clusters that touch the involved sites. For example, consider a proposed move that changes flips the spin of site i. The change in energy is:

$$\Delta E(\Delta\sigma_i) = -2 \sum_{\alpha} V_\alpha \sum_{\delta \in \Omega_\alpha}^{i \in \delta} \phi_\delta(\overline{\sigma}),$$

where the inner sum is over only individual clusters δ which touch site i. The factor of $-2\phi_\delta(\overline{\sigma})$ comes from the change in $\Phi_\alpha(\overline{\sigma})$ being $-\phi_\delta(\overline{\sigma}) + (-1)\phi_\delta(\overline{\sigma})$. The application of (-1) to $\phi_\delta(\overline{\sigma})$ flips the spin of site i in δ. If the move is accepted, all of the affected $\phi_\delta(\overline{\sigma})$ are then updated. The time complexity of moves is therefore linear in the *number of*

clusters in the Hamiltonian, not in the number of sites in the supercell. Armed with this massive reduction in difficulty, we can easily sample tens of thousands of configurations for supercells containing themselves tens of thousands of sites!

Lest the reader believe the CE formalism be limited to only two-state systems: extensions to both the spin and occupation basis exist for systems with an arbitrary number of components. In addition, systems with multiple independent DOFs, e.g., magnetism *and* composition (where σ_i becomes a vector) are discussed in Chapter 6. As we have hinted at before, we are not limited to only expanding the energy, either. Any scalar[119–123] (or tensor[124]) product of the lattice occupation DOFs can be expanded in the orthonormal basis provided by the clusters, and hence, sampled over. If $E(\overline{\sigma})$ is the CE Hamiltonian, let $X(\overline{\sigma})$ be any other ground state property of the configuration. Then, we can simply sample over the microstates using E and measure X to replicate the following ensemble average:

$$\langle X \rangle = \frac{\sum_{\overline{\sigma}} X(\overline{\sigma}) \exp\left[\frac{E(\overline{\sigma})}{k_b T}\right]}{\sum_{\overline{\sigma}} \exp\left[\frac{E(\overline{\sigma})}{k_b T}\right]}. \tag{2.21}$$

Cluster Expansions and Sparsity

Solving for a sparse Hamiltonian, or in general, the problem of sparse regression has been the subject of many doctoral theses in its own right. Broadly, the techniques used fall into two categories: (a) approaches that select a set of features, then perform regression, and (b) approaches that perform feature selection and regression in one step. Examples of category (a) are evolutionary approaches, where e.g., a genetic algorithm[125] is used to select features, regression is performed, and the root-mean-squared error or cross-validation score are used to evaluate fitness. Examples of category (b) include penalized regression, e.g., ridge regression or LASSO regression[126], as well as Bayesian approaches

to penalized regression[127, 128]. In addition, there is the matter of choosing weights for different samples (microstates), and the definition of testing and training sets for calculation of cross-validation scores. These subjects are touched upon in the following chapters, and the citations used there can be followed to more in-depth treatments of the materials.

2.3 Computational Methods

In Chapters 3, 5, and 6, a sizeable [11] [12] [13] number of electronic structure calculations are performed. In all cases, the Vienna *Ab Initio* Simulation Package (VASP)[20–22, 129] was used: version 5.3.5 from 2012-2014, and 5.4.1 from 2015 onward. All calculations utilized projector-augmented wave[98, 130] (PAW) pseudo-potentials, using dataset v.54. Specific PAWs for each element were chosen using the guidelines at `https://cms.mpi.univie.ac.at/vasp/vasp/Recommended_GW_PAW_potentials_vasp_5_2.html`. Unless otherwise indicated, the generalized gradient approximation of Perdew, Burke, and Ernzerhof (PBE) was used for the exchange energy[89] and the interpolation formula of Vosko, Wilk, and Nusair was used for the correlation energy[131]. With noted exceptions in Chapter 5, all calculations were performed using spin polarized densities.

All calculations utilized Γ-centered Monkhorst-Pack k-point grids[132] using either the first order Methfessel-Paxton method[133] (for relaxations) or the tetrahedron method with Blöchl corrections[134] (for static runs) to integrate over electronic energy levels. Both the energy cutoffs and the k-point grid densities were chosen via a convergence method. First, the k-point meshes were converged: the number of divisions along the shortest real-space dimension were increased in integer steps (with the divisions in the

[11] Approximately 4,000 unique calculations over five years; in 2014 I alone accounted for for $> 65\%$ of CNSI's computer cluster use!

[12] My work at Sandia, however, has lead me to carry out $> 100,000$ unique calculations

[13] I fear for the electricity bill of my future employer

other two directions adjusted inversely-proportionately) until the change in energy per step dropped below 1 meV. Next, a similar process was carried out with the energy cutoff: starting with 1.5 the largest value in the elemental pseudopotential files, the cutoff was increased in steps of 10 eV, until the change in energy per step dropped below 1 meV. These convergences were carried out for both end members in every binary surveyed, and the denser mesh and largest energy cutoff from the pair was used. For supercell calculations, the k-point mesh was scaled appropriately.

Generally speaking, two categories of calculations were carried out: relaxations and static calculations. Relaxations allowed for the cell shape and size and/or the internal ionic DOFs to relax. For these calculations, the ionic self-consistency loops were terminated when forces became smaller than 10^{-2} eV/Å. If both (a) the cell shape or size were allowed to relax and (b) the relaxation took more than three ionic steps, another relaxation was performed. This is because the basis set utilized by VASP is initialized at the start of a calculation, based on the starting geometry, and then never changed, *even if the geometry changes significantly.* All relaxations performed were followed by a static calculation. While specific static calculations utilized different settings depending on the goal (e.g., to obtain a density-of-states, or to determine very accurately the internal forces), all static runs shared one feature: the ionic DOFs were *never* allowed to change. Electronic self-consistency loops were terminated with energy differences of, at most, 10^{-4} eV for relaxations and 10^{-6} eV for static calculations.

In addition to VASP, the CASM (a Clusters Approach to Statistical Mechanics) software package[31, 135–137] was used in all Chapters to enumerate supercells, manage simulations, fit CEs, and perform MC simulations. Since joining the Van der Ven group in 2013, CASM has undergone two complete overhauls and numerous major, feature-breaking revisions[14]. Difficulties aside, however, CASM contains multiple incredibly pow-

[14]Not to mention how Byzantine the codebase has become: even glancing at the source repo has made

erful features regarding structure enumeration, symmetry analysis, data analysis, and the "clexulator". The general features of the code are illustrated in Figure 2.3. Additional software to automate the fitting of CE Hamiltonians from ensemble measurements was written for Chapter 4, while modifications to CASM to handle magnetic DOFs were written for Chapter 6. The author's contributions to the CASM codebase can be found at `github.com/prisms-center/CASMcode/commits/0.2.X?author=tallakahath`.

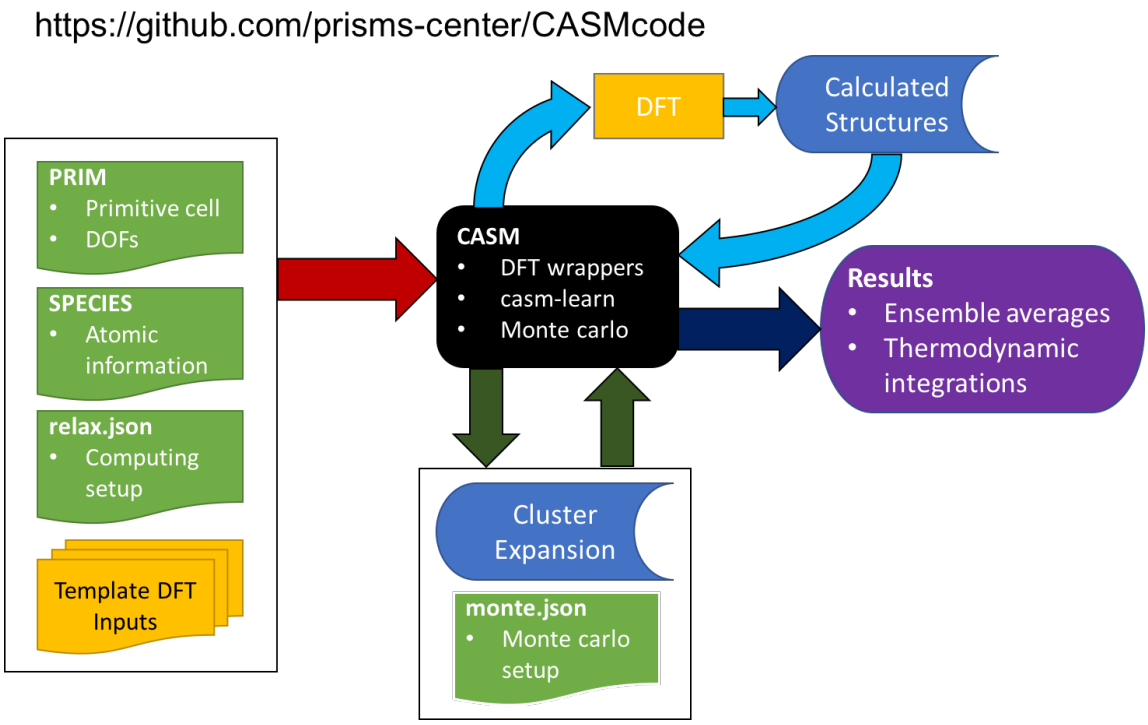

Figure 2.3: Diagram illustrating the high-level features available in CASM. The operation of CASM can be generally divided into three categories: (1) setting up and carrying out *ab-initio* calculations, (2) constructing and fitting CE Hamiltonians to data, and (3) performing MC simulations. The majority of the author's contributed code lives in the small yellow box labeled "DFT", concerning the wrapping of VASP.

Google software engineers cry out in fear

Chapter 3

Testing Predictions from Density Functional Theory at Finite Temperatures: β_2-Like Ground States in Co-Pt

> When teaching chemistry students, I explain that DFT is some algorithm meaning unreliable, while ab initio is Latin for too expensive.
>
> *Kieron Burke*, from "Perspective on density functional theory"

In this Chapter, we perform a critical assessment of the accuracy of density functional theory methods in predicting stable phases within the Co-Pt binary alloy. The statistical mechanical techniques in Section 2.2 are applied to density functional theory calculations to yield finite-temperature results directly comparable to experimental measurements. The predicted temperature-composition phase diagram of Co-Pt is shown to be

qualitatively incompatible with experimental observations, indicating that the predicted long-period superstructure ground states are fictitious. We explore in-depth exactly how density functional theory can fail for transition metals, building on the framework laid in Section 2.1. We also show that recently suggested methods to better align density functional theory and experiment via the hybrid functional HSE06 are unable to resolve the discrepancies in this system. Our results indicate a need for better verification of density functional theory based phase stability predictions, and highlight fundamental flaws in the ability of DFT to treat late $3d$-$5d$ binary alloys.

3.1 Introduction

Density functional theory (DFT) has grown to become the most popular electronic structure calculation method to date[138]. Modern computational resources have made DFT viable as a high-throughput materials design technique[57, 90, 139], whereby the existence, stability, and properties of periodic crystalline phases are predicted entirely from first principles. These approaches are especially attractive for predicting the properties of systems that are otherwise too expensive or difficult to study experimentally, such as alloys containing Ru[59], Tc[140], and Pt[56], among others[141–144].

While remarkably successful in predicting phase stability in a wide variety of chemically disparate systems[141], the occasional failures of DFT[145–147] highlight the importance of experiments to validate such predictions. However, there exists a fundamental challenge in comparing DFT and experiments: electronic structure calculations predict zero kelvin properties, while experiments are performed at finite temperatures. The most reliable measurements of thermodynamic properties are performed at elevated temperatures, where equilibrium is more readily attained, but also where the entropic contributions to such properties are the greatest. Accuracy in comparing *ab-initio* and

experimental results is vital, because any mismatch may indicate failure in the approximations used in DFT to accurately reproduce the necessary physics.

Of particular concern are disagreements between the set of observed phases and DFT-predicted zero kelvin ground states. These errors, while more sensitive to unknown kinetic barriers or unaccounted for entropic contributions, can also indicate fundamental flaws in the *ab-initio* method. Binaries that pair late $3d$ with late $5d$ transition metals, such as Cu-Au[148, 149], Co-Pt[56, 150], Ni-Pt[56, 149, 151], Fe-Pt[56, 152], and Fe-Pd[153], represent one class of materials where DFT predicts a rich variety of zero kelvin ground states for which no experimental evidence exists. A wealth of long-period superstructures have been predicted to be stable in the intermediate continuum of compositions between x_{Pt} 0.5 and 0.75 in the $Ni_{1-x}Pt_x$, $Fe_{1-x}Pt_x$, $Co_{1-x}Pt_x$ and $Cu_{1-x}Au_x$ alloys, instead of the two phase mixtures of $L1_0$ and $L1_2$ observed experimentally. In the case of Cu-Au, Co-Pt, Ni-Pt and Fe-Pd, the $L1_2$ AB_3 structure is altogether excluded from the set of ground states, and in the case of Co-Pt, the $L1_0$ formation enthalpy is less stable than the (experimental) solid solution enthalpy[154]. In all cases, the formation enthalpies for the ordered phases have been predicted to be dozens of meV higher than experimental results[155–158]. These results derive from zero kelvin predictions, but little or no thermodynamic analysis of the finite-temperature impacts has been performed, and bulk phase diagrams deriving solely from electronic structure calculations have never previously been constructed for these materials. Co-Pt, Fe-Pt, and Fe-Pd are all candidates for use in ultrahigh density magnetic storage[159–164]; resolving uncertainties about low-temperature predictions of phase (in)stability is thus critical.

This Chapter explores the finite temperature implications of the zero kelvin ground states predicted by DFT for the $Co_{1-x}Pt_x$ alloy. We have developed a first-principles Cluster Expansion (CE) Hamiltonian and used it in semi-grand canonical Monte Carlo (MC) simulations to construct a temperature versus composition phase diagram. The

predicted phase stability is in qualitative disagreement with available experimental observations. Our calculations also indicate that long-range ordered phases persist as ground states when including corrections for spin-orbit coupling (SOC), antiferromagnetic and mixed magnetic ordering, and noncollinear magnetism. Using a hybrid functional, we have attempted to recover experimental results; however, this approach is shown to introduce new errors in the enthalpy and magnetic moments of the structures. These errors can be traced back to known failings of Hartree-Fock exchange when applied to transition metals, which we illustrate by analyzing the density of states (DOS) for $L1_0$ CoPt.

3.2 Methods

3.2.1 Electronic Structure Calculations

Details about the electronic structure calculations performed in this Chapter are available in Section 2.3. All calculations were performed spin polarized unless otherwise noted, with an energy cutoff of 460 eV and a k-point grid with $23 \times 23 \times 23$ divisions in the unit cell (and scaled with reciprocal supercell size).

3.2.2 Cluster Expansion and Monte Carlo Simulations

Configurational degrees-of-freedom (DOFs) in an alloy can be described with a CE (Cluster Expansion) Hamiltonian[28, 29] combined with MC simulations[31, 137, 165]. Details of the CE formalism can be found in Section 2.2. Being concerned with the entirety of composition space, we chose to use the spin basis (i.e., the Chebychev basis for a binary), with $\sigma_i = -1$ for Co and $\sigma_i = +1$ for Pt.

Semi-grand canonical MC simulations were performed in a $24 \times 24 \times 24$ periodic supercell with 1000 equilibration passes followed by 2000 thermodynamic-averaging passes

(where one pass is N_{sites} attempted "spin flips"). Approximate phase boundaries were identified by discontinuities in the composition-temperature lines at constant chemical potential (using temperature increments of $\Delta T = 2$ K), or by plateaus in composition-chemical potential lines at constant temperature (using chemical potential increments of $\Delta\mu = 0.01$ eV).

3.2.3 Phonons

Force constants were calculated using the frozen phonon approach[166–168], perturbing large supercells (108 atoms) with small, isolated, symmetrically-distinct atomic displacements (0.01, 0.02, and 0.04 Å). Following electronic structure calculations, the resulting force constants were used to construct the dynamical matrix[169]. Vibrational free energies[170] were then calculated using the quasi-harmonic approximation, repeating the previous procedure at a variety of slightly smaller and larger (-2% to $+10\%$) supercell volumes and using a second order polynomial to fit the dependence of the free energy on volume to determine the change in formation energy with temperature[171].

3.3 Results and Discussion

3.3.1 Zero kelvin and Finite Temperature Results for PBE

To fully characterize the *ab-initio* properties of the Co-Pt binary, we calculated the DFT energies of 1469 symmetrically-distinct orderings on the face-centered-cubic (FCC) lattice selected by an iterative approach. Each configuration was initialized ferromagnetically during the DFT calculations. We started with all known FCC based ground states as well as all symmetrically distinct orderings of Co and Pt over FCC within supercells containing up to 6 atoms. A CE was fit to these energies and subsequently used to search

for low energy configurations in larger supercells. The energies of configurations in the larger supercells that were predicted to be below or close to the convex hull with the CE were then calculated with DFT and included in a new fit. The CE was iteratively improved until no new ground states were predicted. The resulting set of structures included: (i) all unique supercells up to 6 atoms, (ii) all supercells up to 8 atoms with platinum composition between 25% and 75%, and (iii) long-period superstructure orderings involving (001) layers of Co and Pt stacked in various tilings in supercells with up to 15 atoms ($1 \times 1 \times n$ primitive cells). Additional magnetic configurations were tested; anti-ferromagnetic and mixed/ferrimagnetic orderings were explored and non-collinear magnetism with SOC corrections was separately included. The formation energies of all these configurations, calculated using hexagonally-close-packed (HCP) Co and FCC Pt as reference states, are shown in Figure 3.1.

The set of ground states predicted by PBE (red circles/lines in Figure 3.1, corresponding structures in Figure 3.2) contain a variety of ordered phases at differing compositions. Most prominent is the β_2 $CoPt_2$ ordering, characterized by alternating single (001) layers of Co and pairs of (001) layers of Pt. The $L1_0$ structure, observed experimentally through a wide range of compositions[172, 173], is predicted to be stable only in a very narrow chemical potential range as a result of the small difference between the slopes of the tie lines connecting $L1_0$ CoPt to Co_2Pt and Co_2Pt_3. The experimentally observed $L1_2$ $CoPt_3$ ordering is entirely absent from the set of ground states, excluded by the depth of the common tangent between the $CoPt_2$ and FCC Pt phases. A large number of long-period superstructures, characterized by different arrangements of (001) layers of Co and Pt and with a preference for Pt-Pt layer pairs (similar to β_2) to account for deviations in stoichiometry (instead of anti-site defects on a $L1_0$ supercell), are present along or within 5 meV of the tangent between CoPt and $CoPt_2$.

These enthalpies and ground states match the results of Chepulskii *et al.*[150] and

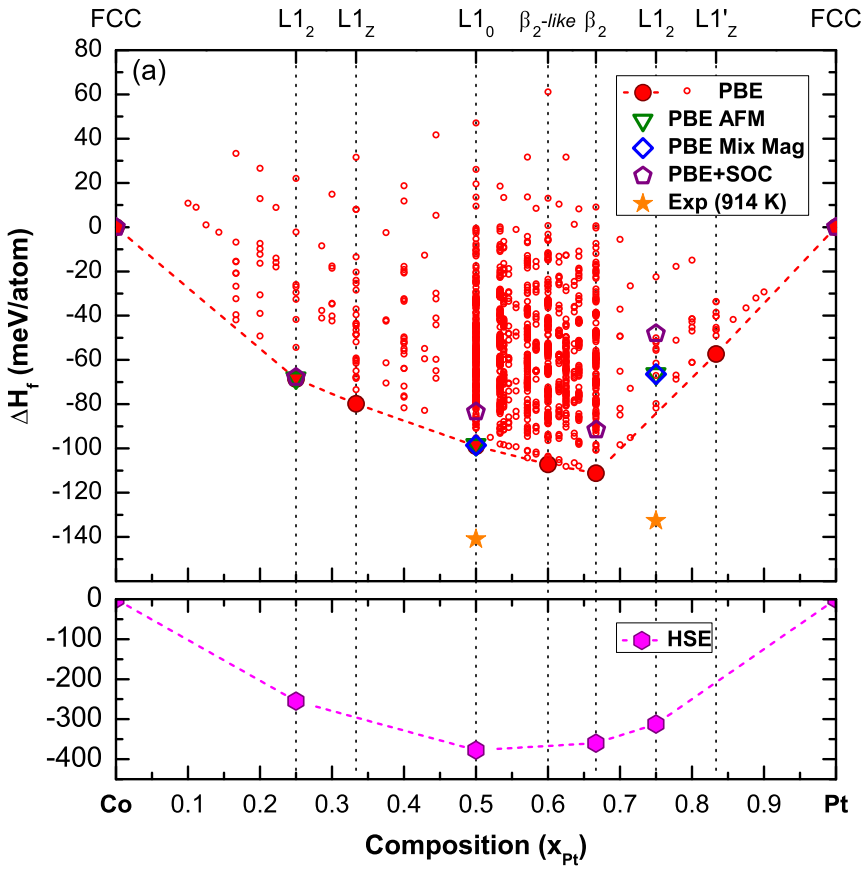

Figure 3.1: Formation energies in the Co-Pt binary as calculated using PBE and HSE06. For ground state configurations, antiferromagnetic and mixed/ferrimagnetic orderings and SOC corrections were also considered. Experimental values at 914 K are from Ref. [156].

Hart *et al.*[56], although an order of magnitude more configurations have been considered here. While both prior works have reported a stable $D0_{19}$ (HCP) phase at Co-rich compositions[56, 150], we restricted our focus to FCC-like superstructures because we are only interested in equiatomic and majority-Pt alloys (i.e., $0.25 < x_{Pt} < 0.75$), which all adopt FCC-based orderings experimentally[154].

The calculated formation energies of $L1_0$ CoPt and $L1_2$ $CoPt_3$ are approximately 50 meV above (less stable) the measured formation enthalpies at 914 K[156], i.e., an error of nearly 40%. The lattice parameters, however, are within <1% of experimen-

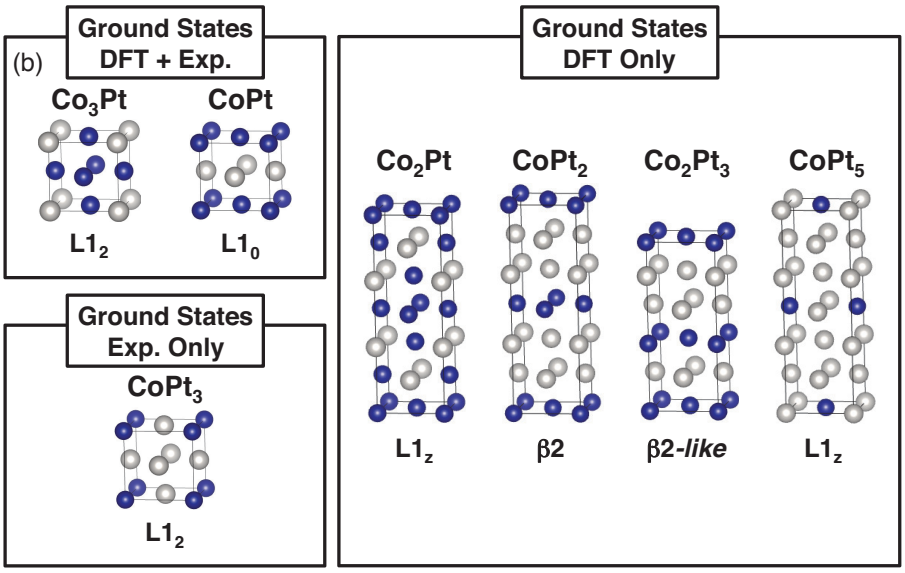

Figure 3.2: Crystal structures of the stable ground states predicted in Co-Pt using PBE (drawn with VESTA[174]). Compositions for ground states, including long-period superstructures, are indicated by dotted lines.

tal measurements[173]. Alternative magnetic configurations and SOC contributions did not result in any further lowering of the formation energies of the ground states and *increased* the difference between calculated and measured formation enthalpies [blue triangles, green squares, and purple pentagons in Figure 3.1, respectively]. Figures detailing the additional magnetic orderings shown in Figure 3.3.

The Co-Pt system forms a FCC-based solid solution at high temperatures and a variety of FCC-based ordered structures upon cooling. The contributions of configurational entropy play an important role in determining phase stability when increasing temperature. We fit[31] the coefficients of a CE to the 1469 formation energies using a genetic algorithm[125] to determine the optimal basis set. The resulting fit has 89 effective cluster interaction (ECIs) coefficients corresponding to pair, triplet, and quadruplet clusters [Figure 3.4]. The root-mean-squared error of the fit was 3.3 meV, and the cross validation score (using leave-one-out cross validation) was 3.6 meV.

The PBE-based phase diagram [Figure 3.5], determined using semi-grand canonical

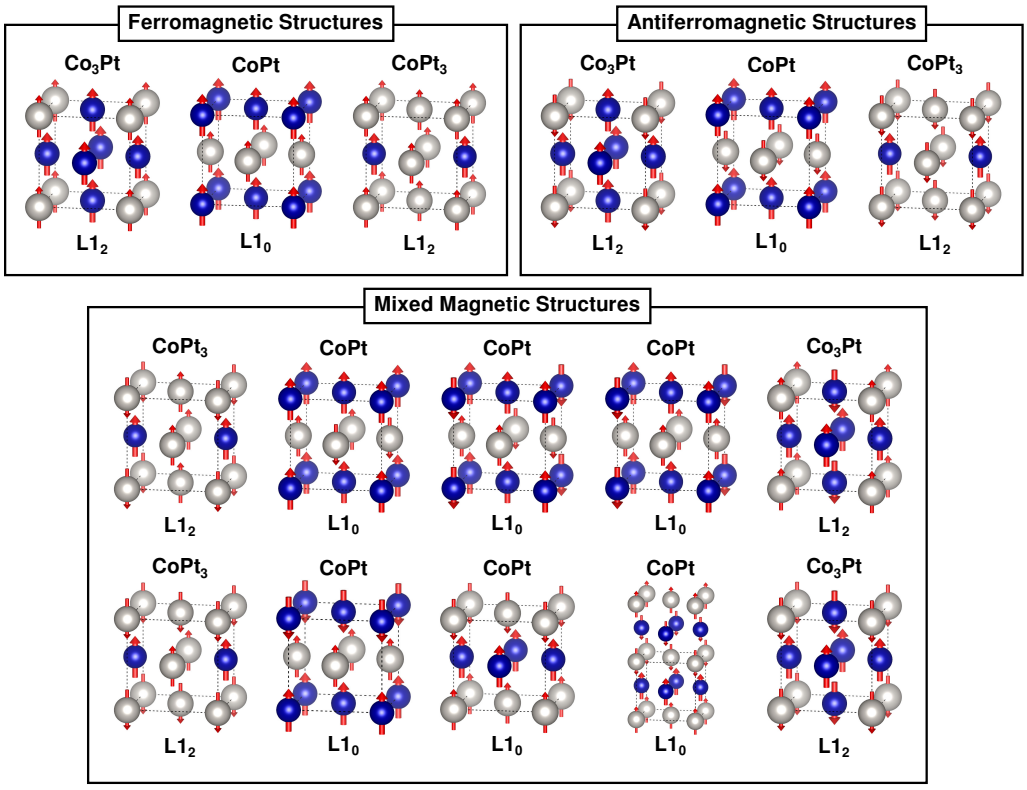

Figure 3.3: Symmetrically unique magnetic orderings used when performing electronic structure calculations. Arrows indicate the sign of the initial magnetic moment (μ_i) on a given site: $+\hat{\mathbf{z}}$ for $\mu_i > 0$, $-\hat{\mathbf{z}}$ for $\mu_i < 0$, though no coupling of magnetic moments with crystallographic directions should be inferred. Ferromagnetic orderings were used in the initial calculations of the PBE set of ground states, though the antiferromagnetic and "mixed" magnetic orderings were later examined to determine if an unusual magnetic configuration could be responsible for a change in formation energy. All figures were drawn using VESTA.

MC, shows a very wide stability region for β_2 $CoPt_2$. Although this ordering also has the highest order-disorder temperature, the transformation is predicted to occur hundreds of degrees lower than the experimental transition temperatures of $L1_0$ CoPt and $L1_2$ $CoPt_3$[172, 173, 175]. The $L1_2$ $CoPt_3$ structure does not appear at all in the calculated phase diagram, and the region surrounding $x_{Pt} = 0.5$ consists of a continuum of defected incommensurate long-period superstructures up to the peritectoid temperature, decomposing into a mixture of solid solution and β_2 $CoPt_2$. We found no evidence for the stabilization of defected $L1_0$ CoPt (i.e., single planes of Co and Pt with a random

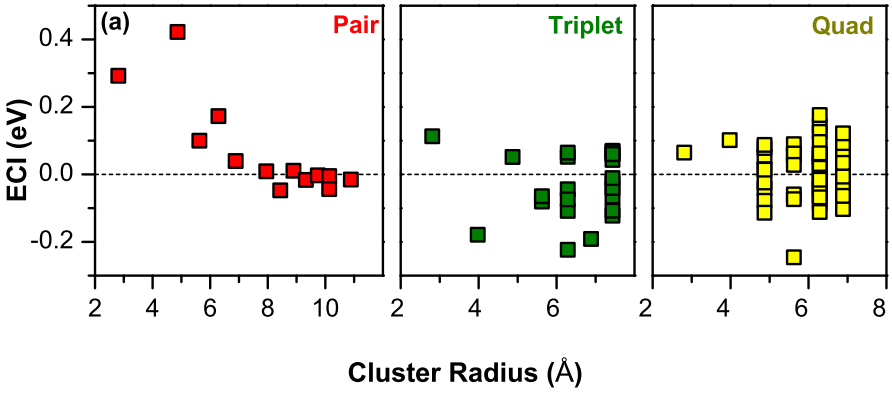

Figure 3.4: ECIs of the PBE CE Hamiltonian, grouped by cluster type. The empty and point clusters have ECIs of 20.5 meV and 473 meV, respectively.

distribution of anti-site defects); even at compositions close to $x_{Pt} = 0.5$, the structure instead resembled β_2-like Co_3Pt_5 with anti-site defects concentrated in the paired Pt-Pt (001) layers. The phase diagram was not explored below 400 K, nor were compositions below $x_{Pt} = 0.2$ or above $x_{Pt} = 0.8$ explored because these regions were not emphasized when fitting the CE.

Overall, the resulting phase diagram is inconsistent with the high temperature observations of $L1_0$ CoPt and $L1_2$ $CoPt_3$. These phases have been well characterized in the literature and have important differences in diffraction patterns from the long-period superstructures predicted by PBE. Experimental characterization of the $L1_0$ phase has historically relied upon the [001] superstructure peak[173, 176, 177], a peak that is absent in the predicted long-period superstructure orderings. $L1_2$ $CoPt_3$, having cubic symmetry, also has very different diffraction patterns from tetragonal β_2 $CoPt_2$ or any of its derivatives.

While the calculated phase diagram only accounts for configurational excitations at finite temperature, vibrational and magnetic excitations may also play a role in determining the relative stability of different orderings. To explore vibrational free energies,

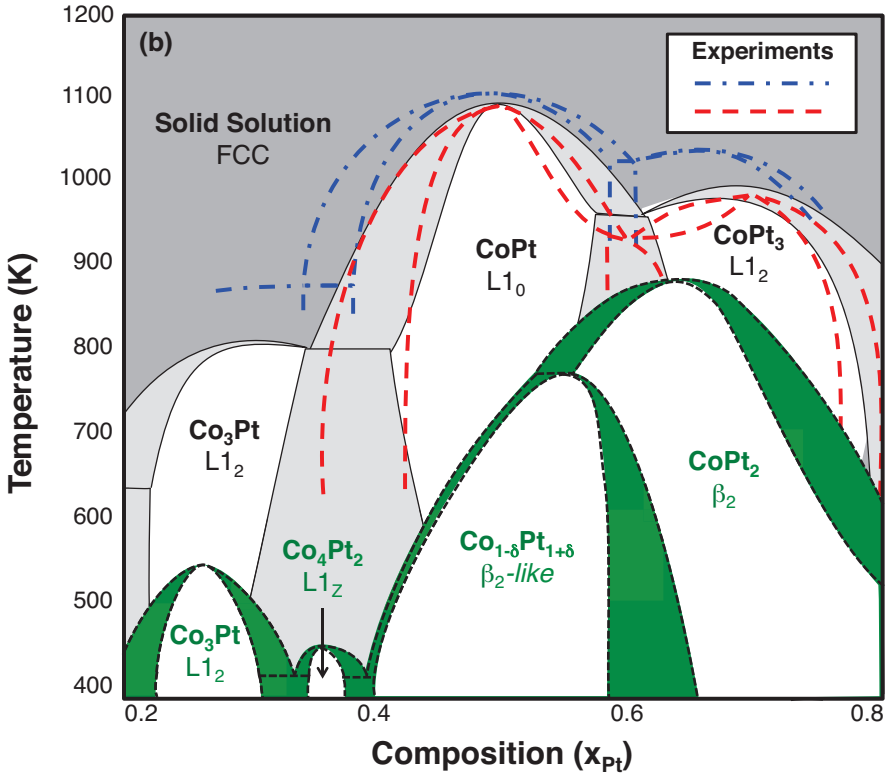

Figure 3.5: The temperature-composition phase diagrams for Co-Pt from experiments (dashed red, blue lines[172, 173, 175]), our results with PBE (green), and CALPHAD (solid black lines[154]). Green shading indicates two-phase regions.

we performed phonon calculations for FCC Co, FCC Pt, $L1_0$ CoPt, β_2 $CoPt_2$ and $L1_2$ $CoPt_3$ within the quasi-harmonic approximation. Figure 3.6 shows the modified convex hull for $L1_0$ CoPt, β_2 $CoPt_2$, and $L1_2$ $CoPt_3$ when phonon contributions are considered. However, even at 914 K, $L1_2$ $CoPt_3$ never emerges as a stable phase relative to β_2 $CoPt_2$ and FCC Pt. Furthermore, the stability of $L1_0$ CoPt relative to β_2 $CoPt_2$ and $L1_2$ Co_3Pt does not increase markedly with increasing temperature. This suggests that rigorous inclusion of a vibrational DOF, in addition to a configurational DOF using coarse-graining schemes[178, 179], are unlikely to qualitatively alter the calculated phase diagram of Figure 3.5.

Thermal excitations of magnetic moments have previously been shown to be impor-

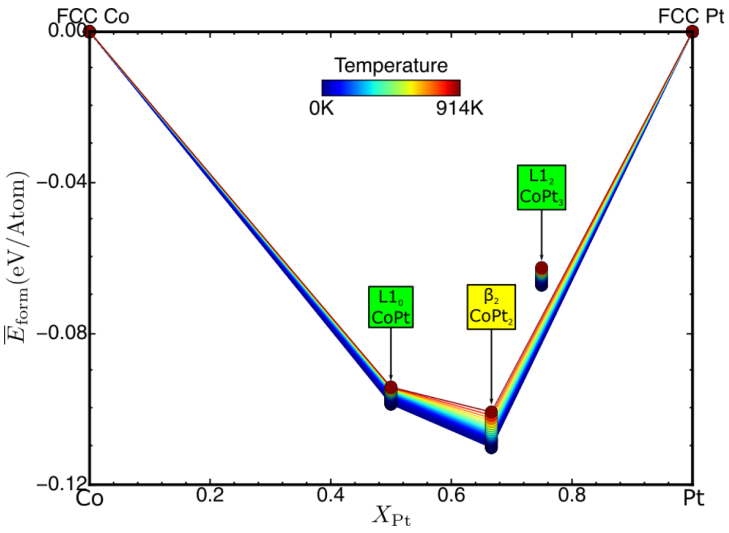

Figure 3.6: Phonon contributions to the formation energies of $L1_0$ CoPt, β_2 $CoPt_2$, and $L1_2$$CoPt_3$. Modifications to the convex hull are only slight, and the $L1_2$ phase is never stabilized, even at 914 K.

tant in affecting phase stability in Co-Pt alloys[172, 175]. In pure Co, entropic contributions arising from spin-spiral excitations have a strong influence on the HCP/FCC transformation temperature[180]. At Pt-rich compositions, the ferromagnetic to paramagnetic Curie temperatures occur below the order-disorder transition temperatures of both $L1_0$ CoPt and $L1_2$ $CoPt_3$ [154, 172, 173]. Hence, magnetic disorder, neglected in the calculation of our phase diagram, will likely play a role in determining the precise order-disorder transition temperatures. An in-depth study of the effects of magnetic entropy on the phase diagram are beyond the scope of this Chapter. However, below the Curie temperatures contributions to the free energy from magnetic entropy are expected to be small. While we do not know the Curie temperature of the β_2 phase, those of $L1_0$ and $L1_2$ are above all of our calculated solid solution transformation temperatures. In the case of the β_2 phase, there are two possibilities: (i) $CoPt_2$ remains ferromagnetically ordered up to the solid solution transformation temperature, or (ii) $CoPt_2$ becomes paramagnetic below the solid solution transformation temperature. In scenario (i) our phase diagram should be negligibly impacted by the inclusion of magnetic entropy, while in scenario (ii), magnetic entropy will only further *stabilize* the β_2 phase with respect to the $L1_0$ and $L1_2$ phases. We therefore expect that inclusion of magnetic excitations will not rectify the

disagreement between finite temperature predictions and experimental observations.

The over-stabilization of β_2 and other long-period superstructures with paired (001) Pt-Pt planes can be attributed to over-delocalized electron charge densities in PBE. Generalized gradient approximations (GGAs) can perform poorly in transition metals[37, 108, 181] where the significance of the localized d-orbitals comes into conflict with the orbital-less approach of GGA. Any functional treatment of the electron density leads to an electron interacting with its own potential, the self-interaction error (SIE), which causes excessive delocalization of the total charge. Additionally, the GGA functional can not energetically differentiate between occupied and unoccupied bands, leading to incorrect predictions for orbital/band occupation and splitting[36, 182]. Because both the energy levels and occupations of the d orbitals are incorrect, the Co $3d$ and Pt $5d$ bands cannot hybridize, losing significant enhancement of the magnetic moment[183–185]. Stabilization of a magnetic ground state, however, is a driving force in choosing the thermodynamic ground states in Co-Pt[186], and ferromagnetic effects drive the asymmetry in the phase diagram with respect to the Co-rich and Pt-rich $L1_2$ phases[172, 175].

3.3.2 Comparison with Hybrid Functional HSE06

Using a screened form of Hartree-Fock exchange, Zhang *et al.*[147] were able to recover the experimental ground-states of Au-Cu. The parametrization of the hybrid functional developed by Heyd *et al.* (HSE06)[187, 188] reduces the SIE akin to Hartree-Fock theory[102], while avoiding the associated singularity in occupation at the Fermi level. Since HSE06 explicitly includes orbitals, d-orbital hybridization can be recovered, e.g., as in Au-Cu. The functional is, however, limited by its computational expense[189] and accuracy[37, 99].

To examine the performance of the HSE06 functional, all of the PBE ground states, as well as $L1_2$ $CoPt_3$, FCC Co and Pt, and HCP Co were recalculated [pink hexagons/lines in Figure 3.1]. The results show qualitative improvement: $L1_2$ $CoPt_3$ is predicted as a ground state, and $L1_0$ CoPt is substantially more stable relative to $L1_2$ Co_3Pt and β_2 $CoPt_2$. However, the enthalpy and lattice parameter errors increase by an order of magnitude (200–300 meV and 2.5–4.5%, respectively) and β_2 remains as a ground state. These results are not surprising: HSE06 is known to severely overestimate exchange splitting in itinerant magnetic systems[99, 190, 191]. The default screening parameter in the HSE06 formalism ($\omega = 0.2$ Å^{-1}, $r_{screen} = 10$ Å) results in an effective screening length an order of magnitude greater than the length scales ($r_{screen} = 0.24 - 0.26$ Å) for screening in bulk Pt or Co metals[192], introducing spurious interactions between orbitals at different sites. This is further verified by stabilization of a *ferromagnetic* ground state for Pt in both this Chapter and Ref. [193] over the experimentally observed nonmagnetic state, and an overestimation of magnetic moments with HSE06 for *all* experimentally studied structures.

The shortcomings of both the PBE and HSE06 functionals are more easily visualized by comparing the calculated DOS (density of states) for Co-Pt (Figure 3.7) with data from experiments. The width of d-band states, as measured by photoemission[194, 195], are shown in grey in Figure 3.7, while the electron occupation at the Fermi level can be inferred from low temperature heat capacity experiments[196–198], shown as the height between the red dashed lines. In the case of HCP cobalt, PBE predicts a d-band width in good agreement with experiment, but the occupation at the Fermi level is underestimated. The excessive delocalization provided by SIE in PBE smears the electron density towards a more even distribution between orbitals, and this effect is magnified by the inability of PBE to (energetically) distinguish between occupied and empty orbitals. This latter point is exemplified by a difference between the calculated exchange splitting (energy difference

between maxima in spin-up and spin-down DOS) and the experimentally determined width, indicated in purple. Unsurprisingly, PBE performs well in FCC platinum, where the d-orbitals are fully occupied and differentiation between sub-shells does not matter. Though we were not able to find suitable experimental analysis of the $L1_0$ CoPt d-bands, Figure 3.7 shows an unexpectedly wide d-band and low electronic occupation at the Fermi level in CoPt, similar to Co.

Contrary to expectation, HSE06 worsens the degree of electronic delocalization in Co even as the SIE should be reduced; this can be attributed to the unrealistic (for Co) screening length standardized in the HSE06 functional. In Pt, a very large fictitious exchange splitting is introduced, explaining the large magnetic moment commented upon previously. Here, an electron has been promoted from the $5d$ orbitals in PBE to the $6p$ orbitals in HSE06 to increase the net number of unpaired spins. The over-stabilization of a magnetic ground state also reduces the energy of the d-orbitals in all materials; we can see this in Figure 3.7 where the occupation at the Fermi level drops to between one half and one quarter of the PBE values. These results both highlight the failures of the PBE and HSE06 functionals and offer insight as to *why* these methods describe the Co-Pt binary so poorly.

Recognizing that the screening length in HSE06 may be inappropriate for the Co-Pt binary, we explored additional screening and mixing parameters to evaluate their performance. In the spirit of Moussa, *et al*[200], we attempted to find a set of parameters that minimized the error in the DOS at the Fermi level in CoPt. Figure 3.8 shows results for different values of the mixing and screening parameter. The PBE DOS at the Fermi level is recovered when the mixing approaches zero, but by this point, the *energetics* of the PBE functional are also recovered, which we have demonstrated to be incorrect. While increasing the screening parameter (reducing the effective screening length) qualitatively improves the DOS at the Fermi level, the error is still unacceptably large.

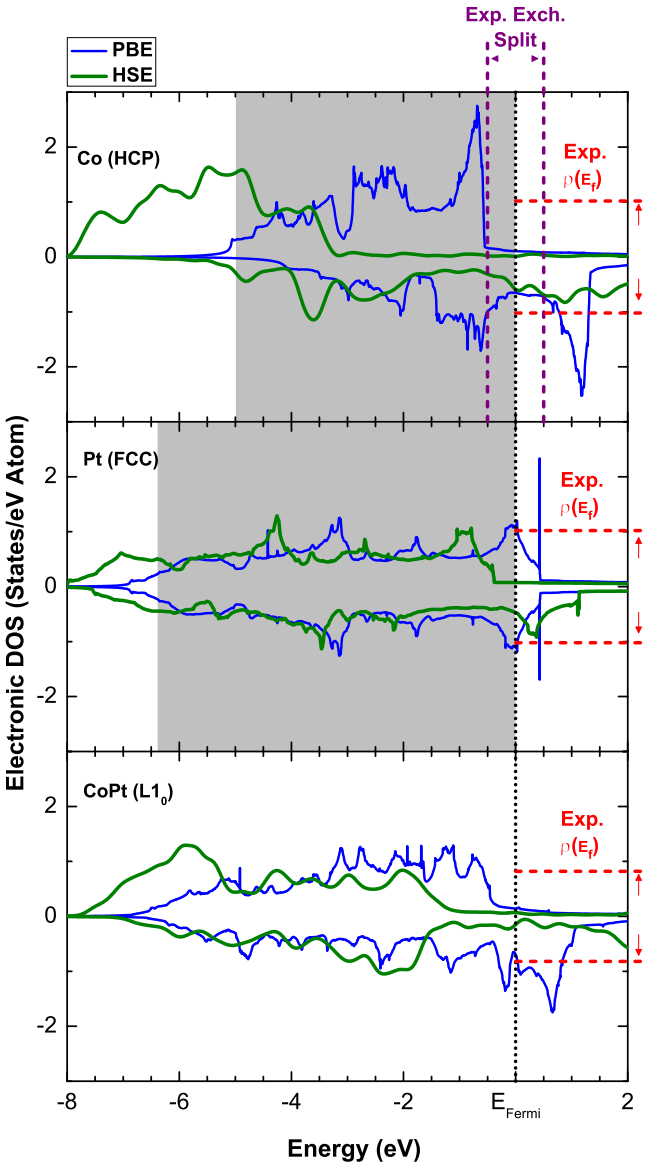

Figure 3.7: d-orbital density of states for HCP Co (top), FCC Pt (middle) and $L1_0$ CoPt (bottom) calculated from DFT, using both the PBE (blue line) and HSE06 (green line) functionals. Gray regions show occupied d-band width from photoemission results[194, 195], red dotted lines show occupation at the Fermi level predicted from the heat capacity[196–198], and purple dotted lines show exchange splitting predicted from experiment [ΔE between $N(E)_{\max}$ for majority and minority spins] for Co[199].

3.3.3 Additional Functionals

Additional functionals were explored, though not in-depth, once initial results indicated a qualitatively similar set and arrangement of ground states to the results using PBE. The Tao-Perdew-Staroverov-Scuseria[201] meta-GGA functional and its revised

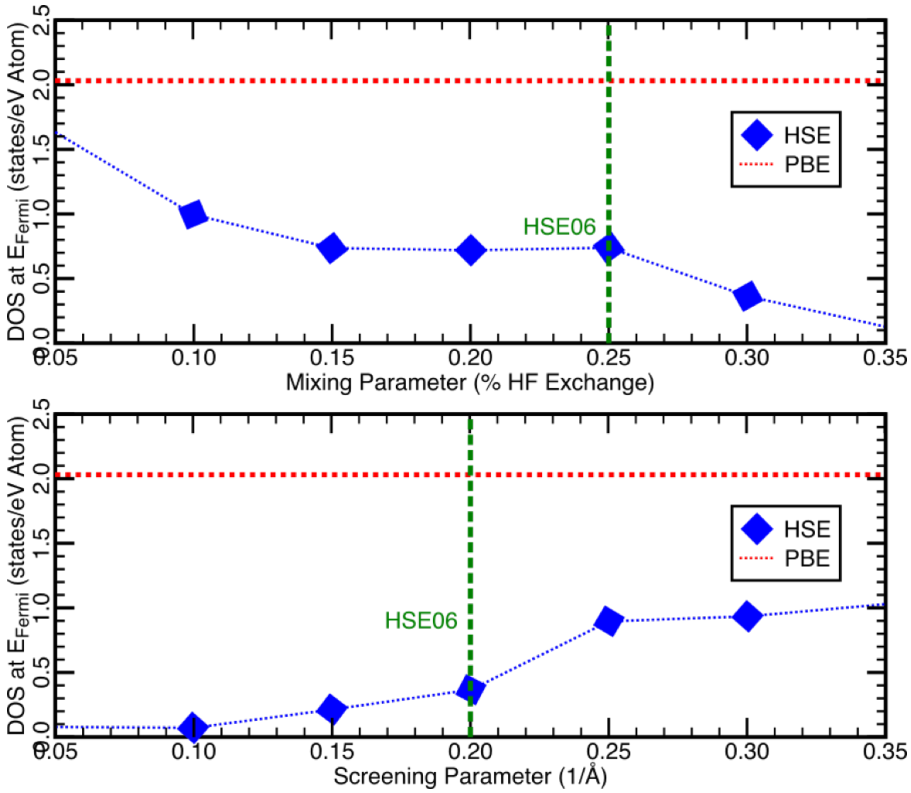

Figure 3.8: DOS at the Fermi energy for $L1_0$ CoPt with different values of the HSE mixing (top) and screening (bottom) parameters.

variant[105], as well as the Minnesota meta-GGA functional M06-L[202], were tested, but retained β_2-like structures and excluded $L1_2$ $CoPt_3$ from the set of ground states. PBESol[103] was investigated but also produced similar results to PBE. HSESol[203], and various parametrizations of the HSE functional (in α and ω) were tested only on $L1_0$ CoPt, $L1_2$ Co_3 Pt and $CoPt_3$, and β_2 $CoPt_2$, but yielded decreasingly tiny occupations at the Fermi level as well as worsening energetics and a deepening of the β_2 enthalpy with respect to other ground states.

The importance of localized d electrons in Co-Pt, which has been incorrectly treated in both PBE and HSE06, motivated the examination of the LSDA+U method[83]. We explored a two-dimensional grid of U's of 1.0–4.0 eV in Co, and 0.0–4.0 eV in Pt, in 0.1 eV steps using the rotationally-invariant method of Dudarev *et al.*[84]. Unfortunately

(though perhaps not unsurprisingly), the results showed no set of U's that simultaneously produced the correct set of ground states, matched the experimental enthalpies (within a range of $\pm 50\%$), and matched the experimental c/a ratio (within a range of $\pm 50\%$). The linear-response approach to determine coupling parameters of Cococcioni and Gironcoli[204] was also used, but the resulting U's produced similar unsatisfactory results.

3.4 Conclusion

In this Chapter, we have shown that the anomalous ground states predicted in Co-Pt using the PBE functional result in equally anomalous phase behavior at elevated temperature, wholly inconsistent with the body of experimental literature. By examining our results in the greater context of the *known* shortcomings of PBE, we can characterize the modes of failure, attributing the stabilization of the β_2 $CoPt_2$ ground state to SIE and occupation errors inherent in the functional. Although DFT performs exceptionally well in a wide variety of inorganic systems, caution must be used when predictions appear inconsistent with experiment. By using rigorous statistical mechanical approaches, experimental results can be meaningfully compared with zero kelvin predictions in both qualitative and quantitative fashions. Unfortunately, when one method falls short, it is not always sufficient to move up the "Jacob's ladder" of XC functionals[81]: the HSE06 functional merely trades one set of inaccuracies for another. Based on both our analysis and the existing literature, we believe that sibling systems (e.g., Fe-Pt, Ni-Pt, Fe-Ni) will yield similar results. Though the prospect of a one-size-fits-all DFT-based approach to predicting phase diagrams is appealing, our analysis of the Co-Pt system highlights the need to review zero kelvin electronic results in a finite-temperature and thermodynamically meaningful fashion.

Chapter 4

Recovering 0 Kelvin Effective Hamiltonian Parameters from High-Temperature Disordered Phases

> Thermodynamics is a funny subject. The first time you go through it, you don't understand it at all. The second time you go through it, you think you understand it, except for one or two small points. The third time you go through it, you know you don't understand it, but by that time you are so used to it, it doesn't bother you any more.
>
> *Arnold Sommerfeld*

In this Chapter, we present a new method to run the statistical mechanics problem "in reverse", using high-temperature observations and thermodynamic connections to construct an effective Hamiltonian and thereby predict the zero kelvin energy spectrum and associated ground states. Building upon the discussion in Section 2.2, we re-examine

the Cluster Expansion formalism through the lens of entropy-maximization approaches to develop an algorithm to select the relevant lattice basis functions and determine their corresponding interaction coefficients. This technique utilizes only a few, high-temperature experiments on disordered phases. We demonstrate that the approach can recover not only the ground states at zero kelvin, but also the full phase behavior for three realistic two-dimensional and three-dimensional alloy test-cases.

4.1 Introduction

First-principles electronic structure methods, such as density functional theory (DFT), can provide a unique view into atomic-scale properties that are otherwise *inaccessible* via experiment. Statistical mechanics, or other scale bridging techniques, can then connect the quantum mechanical energy spectrum to the realm of experimentally observable, and industrially-relevant, temperatures and length scales. Directly utilizing first-principles electronic structure methods in statistical mechanics schemes (e.g., to calculate the energy of every microstate), though, is in general computationally intractable. While *ab-initio* molecular dynamics[205] is increasingly being used to probe high temperature behavior[206, 207], it remains restricted to artificially small periodic unit cells and short simulation times[58, 208]. Instead, atomistic models[28–30, 135, 208–220] are more often used to represent a first-principles landscape as a function of relevant degrees-of-freedom (DOFs). The path from electronic structure to the laboratory, however, is almost entirely one-way: should an *ab-initio* method prove unreliable when compared to experiment, the experiments cannot be meaningfully used to inform and improve the electronic structure model with the same detail and precision as a direct, first-principles method.

This situation motivates the development of a technique that goes "in reverse", whereby measurements of an easily accessible, high-temperature, and disordered phase

are used to develop an atomistic model that is accurate at zero kelvin. The advantages of such an approach are many. An accurate atomistic model parameterized with high temperature data can be used to predict the energy spectrum over the microstates of a solid, as well as to reveal thermodynamic ground states that are otherwise difficult to determine experimentally (e.g., due to sluggish kinetics at low temperatures)[221]. Furthermore, the model can be applied in conventional Monte Carlo (MC) simulations to predict the full phase diagram[31, 34, 222, 223], or with variance constrained MC to predict free energies inaccessible to experiment (e.g., inside the spinodal of a miscibility gap)[224]. Even kinetic properties, such as diffusion[137, 165, 225] and precipitate nucleation and growth[226], can be elucidated with such a model.

Effective Hamiltonians[28–30, 117, 216, 227, 228], which have seen extensive use in the literature[31–34, 135, 143, 165, 171, 222, 223, 225, 229–235], provide a framework well-suited to developing such a model. They have proven to be powerful tools to extrapolate first-principles energy landscapes and come in many forms. A harmonic Hamiltonian expressed in terms of inter-atomic force-constants, for example, extrapolates first-principles force-displacement relations to predict phonon properties and vibrational free energies. Cluster Expansions[28–30] (CEs) and anharmonic lattice dynamics Hamiltonians[135, 211, 211, 212, 218, 219] have enabled the first-principles study of alloy phase diagrams and structural phase transitions with MC[34, 137, 211, 213, 218, 235, 236]. In their most rigorous form, an effective Hamiltonian can be formulated as a linear expansion in a set of basis functions, expressed in terms of variables that describe particular atomic DOFs. Alloy Hamiltonians, for example, commonly referred to as "Cluster Expansions", are expressed in terms of polynomials of occupation variables associated with clusters of sites (e.g., pairs, triplets etc.) in the crystal[28–30]. The resulting polynomial is computationally inexpensive, and thus well-suited for stochastic methods such as MC, which require tens of thousands of energy evaluations to calculate accurate thermody-

namic properties.

In this Chapter we explore the possibility of developing an "experiments-first" effective Hamiltonian, using high temperature experiments to predict zero kelvin behavior. We present a new method of parametrizing the Hamiltonian using experimental data of the disordered state instead of zero kelvin quantum mechanical predictions. The approach not only yields a parameterization of the expansion coefficients, but also suggests the most probable truncation of the Hamiltonian. Overall, the method enables the construction of an accurate atomistic model of crystalline materials suitable for a wide variety of stochastic simulation techniques. Our approach provides a new tool to develop full phase diagrams and probe otherwise difficult-to-measure thermodynamic properties, using only a small number of high-temperature observations of a disordered phase.

4.2 A Thermodynamic Approach to Cluster Expansion Parameters

We illustrate our approach of parameterizing an effective Hamiltonian with high temperature experimental data in the context of a binary A-B crystalline alloy. The approach is, nevertheless, general, and can be applied to any effective Hamiltonian constructed as a linear expansion of basis functions that depend on one or more atomic DOFs (e.g., local magnetic moments like used in Chapter 6, atomic displacements etc.). The analysis here builds off of the foundation laid in Section 2.2, which the reader is encouraged to review, in addition to References [28], [237], and [30].

4.2.1 Thermodynamic Relationships

Experiments are unable to provide direct access to the energies of individual microstates $\overline{\sigma}$. Methods for measuring internal energies or enthalpies return only the average over many microstates. Hence, a method based on an inversion of

$$E(\overline{\sigma}) = \sum_{\alpha} \Phi_{\alpha}(\overline{\sigma}) V_{\alpha}, \tag{4.1}$$

relying on experimental measurements, is unlikely to be found. By instead assigning a thermodynamic interpretation to the effective cluster interactions (ECIs, $\overline{V}$) of a CE, other expressions can be derived that relate averages of spatial correlations over clusters of sites, which can be measured with a variety of local or reciprocal probes, to the $\overline{V}$.

It is convenient to work in the canonical ensemble (constant temperature T, number of sites N, and number of A sites $N_A \leq N$), which has as partition function Z and free energy A:

$$Z(T, N, N_A) = \sum_{\overline{\sigma}} e^{-\frac{\overline{\Phi}(\overline{\sigma}) \cdot \overline{V}}{k_b T}} \tag{4.2}$$

$$A(T, N, N_A) = -k_b T \ln [Z] \tag{4.3}$$

The sum is restricted to configurations $\overline{\sigma}$ having fixed composition, and k_b is the Boltzmann constant. Starting with the canonical free energy, we can produce a number of derivatives, some of which have been discussed in previous work[238]. We highlight a few that are of practical importance here:

$$\frac{\partial A}{\partial V_\alpha} = \langle \Phi_\alpha \rangle \tag{4.4}$$

$$\frac{\partial^2 A}{\partial V_\alpha \partial V_\beta} = \frac{\partial \langle \Phi_\alpha \rangle}{\partial V_\beta} = \frac{\partial \langle \Phi_\beta \rangle}{\partial V_\alpha} = -\frac{\text{cov}[\Phi_\alpha, \Phi_\beta]}{k_b T} \tag{4.5}$$

$$\frac{\partial^2 A}{\partial V_\alpha \partial T} = \frac{\partial \langle \Phi_\alpha \rangle}{\partial T} = -\frac{\partial S}{\partial V_\alpha} = \frac{\text{cov}[\Phi_\alpha, (\overline{V} \cdot \overline{\Phi})]}{k_b T^2} \tag{4.6}$$

where $\langle y \rangle = \sum_{\overline{\sigma}} y \frac{\exp\left[\frac{-\overline{V} \cdot \overline{\Phi}(\overline{\sigma})}{k_b T}\right]}{Z}$ denotes the ensemble average of y and $\text{cov}[y, z] = \langle yz \rangle - \langle y \rangle \langle z \rangle$ denotes the ensemble covariance of y and z. S in Equation (4.6) refers to the entropy.

Equations (4.5) and (4.6) are response functions, measuring how the ensemble average of an extensive cluster function, $\langle \Phi_\alpha \rangle$, responds to a change in either an ECI, V_β, or the temperature. Equation (4.6) is especially useful after expanding the covariance of the products and rearranging slightly:

$$k_b T^2 \frac{\partial \langle \overline{\Phi} \rangle}{\partial T} = \mathbf{cov}[\overline{\Phi}, \overline{\Phi}] \cdot \overline{V} \tag{4.7}$$

with $\mathbf{cov}[\overline{\Phi}, \overline{\Phi}]$ denoting a matrix, with each element of this matrix, $\left(\mathbf{cov}[\overline{\Phi}, \overline{\Phi}]\right)_{\alpha,\beta}$, corresponding to an ensemble averaged covariance between a pair of extensive cluster functions, Φ_α and Φ_β. The left hand side of Equation (4.7) is a column vector of the temperature derivatives of the ensemble averages of the extensive cluster functions Φ_α, multiplied by $k_b T^2$.

Equation (4.7) is a crucial component of the approach as it provides a connection between a *measurable* set of variables, $\mathbf{cov}[\overline{\Phi}, \overline{\Phi}]$ and $k_b T^2 \frac{\partial \langle \overline{\Phi} \rangle}{\partial T}$, and a desirable (but immeasurable) set of coefficients, $\overline{V}$. Once values have been measured for the temperature dependence of the extensive cluster functions, and for covariances between pairs of extensive cluster functions, it should in principle be possible to invert Equation (4.7) to

recover the expansion coefficients $\overline{V}$. These expansion coefficients can then be used in standard statistical mechanics approaches to determine ground states and to calculate the *full* phase diagram. Hence, with only a few measurements, information about the entire phase space can be generated.

4.2.2 Entropy-Maximizing Basis Function Selection

While Equation (4.7) offers the potential to extract the ECI of a CE from experimental measurements of extensive cluster functions, Φ_α, and their covariances, a direct inversion is, in general, infeasible. Experience with first-principles parameterized CE shows that these Hamiltonians are typically sparse, converging rapidly as the cluster size of a basis function increases, both in spatial extent and number of sites. Even when the clusters are small, their corresponding ECI may be close to zero. Before Equation (4.7) can be inverted, it is therefore necessary to devise a method to determine the "correct" sparse set of clusters (i.e., non zero elements in $\overline{V}$). Biased regression schemes (such as l^1-norm penalization[239]), while attractive for DFT-based CEs[126–128], perform poorly when elements in the design matrix (i.e., $\mathbf{cov}[\overline{\Phi}, \overline{\Phi}]$) are correlated[240]. As the columns in our covariance matrix are themselves correlated, we require an external cluster-selection step that is robust to this feature.

To this end, we again rely on a thermodynamic interpretation of the expansion coefficients $\overline{V}$. The entropy-maximization approach of Jaynes[68] (MAXENT) can be employed to develop a simple metric to judge whether a given cluster should be included or excluded in a final regression scheme to extract the non-zero $\overline{V}$ from Equation (4.7). Treating the ECI as thermodynamic variables, we can re-cast the problem in the form of finding a set of parameters, $\overline{V}$, which satisfy:

$$\frac{\partial A}{\partial \overline{V}} = \langle \overline{\Phi} \rangle_{\text{obs}}, \tag{4.8}$$

where $\langle \overline{\Phi} \rangle_{\text{obs}}$ is an *observed* value of the extensive cluster functions. This relation yields a microstate distribution that maximizes the "information entropy" of the system, given the constraint that $\langle \overline{\Phi} \rangle$, the ensemble average, is equal to $\langle \overline{\Phi} \rangle_{\text{obs}}$. The Lagrange multipliers in this constrained maximization problem are, conveniently, the ECIs. Our entropy-maximizing solution is then given by the *stationary points* with respect to $\overline{V}$ of the free energy Υ:

$$\Upsilon(T, N, N_A, \overline{V}, \langle \overline{\Phi} \rangle_{\text{obs}}) = A(T, N, N_A) - \overline{V} \cdot \langle \overline{\Phi} \rangle_{\text{obs}}. \tag{4.9}$$

Finding the stationary points is as simple as solving $\frac{\partial \Upsilon}{\partial \overline{V}} = 0$ (which returns Equation (4.8)). When the $\langle \overline{\Phi} \rangle_{\text{obs}}$ are measured in a thermodynamically stable phase, these stationary points are *maxima*, as proven by the sign of the Hessian of A (and, therefore, of Υ) in $\overline{V}$:

$$\frac{\partial^2 \Upsilon}{\partial \overline{V}^2} = -\frac{\mathbf{cov}\left[\overline{\Phi}, \overline{\Phi}\right]}{k_b T} \leq 0. \tag{4.10}$$

The strict seminegative-definite nature of the Hessian of Υ for thermodynamically stable phases guarantees a single maximum only. This means that any changes in $\overline{V}$ that increase Υ are moving us towards that global maximum — there are no local maxima upon which to become trapped. Therefore, if we can evaluate how Υ changes when a cluster is included or excluded, we can use the sign of $\Delta\Upsilon$ to determine if that cluster is moving us towards or away from the MAXENT solution.

A difficulty with Equation (4.9) is that we do not know the free energy A of the phase in which the $\langle \overline{\Phi} \rangle_{\text{obs}}$ were measured. However, for a disordered solid solution, we

can approximate it by performing a Taylor expansion of $A(\overline{V})$ around the non-interacting crystal ($\overline{V} = 0$) corresponding to an ideal solution. To first order:

$$\Upsilon(T, N, N_A, \overline{V}, \langle\overline{\Phi}\rangle_{\text{obs}}) \approx A_0 + \overline{V} \cdot \left(\langle\overline{\Phi}\rangle_0 - \langle\overline{\Phi}\rangle_{\text{obs}}\right) \tag{4.11}$$

where A_0 is the ideal solution free energy, and $\frac{\partial A}{\partial \overline{V}}\big|_{\overline{V}=0} = \langle\overline{\Phi}\rangle_0$ is the vector of ideal-solution extensive cluster functions, which can easily be evaluated, as the sites of any cluster in an ideal solution are uncorrelated by definition. With the Taylor expansion approximation to Υ, the criterion $\Delta_\alpha\Upsilon$ as to whether or not a cluster α should be included is then:

$$\Delta_\alpha\Upsilon\left(T, N, N_A, \langle\overline{\Phi}\rangle_{\text{obs}}\right) \approx \left(\langle\overline{\Phi}\rangle_0 - \langle\overline{\Phi}\rangle_{\text{obs}}\right) \cdot \left[\overline{V}_{\text{new}}\left(\langle\overline{\Phi}\rangle_{\text{obs}}\right) - \overline{V}_{\text{old}}\left(\langle\overline{\Phi}\rangle_{\text{obs}}\right)\right] \tag{4.12}$$

where $\overline{V}_{\text{new}}\left(\overline{\Phi}_{\text{obs}}\right)$ and $\overline{V}_{\text{old}}\left(\overline{\Phi}_{\text{obs}}\right)$ refer to the values of the ECIs calculated using Equation (4.7) with cluster α included and excluded, respectively. By testing each candidate cluster α for $\Delta_\alpha\Upsilon > 0$, we can differentiate between relevant clusters with small ECIs, and clusters with 0 ECIs that recover nonzero values due to regression error. This algorithm is described in the following section, and requires only a single pass through the set of all clusters. For reasons of numerical stability, only cluster observations on the same length-scale of any "selected" clusters are used for subsequent evaluations of Equation (4.7).

The uniqueness of the maximum of Υ is only guaranteed where the free energy varies smoothly, i.e., far from a phase boundary. Additionally, as our Taylor expansion is based around the ideal solution, observations should only be drawn from the disordered phase. This is an easy region to access experimentally, and agrees well with the goals outlined

at the beginning of this section. Using Equation (4.12), we can determine the ideal set of clusters to include, and with Equation (4.7), we can solve for their ECIs. These clusters and ECIs are sparse, thermodynamically-consistent, share a one-to-one mapping with the observed extensive cluster functions, and can be found using only a few observations of the high-temperature, disordered phase.

4.3 Selection Algorithm

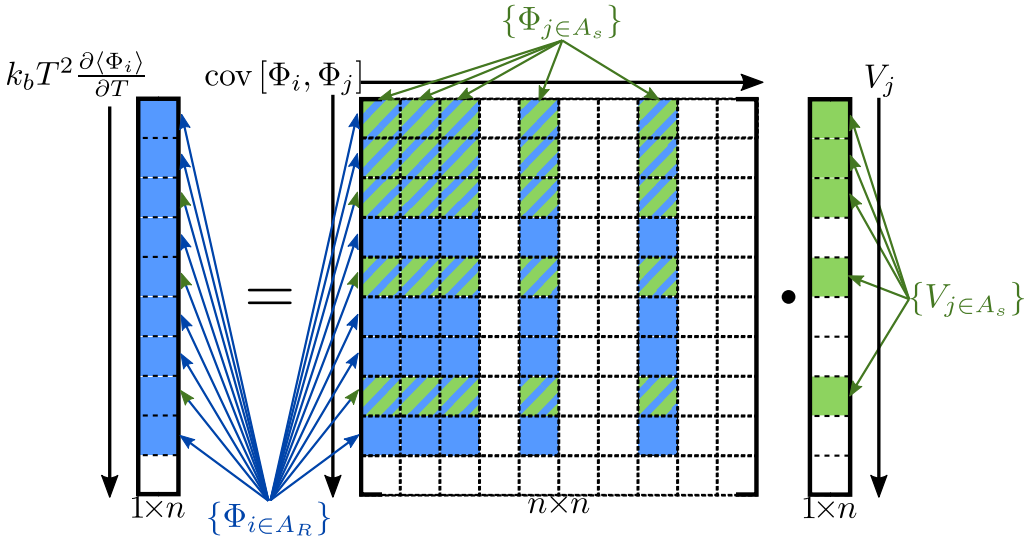

Figure 4.1: Schematic version of the regression scheme, Equation (4.7), indicating which columns are selected by Equation (4.12) (the set A_s, in green) and which rows are included by the cluster radius cutoff (the set A_R, in blue). Selecting only rows that represent extensive cluster functions in A_s results in large quantities of data going unused. By using A_R, i.e., the set of geometric clusters at or below the cluster radius of the largest geometric cluster in A_s, a significantly larger portion of the available observations can be used.

The approach of our algorithm is to invert Equation (4.7) via regression, using Equation (4.12) to select which ECIs will be allowed to be nonzero. Additionally, we wish to restrict the range of measurements, i.e., $k_bT\frac{\partial\langle\Phi_i\rangle}{\partial T}$, utilized in our regression. Figure 4.1 schematically illustrated the set-up of the regression, indicating which ECIs

have been selected (in green) and which measurements are being utilized (in blue). Let some selected set of ECIs be indexed by $A_s = \{\alpha_0, \alpha_1, \dots\}$, such that our model coefficients are $\overline{V}_{A_s} = \{V_{i \in A_s}\}$. Then, let some utilized set of measurements be indexed by $A_R = \{\beta_0, \beta_1, \dots\}$, such that our predicted outputs are $\overline{y}_{A_R} = \{k_b \frac{\partial \langle \Phi_{j \in A_R} \rangle}{\partial T}\}$. Then, the columns utilized in our design matrix, $\boldsymbol{X}$, must be A_s and the rows utilized must be A_R, such that $\boldsymbol{X} = \mathbf{cov}[\{\Phi_{j \in A_R}\}, \{\Phi_{i \in A_s}\}]$. These definitions will be utilized extensively in the description of our algorithm, below. Our selection-and-regression algorithm runs in polynomial time, and requires no additional data or information beyond the same information needed for Equation (4.7). The algorithm as implemented in section III is outlined below:

1. Form the set of extensive cluster function indices A for which there exists data, up to a cut-off radius r, sorted by increasing geometric cluster[1] size (first by cluster radius, then by the number of sites in the cluster):

$$A = \{\alpha_0, \alpha_1, \dots, \alpha_n\}.$$

2. Initialize the list of selected ECIs A_s by selecting the indices associated with the empty, point and pair clusters from A:

$$A_s = \{\alpha_0, \alpha_1, \alpha_2\}.$$

3. Let the cluster radius $r(\alpha_i)$ be the longest distance between any two sites in α_i, and define R_s be the largest cluster radius of geometric clusters represented in A_s:

[1] A *geometric cluster* refers to the set of sites on a lattice included in the definition of a cluster function, but *not* which basis function of the site is being used

$$R_s = \max\left[\{r(\alpha_i) : \forall \alpha_i \in A_s\}\right]$$

4. Form the set of indices affiliated with geometric clusters as small as, or smaller than, R_s. This set defines the extensive cluster functions with measurements that we presume to be dominated by signal, rather than noise:

$$A_R = \{\alpha_i : \forall \alpha_i \in A \text{ if } r(\alpha_i) \leq R_s\}$$

5. Using ridge regression [2] (with regularization parameter γ), calculate the ECIs for A_s:

$$\overline{V}_{A_s} = (\boldsymbol{X}\boldsymbol{X}^\intercal + \gamma \boldsymbol{I})^{-1}\boldsymbol{X} \cdot \overline{y}_{A_R}$$

6. From A, select the next index α_j which has not yet been examined, and form the set A_j:

$$A_j = A_s + \{\alpha_j\}\,.$$

7. Using ridge regression[3] (with regularization parameter γ), calculate the ECIs for A_j:

$$\overline{V}_{A_j} = k_b T^2 (\boldsymbol{X}\boldsymbol{X}^\intercal + \gamma \boldsymbol{I})^{-1}\boldsymbol{X} \cdot \overline{y}_{A_R}$$

[2] Ridge regression is only used in the *selection* step, not in the for the final ECIs when A_s has been fully determined; the motivation for this choice is described in Section 4.5.3

[3] During the application of our algorithm, any $\Delta\Upsilon_j$ or ECI values ≤ 0.001 meV in magnitude were considered to be 0

8. Use Equation (4.12) to calculate $\Delta\Upsilon$:

$$\Delta_j\Upsilon(T, N, N_A, \overline{\Phi}_{\text{obs}}) = \sum_{\alpha\in A_s} \left(\overline{\Phi}_0^\alpha - \overline{\Phi}_{\text{obs}}^\alpha\right)\left(V_{A_j}^\alpha - V_{A_s}^\alpha\right)$$

9. If $\Delta_j\Upsilon > 0$, $A_s = A_j$, otherwise A_s remains unchanged.

10. Return to step 3, until there exist no indices in A which have not been examined.

11. Using the final set of selected A_s determine the ECIs. Calculate R_s and construct A_R as in steps 3 and 4, respectively, and build $\boldsymbol{X} = \mathbf{cov}\left[\{\Phi_{j\in A_R}\}, \{\Phi_{i\in A_s}\}\right]$. Solve for $\overline{V}_{A_s}$ using ordinary least squares regression:

$$\overline{V}_{A_s} = k_b T^2 (\boldsymbol{X}\boldsymbol{X}^\intercal)^{-1}\boldsymbol{X}\cdot\overline{y}_{A_R}$$

4.4 Testing the Hamiltonian inversion approach on simulated data

We used simulated data sets to test the viability of the methodology developed in Section II to parameterize an effective Hamiltonian to high temperature measurements. Benchmarking of the approach was performed on three binary systems (A-B alloys) with their configurational energy described by CE Hamiltonians. This included two systems on a 2D triangular lattice using: (I) only nearest and next-nearest neighbor (NN and NNN) interactions, and (II) six pseudo-random interactions, including three and four-body clusters. System I has been characterized in-depth by Glosli and Plischke[241]. We also studied a 3D FCC lattice (III) using clusters and ECIs generated from first-principles to model the Au-Cu system by Z. Lu, *et al*[242]. For all systems, we report our results

using the following dimensionless, reduced units:

$$\tau = \frac{k_b T}{V_{NN}} \qquad m = \frac{\mu_A - \mu_B}{V_{NN}} \qquad x_A = \frac{N_A}{N}$$
$$v_i = \frac{V_i}{V_{NN}} \qquad e = \frac{E}{V_{NN}}$$

where V_{NN} is the nearest-neighbor-pair ECI from the *original* CE, and E and e refer to *any* type of energy, in the absolute and dimensionless units, respectively. An ECI that is strictly zero, i.e., $v_\alpha = 0$, is equivalent to cluster function ϕ_α being excluded from the CE.

The normalized chemical potential difference m is related to the slope of the alloy free energy as a function of alloy composition x_A. The reference states for the model CEs were defined such that the energies for pure A and pure B are both equal to zero. With these reference states, very negative values of m correspond to B-rich alloys while very positive values of m correspond to A rich alloys. Equi-composition alloys have intermediate values of m that are centered around zero.

The simulated data was generated with semi-grand canonical MC simulations performed using the three model CEs, using the CASM code[31, 135–137]. While the methodology developed in Section II relies upon derivatives taken at constant composition, x_A, rather than at constant chemical potential, m, switching from the canonical to the semi-grand canonical ensemble requires only minor modifications to the equations and changes none of the analysis [4]. The MC simulations were used to calculate ensemble averages of the extensive cluster functions, $\langle \Phi_\alpha \rangle$, and their covariances, $\mathbf{cov}[\overline{\Phi}, \overline{\Phi}]$, in the disordered solid solution of the model alloys at high temperature. These two quantities

[4]Specifically, the number of configurations C is now $C = 2^N$, and the point-term ECI changes from V_1 to $V_1' = V_1 + \frac{\mu}{2}$. This transformation is achieved by examining the argument to the exponential in the semigrand canonical ensemble: $\frac{-\overline{V}\cdot\overline{\Phi}(\overline{\sigma})+\mu N_A}{k_b T}$, and noting that, for our choice of basis set, $N_A = \frac{\Phi_1(\overline{\sigma})+N}{2}$. We can then collect $\Phi_1(\overline{\sigma})(V_1 + \frac{\mu}{2}) = \Phi_1(\overline{\sigma})V'$ and bring the remaining $\frac{\mu N}{2}$ out of the exponential, and indeed out of any outer sum over microstates, entirely as the number of sites N is unchanging.

represent the "experimental data" needed to invert Equation (4.7) to determine the ECIs. A 30×30 periodic supercell of the 2D triangular lattice was used to simulate data for systems I and II, while a $14 \times 14 \times 14$ periodic supercell of the FCC primitive cell was used to generate data for system (III). All measurements were taken from cooling runs at constant dimensionless chemical potential m. The number of passes (N_{pass}), starting dimensionless temperature (τ_0), incremental dimensionless temperature ($\Delta\tau$), and incremental dimensionless chemical potential (Δm) are given in Table (4.1):

For all three model alloys, we found a strong dependence of the recovered ECI on the value of m used to generate the simulated experimental data sets. Data sets collected at chemical potentials that stabilize B-rich alloys or A-rich alloys (i.e., very negative or very positive values of m) were less robust, as changes in $\langle\overline{\Phi}\rangle$ became small at near-pure compositions. However, in the chemical potential range that stabilizes a more equi-compositional alloy, a more consistent and reliable set of ECIs could be recovered (provided the values of m and τ were not too close to a phase transition). To compare the robustness of simulations performed at different values of m, we employed the following "consistency score" figure-of-merit:

$$S_m = \frac{2}{\|\overline{v}_m - \overline{v}_{m+\Delta m}\| + \|\overline{v}_m - \overline{v}_{m-\Delta m}\|}, \tag{4.13}$$

where $\overline{v}_m$ is the vector of (reduced) ECIs evaluated for a simulation performed at chemical potential m, and Δm is the chemical potential step size used when performing multiple simulations. S_m corresponds to the (reciprocal of the) average Euclidean norm of ECIs evaluated at three chemical potentials m and $m \pm \Delta m$. This consistency score is used to evaluate when the inversion algorithm ceases to provide reliable results, due to divergences or zeros in $\mathbf{cov}\left[\overline{\Phi}, \overline{\Phi}\right]$ at phase boundaries or compositional extremes. The reciprocal form provides easier interpretation of the results, and maps the "steadiest"

solutions into the largest scores.

In the following three sections, we summarize the thermodynamic phase behavior of each model system and describe how the inverted CEs compare to the original CEs used to generate the high temperature data sets. For each alloy system, we determined the final $\overline{v}$ with the following process. High temperature measurements (averages of the extensive cluster functions, $\langle \Phi_\alpha \rangle$, and their covariances, $\mathbf{cov}[\overline{\Phi}, \overline{\Phi}]$) were calculated for a range of m values. The temperature range was chosen to be both narrow and near (but not at) the highest-temperature phase transition. For each value of m, a sparse vector, $\overline{v}_m$ was determined using the algorithm of Section 4.3, based on Equation (4.12)[5]. Next, runs were filtered to only include the range of m values centered on $m = 0$ for which S_m remained sufficiently large. Using this *reduced* range, only clusters with ECI (entry in $\overline{v}_m$) that were nonzero more than 50% of the time were kept, forming the "selected" set. Finally, ECIs were calculated for the selected set of clusters at each m in the reduced range, with each m being treated independently. By averaging $\overline{v}_m$ of the selected set of clusters over the reduced range of m, a final sparse set of ECIs was determined.

Table 4.1: Simulation conditions for semi-grand canonical MC simulations.

Simulation	N_{pass}	τ_0	$\Delta\tau$	Δm
I (2D)	10,000	1.29	-2.59×10^{-3}	0.15
II (2D)	5,000	6.46	-12.9×10^{-3}	0.3
III (3D)	5,000	3.18	-3.18×10^{-3}	0.369

4.4.1 System I: NN and NNN 2D Triangular Lattice

The original and recovered clusters and ECIs for the 2D triangular lattice are given in Table 4.2, with diagrams of the clusters shown in Figure 4.2a. The zero kelvin formation

[5]During the application of our algorithm, any $\Delta\Upsilon_j$ or ECI values ≤ 0.001 meV in magnitude were considered to be 0

energies of several structures, including the five ground states for this CE, are shown in Figure 4.2b, with the ordering of each ground state illustrated in Figure 4.2c. This set of clusters and ECIs produces a symmetric phase diagram with both first-order and continuous phase transitions as is evident in Figure 4.3a. Data for use in our algorithm was sampled over a wide range of chemical potentials and at temperatures from the region in Figure 4.3a bounded by blue, dashed lines.

Table 4.2: Cluster Characteristics for the 2-Cluster 2D Triangular Lattice.

Cluster i	Original v_i	Recovered v_i
2	1.0	0.969
3	0.1	0.0966
12	0.0	1.26×10^{-3}

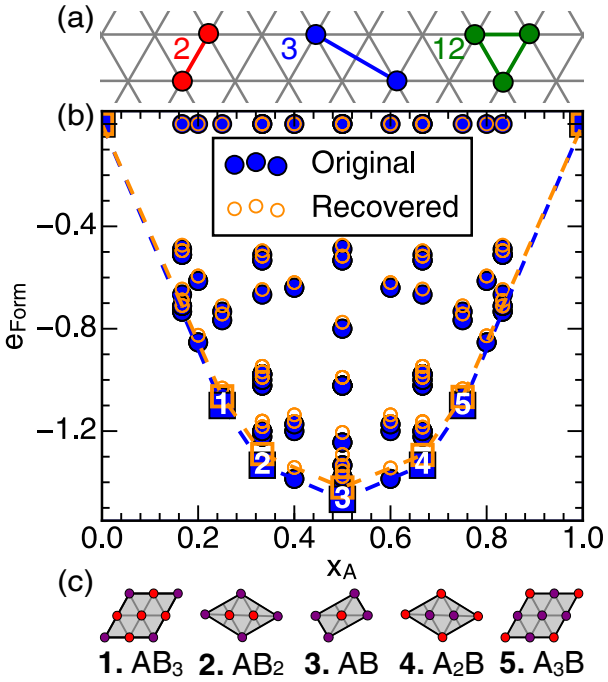

Figure 4.2: (a) shows the two initial cluster prototypes used in our 2D triangular lattice (2 and 3), in addition to a third recovered cluster prototype (12). (b) shows the composition vs formation energy of a selection of configurations, in supercells containing up to 6 sites. Squares indicate ground states and are numbered to match (c). (c) shows schematic cells of the five ordered ground states. Red circles represent particle A, $\sigma_i = +1$, and purple circles represent particle B, $\sigma_i = -1$.

The algorithm of Section 4.3 was applied to data generated over a range of chemical potentials, m, yielding a sparse set of ECIs at each m. The region where the algorithm performs consistently was determined by the location of the first significant increase

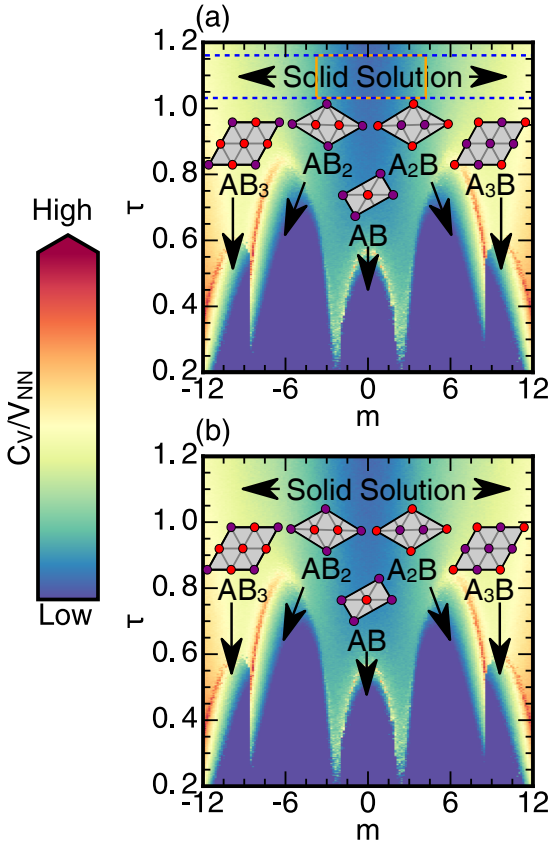

Figure 4.3: Plots (a) and (b) show logrithmic heatmaps of the heat capacity C_V (scaled by V_{NN}), using the original and recovered ECIs, respectively. The approximate phase boundaries visible as sharp shifts in color, and appear at nearly identical locations in both phase maps. The blue dashed lines indicate the range of temperatures across which observations were taken, while the orange lines match those in Figure 4.4a.

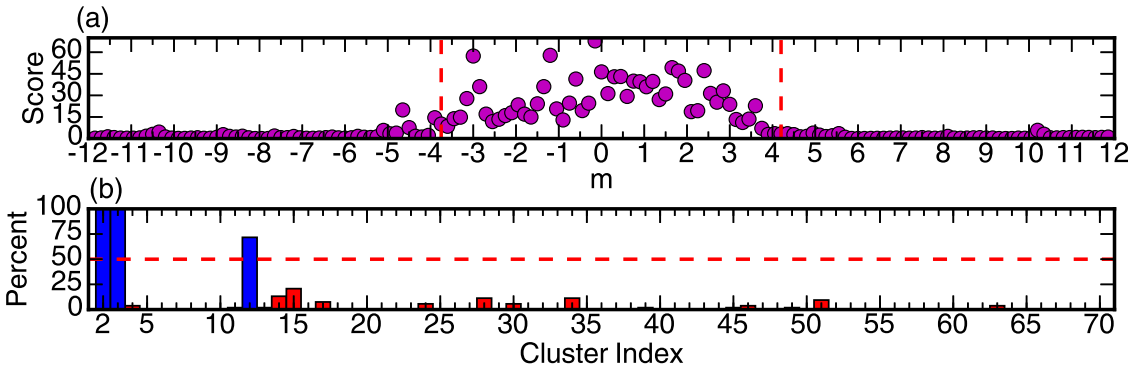

Figure 4.4: (a) shows the consistency score (Equation 4.13) calculated at each chemical potential (purple dots) using the recovered clusters and ECIs found via our algorithm. Only data between the dashed orange lines was used for subsequent analysis. (b) shows the fraction of runs each cluster appeared in; only clusters above the cutoff ($\geq 50\%$, dashed red line) were utilized in the final regression step to determine ECIs.

in the consistency score, S_m, (Equation (4.13)) surrounding $m = 0$, as can be seen in Figure 4.4a. The region of data then used to determine the final clusters and their ECIs is indicated by the orange (dashed) lines in Figures 4.4a and 4.3a, referred to as the "reliable zone". The final ECIs were determined following two steps: first, the percentage of m values in the reliable zone in which each cluster was included in the CE was tallied. This percentage is presented in Figure 4.4b. Any clusters which appeared in half or more of the runs in the reliable zone were included in the final set of clusters. This final set of clusters was then used in a global regression over data collected at all chemical potential values m in the reliable zone. The final set of ECI are listed in Table 4.2.

In addition to the nearest and next-nearest neighbor clusters (2 and 3, respectively), the algorithm also picked up the nearest-neighbor triplet (cluster 12). The recovered ECIs of clusters 2 and 3 are both within 5% of their original values, in addition to maintaining the 10:1 ratio present in the original CE. The nearest-neighbor triplet has a value nearly two orders-of-magnitude smaller than that of the next-nearest neighbor ECI; its impact on any calculated energies is therefore negligible. This assertion is proved by both the zero kelvin formation energies reproduced using the recovered ECIs in Figure 4.2b, and the shape and features of the phase diagram in Figure 4.3b. For this simple model CE, the algorithm of Section 4.3 has successfully recovered not only the correct ground states, but the correct phase behavior throughout all of phase space, while utilizing only a tiny fraction of the data available.

4.4.2 System II: 6-Cluster 2D Triangular Lattice

To examine a more complex CE for the triangular lattice, six clusters were chosen to represent a spread of cluster lengths and cluster sizes. The values of the ECIs were chosen randomly and are listed in Table 4.3. Their corresponding clusters are shown in

Figure 4.5a. Zero kelvin formation energies for a selection of orderings on the triangular lattice, including the five ground states, are shown in Figure 4.5b, with orderings for each ground state illustrated in Figure 4.5c. The phase diagram for this CE is shown in Figure 4.6a and is asymmetric, exhibiting both first-order and continuous phase transitions. As before, only data at temperatures bounded by the two blue, dashed lines in Figure 4.6a was used in the algorithm of Section 4.3 to recover the ECI.

Table 4.3: Cluster Characteristics for the 6-Cluster 2D Triangular Lattice.

Cluster i	Original v_i	Recovered v_i
2	1	0.946
3	0.3	0.266
6	0.5	0.433
12	0.3	0.286
14	0	−0.0109
15	0.5	0.450
47	0.3	0.287

Similar to system I described in Section IIIA, we calculated a consistency score for each chemical potential, and used an increase in the consistency score to bound the "reliable zone". The scores and resulting boundaries are shown in Figure 4.7a. The cluster frequencies in this region are plotted in Figure 4.7b, with clusters selected more than 50% of the time utilized in the final series of regressions. In addition to the original clusters, the next-nearest-neighbor triplet (cluster 14) was picked up, with an ECI one order-of-magnitude smaller then the next-smallest ECI. All of the remaining ECIs recovered were within 15% of their original values, and 10% of their relative relationships to the nearest-neighbor ECI.

The recovered CE correctly reproduces the same ground states and formation energies (with a vertical offset) of the original CE, as shown in Figure 4.5b. The calculated phase diagram of Figure 4.6b shows that the transition temperatures and the nature of the

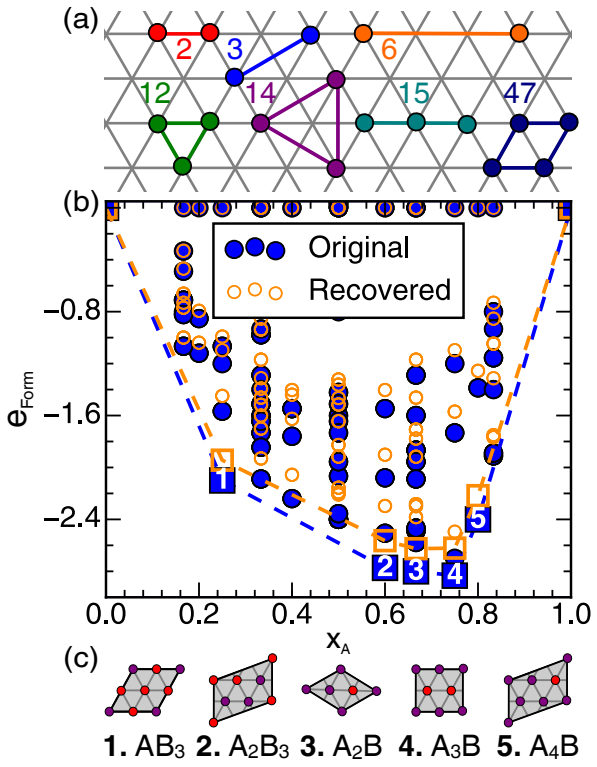

Figure 4.5: (a) shows the six initial cluster prototypes (2, 3, 6, 12, 15, 47) used to generate data, as well as a spuriously-recovered cluster prototype (14). (b) shows the composition versus formation energy for all configurations in supercells containing up to 6 sites. Squares indicate ground states and are numbered to match (c). (c) shows schematic cells of the five ordered ground states. Red circles represent particle A, $\sigma_i = +1$, and purple circles represent particle B, $\sigma_i = -1$.

transition (i.e., first-order versus continuous) are also faithfully reproduced across all of phase space. These results demonstrate the ability of the algorithm to recover a CE from high temperature data that correctly predicts phase stability over all of phase space.

4.4.3 System III: 3D FCC Lattice

The algorithm of Section 4.3 was also tested on a CE constructed by Z. Lu, *et al.* [242] to describe the Au-Cu binary alloy. The ECIs are given in Table 4.4 and the clusters are illustrated in Figure 4.8a. The zero kelvin formation energies of the $L1_0$ and $L1_2$ ground states, as well as of a number of other configurations, are shown in Figure 4.8b with orderings of the ground states illustrated in Figure 4.8c. Figure 4.9a shows the phase diagram, exhibiting expected behavior akin to that experimentally observed for Au-Cu. As for model systems I and II, only data from temperatures between the two blue, dashed lines in Figure 4.9a was used to recover a CE.

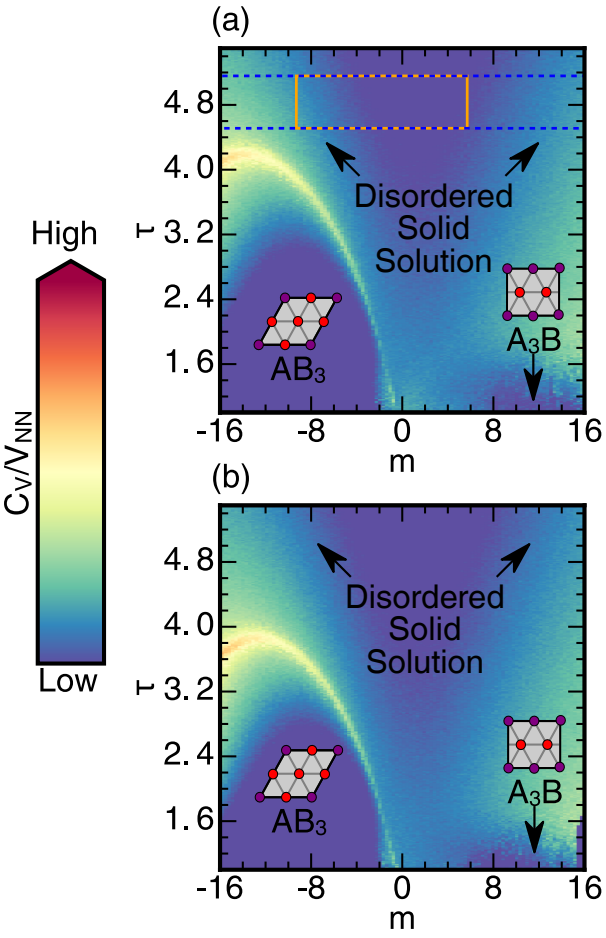

Figure 4.6: Plots (a) and (b) show logrithmic heatmaps of the heat capacity C_V (scaled by V_{NN}), using the original and recovered ECIs, respectively. The approximate phase boundaries are visible as sharp shifts in color, and appear at nearly identical locations in both phase maps, save for a slight amount of scaling. The blue dashed lines indicate the range of temperatures across which observations were taken, while the orange lines match those in Figure 4.7a.

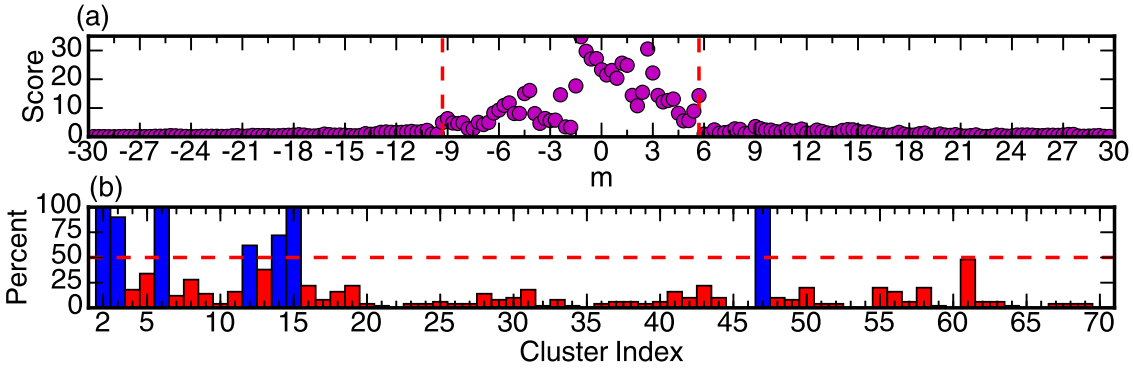

Figure 4.7: (a) shows the score (Equation (4.13)) calculated at each chemical potential (purple dots) using the recovered clusters and ECIs found via our algorithm. Only data from between the dashed orange lines was used for subsequent analysis. (b) shows the fraction fo runs each cluster appeared in; only clusters above the cutoff ($\geq 50\%$, red dashed line) were used in the final regression to determine the ECIs.

Table 4.4: Cluster Characteristics for the Au-Cu FCC Lattice.

Cluster i	Original v_i	Recovered v_i
2	1	0.947
10	0	0.0170
3	0.0224	0
12	0.0622	0.0764
4	0.0576	0
32	0.0129	0
5	0.0157	0

The "reliable zone" of chemical potentials was again determined using the consistency score (Figure 4.10a) and the final choice of clusters was determined by the frequency with which they were picked up by the algorithm for each chemical potential within this zone (Figure 4.10b). In this case, a *reduced* set of clusters was recovered, excluding the 4-body cluster and many of the 2-body clusters, but including a new longer-range pair interaction, shown as cluster 10 in Figure 4.8a. This new set of clusters correctly reproduces the ground states as well as the on-the-hull degenerate configurations identified using the original CE as can be seen in Figure 4.8b. MC simulations applied to the recovered CE also faithfully reproduces the phase behavior of the system to within a scaling factor, visible in Figure 4.9b.

While the recovered CE in this example differs qualitatively from the original one in terms of the number and types of clusters, it nevertheless correctly reproduces the ground states and the finite temperature phase diagram. Equation (4.12) guarantees a deterministic set of clusters and ECIs, but it does not necessarily guarantee the *same* set of clusters will be picked up as those used to generate the high temperature data. By using the MAXENT method, we bias our recovery towards specific sets of solutions. This example illustrates that multiple sets of clusters and ECIs can generate the same phase behavior. Therefore, while the original set of clusters and ECIs can produce the

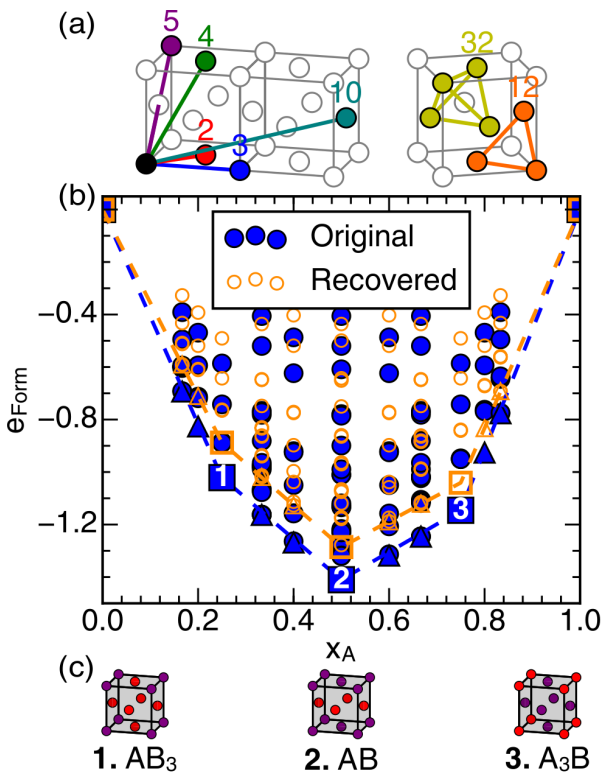

Figure 4.8: (a) shows the six initial cluster prototypes (2, 3, 4, 5, 12, 32) used to generate data, as well as the newly recovered cluster prototype (10). (b) shows the composition versus formation energy for all configurations in supercells containing up to 6 sites, and selected supercells containing up to 8 sites. Squares indicate ground states and are numbered to match (c), triangles indicate degenerate configurations that lie along, but do not deform, the common tangent between adjacent ground states. (c) shows schematic cells of the three ordered ground states. Red circles represent particle A, $\sigma_i = +1$, and purple circles represent particle B, $\sigma_i = -1$.

phase diagram in Figure 4.9a, we have recovered another solution with qualitatively the same phase behavior.

4.5 Discussion

We have introduced a method to parameterize an atomistic Hamiltonian that is capable of accurately predicting both the thermodynamic ground states as well as the full phase diagram at finite temperature using only information about the disordered state. We demonstrated the approach for binary alloys modelled with CE Hamiltonians, which express the dependence of the energy of a multi-component crystal as a linear expansion of cluster basis functions. The foundation of the approach rests on a thermodynamic interpretation of the CE formalism: extensive cluster basis functions, Φ_α, and their corresponding effective cluster interaction (ECI) coefficients, V_α, form conjugate pairs like

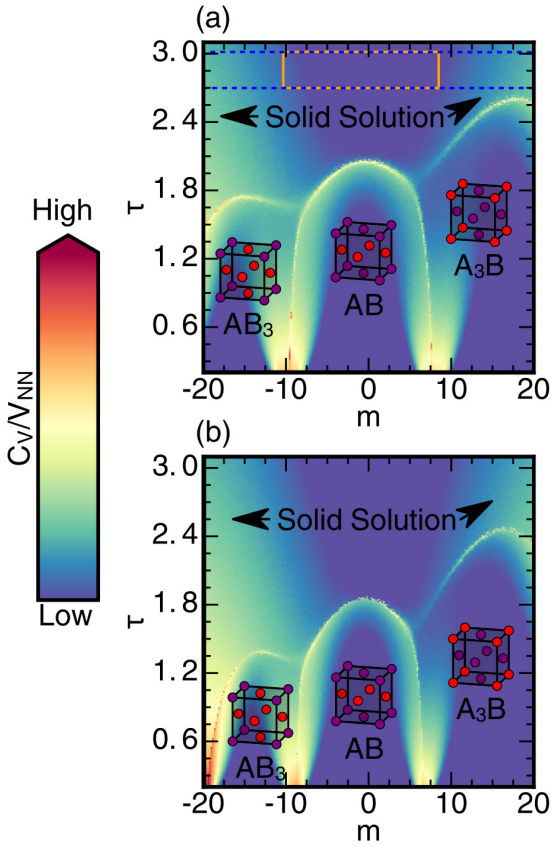

Figure 4.9: Plots (a) and (b) show logrithmic heatmaps of the heat capacity C_V (scaled by V_{NN}), using the original and recovered ECIs, respectively. The approximate phase boundaries are visible as sharp shifts in color, and appear at nearly identical locations in both phase maps, save for a slight amount of scaling. The blue dashed lines indicate the range of temperatures across which observations were taken, while the orange lines match those in Figure 4.10a.

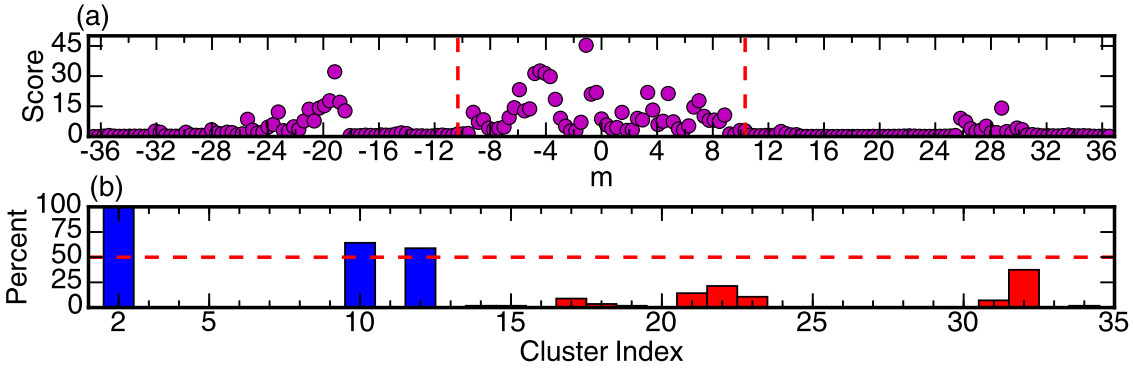

Figure 4.10: (a) shows the score (Equation (4.13)) calculated at each chemical potential (purple dots) using the recovered clusters and ECIs found via our algorithm. Only data from between the dashed, orange lines was used for subsequent analysis. (b) shows the fraction of runs each cluster appeared in; only clusters above the cutoff ($\geq 50\%$, red dashed line) were used in the final regression to determine the ECIs.

any other set of thermodynamic variables. Such an interpretation reveals the existence of Maxwell relations that can be converted to a set of equations (Equation (4.7)) relating two sets of measurable quantities (i.e., the covariance between pairs of extensive cluster functions and the temperature derivative of the ensemble averages of extensive cluster functions) to the unknown ECI of a CE.

CEs parameterized from first principles tend to be sparse, and not require the complete set of basis functions. We have shown that a thermodynamic interpretation of the ECIs also implies a free energy-like function, Equation (4.9). This free energy-like function has a maximum which corresponds to a specified set of basis functions to be retained in a truncated expansion consistent with the *observed* averages of the cluster basis functions. This follows from Jaynes' maximum (information) entropy or MAXENT approach.

The two properties described in Equations (4.7) and (4.12) emerge from a thermodynamic interpretation of the CE formalism. These thermodynamic features motivate and support an iterative algorithm for the parameterization of an effective Hamiltonian to high temperature observations. The final step relies on a regression model to invert Equation (4.7). However, since the measured system is exactly determined (one linear relation and one unknown for each cluster basis function of a CE), direct inversion of Equation (4.7) becomes both numerically unstable and computationally intractable as the number of cluster basis functions becomes exceedingly large in the thermodynamic limit. Furthermore, most multi-component solids can be accurately described with a sparse CE where only a small subset of the ECI are non-zero. Hence, ordinary least squares is not a suitable method for regression, even if only considering the first n rows and first $m < n$ columns of Equation (4.7). Furthermore, we are also prohibited from sparsity-preserving techniques such as LASSO[239] due to the nature of both the regressors (the covariances) and the observed variable (the change in extensive cluster functions with temperature),

an issue further detailed in Section 4.5.2. It is in this context that an initial step involving a maximization of the free energy, Equation (4.9), using an approximation for the disordered state, Equation (4.12), can guide the selection of a sparse truncated CE (i.e., a sparse set of non zero ECI). Iteration between inverting a sparse form of Equation (4.7) and maximizing Equation (4.9) then leads to a Hamiltonian that is consistent with high temperature measurements of the disordered state. As our three examples illustrated, the Hamiltonians parameterized this way are capable of reproducing the ground state orderings as well as the topology of finite temperature phase diagrams with remarkable accuracy.

The approach introduced here differs from conventional inverse MC schemes[238, 243–246], which seek to recover interaction parameters of a Hamiltonian from measures of average cluster functions. While inverse MC methods can generate similar Hamiltonians as the approach introduced here, they require a new round of MC simulations for each step in the gradient descent towards the "correct" ECIs. Furthermore, inverse MC methods provide no proscription as to *which* cluster basis functions to query, leading to instability of the solution when numerous spurious cluster functions are considered simultaneously for the case of a sparse ground-truth. The approach of this work, in contrast, does not require iteration with MC and relies on an agnostic approach in the selection of relevant cluster basis functions. In fact, the step relying on Equation (4.9) can also be incorporated in conventional inverse MC schemes as a way of cluster function selection.

We have said much about "experimental observables" without yet discussing how the $\langle\overline{\Phi}\rangle$ and $\mathbf{cov}[\overline{\Phi},\overline{\Phi}]$ may actually be obtained. Ultimately, the extensive cluster functions are merely the products of site occupation variables, and so if provided with exact atomic data, one would map each site onto a lattice, assign a spin variable, and be able to directly calculate $\overline{\Phi}$. The averages and covariances of the clusters can then be calculated by sub-dividing a sufficiently large observation into N smaller observations and taking

averages and covariances across this collection of observations. This sort of exact atomic information is available via atom probe tomography, which can yield observations with volumes on the order of 10^6 nm^3[247] or 10^8 unit cells. High-angle annular dark-field imaging (HAADF-STEM) can also provide atomic-scale resolution of a sample as well, and by varying the depth of focus, a 3D image image can be obtained over a comparable volume[248]. Atom probe and HAADF-STEM do not provide 100% coverage of the volumes they query, but each provides a sufficient overabundance of information as to allow for some guesses at the unknown zones. Less directly, information on pair correlations can be obtained via techniques such as x-ray and electron diffraction, the covariances of the pair cluster functions using fluctuation microscopy[249], and short-range pair and multi-body terms using nuclear magnetic resonance (NMR) multiple-quantum experiments[250]. However, rather than use diffraction or NMR techniques directly, it is likely these could be used to supplement any interpretation of atom probe or HAADF-STEM analysis, providing better guesses at information that may be missing.

While the approach introduced here has been developed in the context of a binary alloy Hamiltonian, it can be used to invert any effective Hamiltonian that is expressed as a linear expansion of basis functions of relevant DOFs. The linear expansion coefficients that measure the weight of a particular basis function in the effective Hamiltonian can again be interpreted as a thermodynamic variable. Equations similar to (4.7) and (4.12) can then be derived that, through an iterative procedure, enable the parameterization of interaction coefficients using measurements in a high temperature phase. The types of Hamiltonians that can be analyzed in this manner include multi-component (i.e., ternary, quaternary, etc.) CEs, spin-CEs describing non-collinear magnetic solids [216] and lattice dynamical Hamiltonians in the harmonic approximation and beyond.[135, 137, 213, 236, 251]

4.5.1 The Effects of Order and Too Much Data

Our selection algorithm provides a unique set of clusters that can describe the observed data; the final values of the ECIs (to within $> 0.5\%$) do *not* rely on the order in which clusters are considered. As the nature of Equation (4.10) does not depend on which subspace of clusters is chosen (the covariance matrix is, regardless, semipositive definite), results for $\Delta\Upsilon_j$ will remain correct in sign even if some clusters have previously been included incorrectly. However, if the measurements (rows) utilized in our regression are dominated by noise, rather than signal, the results of the regression behave erratically. Specifically, we have found that if we include *all* measurements available to us (limited only by when we have chosen to cease enumerating new extensive cluster functions to measure), the results of our algorithm, and in fact, of any regression (even when selecting the set of ECIs used in the underlying Hamiltonian we were trying to recover), were divergent. In this way, the values entering Equation 4.12 are then no longer representative of the data, making our scheme (and any scheme) meaningless. Therefore, addition to selecting which ECIs to include in the fit, we have also chosen to restrict which measurements we utilize in our regression; these choices are described in the previous section and illustrated in Figure 4.1.

4.5.2 Numerical Accuracy and Impact of Algorithm Choice

In all of our test cases, we were able to recover both the original ground states and the full phase diagram, using only a narrow, high-temperature subset of the data. We have performed other tests using larger quantities of data (e.g., all chemical potentials, and/or all temperatures, or samples from ordered phases) than the regions we chose, including temperatures above all ordering phase transitions, and chemical potentials centered around equiatomic composition. These trials performed strictly *worse* than

the results shown above, selecting dozens of spurious cluster and/or regressing to wildly incorrect ECI values. The reasons for this are related to issues of numerical accuracy, one consequence being that not all locations in phase-space are equal.

In ordered phases, at large chemical potentials and at low temperatures, the accuracy of the empirically measured $\mathbf{cov}\left[\overline{\Phi}, \overline{\Phi}\right]$ drops dramatically. This effect is a consequence of the small number of microstates available at these conditions, an effect magnified in larger clusters (i.e., clusters with a larger radius, or more members). Conversely, at high temperatures, the entries in the covariance matrix will all go to zero, as $k_b T >> V_j$ for all $j \in \alpha$ and the system is driven to total disorder (an effect that is also more pronounced for larger clusters). This means that, even in a system with no ordered phases, we cannot draw from arbitrary locations in phase space.

At extremes of temperature or chemical potential, we begin to introduce large amounts of *heteroskedastic* noise, or, noise that is not identically and independently distributed for all clusters. This heteroskedastic noise is not limited only to extreme regions, though its impact is distinctly lessened at "milder" locations in phase space. In addition to the noise, the entries in the covariance matrix themselves are not independently distributed, since two covariances with a common element are themselves correlated. Nor are they identically distributed, since the variance of larger clusters is more sensitive to smaller changes in the configuration.

As neither the errors, nor the regressors, are independently and identically distributed, performing unbiased regression (e.g., ordinary least squares) on the full set of basis functions returns small (but nonzero) values for nearly all the ECIs instead of the desired sparse solution. Empirically, additional observations only increase over-fitting, rather than sparsity. Compressive sensing techniques aimed at sparsity, such as LASSO, are foiled by the multicollinearity inherent in the entries of the covariance matrix. The heteroskedastic errors present in the data invalidate the results of most common statistical

tests for variable relevance, as well as many cross-validation schemes, as both rely on *identically* distributed (homoskedastic) errors.

4.5.3 Motivation for Ridge Regression in Selection

When performing extensive cluster function selection, we add a penalty term to A proportional to the l^2-norm of the ECIs to guarantee numerical stability of both Equation (4.7) and (4.12) (i.e., ridge regression). The regularization parameter γ is chosen as part of the Bayesian ridge regression scheme as implemented in scikit-learn[252]. By using ridge regression, we are implicitly assuming that the ECIs are Gaussian distributed with a mean of 0[253].

Our second derivatives from Equation (4.10) are now:

$$\frac{\partial^2 \Upsilon}{\partial \overline{V}^2} = -\frac{\mathbf{cov}\left[\overline{\Phi}, \overline{\Phi}\right]}{k_b T} - \frac{2\gamma}{k_b T} < 0. \tag{4.14}$$

For $\gamma > 0$, this guarantees that A (and thus Υ) is negative definite (and has a unique maximum). In the regression portion of the selection step, the addition of a regularization term ensures that the modified covariance matrix has no (near-)zero eigenvalues, preserving the numerical stability of the solution. The trade-off, in the form of (uniform) shrinkage, is that the ECIs recovered are slightly smaller than their "true" values. Shrinkage of the ECIs provides no penalty in the selection stage as long as the sign of the ECIs is preserved. During the final regression after selection has been performed, only ordinary least squares regression is used to avoid solution bias and shrinkage of the ECIs.

4.6 Conclusion

In this Chapter, we have developed a new method to recover relevant interaction coefficients of effective Hamiltonians from experimentally measurable qualities. By careful examination and manipulation of the free energy, a simple mathematical relationship between fluctuations of extensive cluster functions and their related interaction coefficients emerges. The numerical instability of this equation is solved by the development of a secondary criterion, based on the principle of maximum entropy as put forth by Jaynes. Using a single pass through the space of basis functions of the Hamiltonian, we recover a unique solution in polynomial time. The method has been tested in multiple *in-silico* experiments, and faithfully reproduced both the original thermodynamic ground states and the full phase diagrams of each of our simulated systems.

Chapter 5

First-principles Investigation of Competing Magnetic Interactions in Heusler (Mn,Fe)Ru_2Sn Solid Solutions

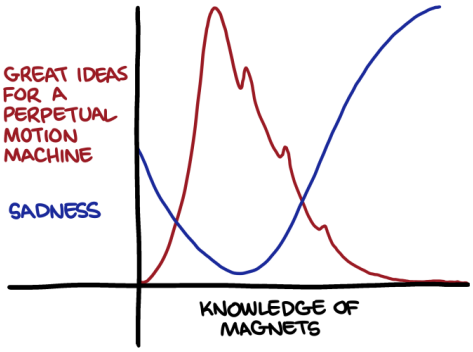

Zach Weinersmith, from "Saturday Morning Breakfast Cereal"

This Chapter forms part of a pair, with Chapter 6, exploring the pseudo-binary Heusler (Mn,Fe)Ru_2Sn. Formed as a solid solution of two full Heuslers, this material has recently been shown to exhibit exchange hardening suggestive of two *magnetic* phases, despite existing as a single *chemical* phase. Here, we have performed a first-principles study of the chemical and magnetic degrees-of-freedom to determine the origin of the unique magnetic behavior responsible for exchange hardening within a single phase. We find a transition from antiferromagnetic (AFM) to ferromagnetic (FM) behavior upon replacement of Mn with Fe, consistent with experimental results. The lowest energy orderings in $Mn_{1-x}Fe_xRu_2Sn$ consist of chemically- and magnetically-uniform (111) planes, with Fe-rich regions preferring FM ordering and Mn-rich regions preferring AFM ordering, independent of the overall composition. Analysis of the electronic structure suggests that the magnetic behavior of this alloy arises from a competition between AFM-favoring Sn-mediated superexchange and FM-favoring RKKY exchange mediated by spin-polarized conduction electrons. Changes in valency upon replacement of Mn with Fe shifts the balance from superexchange-dominated interactions to RKKY-dominated interactions. These results are used in Chapter 6 to construct a Cluster Expansion Hamiltonian to explore how magnetism and chemistry interact at finite temperature, especially in the (Mn,Fe) disordered solid solution.

5.1 Introduction

The unique electronic properties of full Heusler compounds, defined as $L2_1$-ordered XY_2Z alloys with X and Y as transition metals and Z as a main-group element, make them promising materials for applications in spintronics[254], superconductors[48], magnetocalorics[53], and shape-memory devices[255]. The flexibility of Heusler compounds derives from their ability to realize large and tunable changes in properties with

small changes in the valence electron count[256–259]. Different choices of X and Y can produce various magnetic properties, as both Z-mediated indirect exchange between second nearest neighbor pairs of X, and direct exchange involving X-Y interactions, can give rise to ferro-(FM), ferri-(FrM), or antiferro-(AFM) magnetic configurations[48, 254]. Many Heuslers have been demonstrated to follow Slater-Pauling behavior[258, 260, 261], a subset of which are calculated to be half-metals[260–263], yielding a family of materials with unparalleled magnetic flexibility.

The (Mn,Fe)Ru_2(Ge,Sn) genus of the Heusler family neatly demonstrates the transition from AFM to FrM to FM behavior with a change in the ratio of Fe to Mn as the X element[44, 46]. Mizusaki *et al.*[46] and Douglas *et al.*[44] have shown that both the $Mn_xFe_{1-x}Ru_2Ge$ and $Mn_xFe_{1-x}Ru_2Sn$ alloys exhibit magnetic behavior indicative of two-phase coexistence, evidenced by an increase in magnetic coercivity, in spite of the fact that the alloys form a single *chemical* phase, *i.e.*, a solid solution on the X = Mn,Fe sublattice. The spike in coercivity is theorized to be a consequence of local AFM/FM domains and interactions between the two, creating exchange hardening (broadening of the hysteresis loop) as observed on the macroscopic scale. Exchange bias (shifting of the hysteresis loop) and exchange hardening are both well-studied phenomena in nanocomposites and nanostructured thin films[264, 265] containing distinct FM-favoring and AFM-favoring chemical phases. However, exchange hardening *without* the appearance of a second chemical phase is a phenomenon that, at present, is rarely observed and poorly understood. While previous studies have performed limited *ab-initio* calculations to probe the magnetic behavior of the $MnRu_2Sn$ and $FeRu_2Sn$ end-members[44, 262], no studies at intermediate compositions of the $Mn_xFe_{1-x}Ru_2Sn$ alloy have yet been performed.

Here, we perform density functional theory (DFT)[5, 6] calculations on the $Mn_{1-x}Fe_xRu_2Sn$ alloy across the entire composition range $x = [0, 1]$, and explore both

chemical and magnetic degrees-of-freedom (DOFs). We first probe the origin of FM and AFM ordering in the $FeRu_2Sn$ and $MnRu_2Sn$ Heuslers, respectively, and seek to answer *why* a small change in the electronic configuration causes a dramatic change in magnetic ordering. We consider two models of magnetic interaction proposed for Heuslers to analyze our results: (a) indirect exchange, as a competition between AFM-favoring, Sn-mediated superexchange and FM-favoring, Ruderman-Kittel-Kasuya-Yoshida (RKKY) interactions between the X-sites containing Fe and Mn, and (b) direct exchange, as a consequences of bonding/antibonding/nonbonding interactions between Ru and Mn/Fe. As $MnRu_2Sn$ and Mn-rich $Mn_xFe_{1-x}Ru_2Sn$ alloys are known to be AFM or FrM, we next evaluate a large number of magnetic orderings on the Mn/Fe sub-lattice site, and study the interplay between magnetic and chemical stability. We predict the existence of a miscibility gap at zero kelvin with $Mn_{1-x}Fe_xRu_2Sn$ separating into a two-phase mixture of pure Heuslers (Mn,Fe)Ru_2Sn for all x. The lowest-energy chemical configurations of $Mn_xFe_{1-x}Ru_2Sn$ at intermediate concentrations ($0 < x < 1$) offer insights into the low-temperature magnetic behavior of quenched solid solutions.

5.2 Prior Work: Magnetism in Heuslers

Numerous in-depth studies have been published exploring the origin of magnetism and half-metallic behavior[263, 266, 267], the prevalence and consequences of Slater-Pauling behavior[258, 260, 261], and the FM or AFM coupling of magnetic moments in full Heuslers[257]. These studies can be divided into two general categories, namely, those where: (a) the Y transition metal is assumed to determine the lattice constant and the valence electron count, but does *not* participate in the X-X magnetic coupling[256, 257, 268, 269], and those where (b) the X-Y interactions are assumed to *dominate* the magnetic Hamiltonian[258, 259, 263, 270, 271]. While these two viewpoints assign the

observed magnetic behavior to different underlying causes, the conclusions are largely the same. To best understand which mechanisms determine the AFM-to-FM transition in $Mn_{1-x}Fe_xRu_2Sn$ with increasing x, we examine both philosophies and apply the analysis methods used in each to the pure Heuslers (Mn,Fe)Ru_2Sn.

In the following sections, we offer an overview of magnetism in Heuslers. First, we explore the origin of a magnetic moment, and why Slater-Pauling behavior leads to (near-)integer values of the magnetic moment. Next, we review the two models of magnetic interaction given for Heuslers. In the indirect-exchange only model, we discuss two different competing modes of indirect exchange that can couple the Mn and/or Fe containing X sites without the participation of Ru residing on the Y-sites. In the direct-exchange model, we explore the possibility of X-Y (*i.e.*, Mn/Fe-Ru) interactions being the *dominating* influence on whether FM or AFM configurations are realized.

5.2.1 Slater-Pauling Behavior

Galanakis *et al.*[260, 261] have demonstrated that many full Heusler alloys follow Slater-Pauling behavior, such that the total ferromagnetic moment is a linear function of the valence electrons:

$$M_t = Z_t - 24, \tag{5.1}$$

where M_t is the total moment, Z_t is the number of valence electrons, and 24 is the total number of occupied spin-up plus spin-down valence bands in a traditional XY_2Z Heusler. While common, Slater-Pauling behavior is not universal; as the valence electron count approaches and passes 30, Galanakis *et al.* note that the total moment stops rising in integer steps. The number 24 arises from the 12 electrons occupying the minority bands, which require 12 electrons in the majority bands to reach zero moment; additional valence electrons do *not* change the occupation of the minority states, and so the moment is

determined by the number of electrons past parity[1]. In the case of Mn- or $FeRu_2Sn$, the twelve occupied minority states are: one Sn s, three Sn p, five hybridized Fe/Mn-Ru_2 d and another three non-bonding Ru_2 d states. Due to exchange splitting, those twelve states, plus an *additional* three (Mn) or four (Fe) states, are occupied by the majority spin. The states closest to the Fermi level are, however, delocalized conduction electrons and not easily assigned to localized orbitals.

Depending on the size and electronegativity of the Y element (Ru, in our case), the total moment may be localized only onto X (*e.g.*, Mn in $MnRu_2Z$ compounds), or shared among the X and Y sites with the moment on Y being as large as 1 μ_B (*e.g.*, Co in $MnCo_2Z$ compounds)[261]. When Y is a heavier element with better-shielded (and hence more delocalized) valence electrons and a larger atomic radius (like Ru or Rh), the X-Y hybridization is smaller than for a lighter Y with more tightly bound d electrons (like Fe or Co) and a smaller atomic radius. This reduced hybridization results in less moment being assigned to the Y species in a Wigner-Seitz cell integration.

Overall, there are three ways to change the valence electron count Z_t, with differing levels of side-effects. Selecting different elements for X (*e.g.*, Mn versus Fe) can change Z_t, but can also alter the ground state magnetic configuration. Modifying Y (*e.g.*, Ru versus Rh) can change Z_t without significantly affecting other magnetic properties when moving within a heavier group (where the valence electrons are more delocalized). For any main group element Z (*e.g.*, Sn versus Ge), the d states are so far below the Fermi level as to play no role in determining magnetic effects. Furthermore, their atomic radii are too small to set the lattice constant (compared to Y). Main group Z elements, therefore, only act as an electron sink, changing Z_t without affecting any other properties. By tuning the exchange splitting with a careful choice of X and/or Y, and by tuning the

[1]at roughly 30 electrons, this rule begins to break down: the exchange-splitting required to push electrons into the highest-energy anti-bonding orbitals is infeasibly large

filling via Z, it is possible to realize half-metallic and nearly half-metallic alloys. Many half-metallic Heuslers, such as $MnCo_2$(Al/Ga/Si/Ge/Sn)[272] and VMn_2(Ge/Al)[271], have been studied via *ab-initio* calculations.

5.2.2 Indirect-Only Model: Superexchange and RKKY Exchange

The first model of exchange developed for Heusler alloys proposes a collection of localized moments on the X site (Mn or Fe here) interacting via competing AFM-favoring superexchange and FM-favoring RKKY couplings[256, 257, 268]. As the X-X distance in Heuslers is always larger than $2r_X$, where r_X is the Van der Waals radius of X, the majority of X-X exchange is presumed to be indirect. The strongly AFM superexchange interaction is mediated by the Z atoms (Sn here), which sit between second-nearest-neighbor X-X atom pairs. In contrast, RKKY-type exchange undergoes decaying oscillations with interatomic distance and can be FM or AFM. This interaction is the consequence of a large localized moment inducing a decaying oscillation in the spin-polarization of the conduction electrons. Figure 5.1 illustrates, schematically, the spin polarization and occupations involved in both types of indirect exchange. For the interatomic distances of relevance in the $Mn_{1-x}Fe_xRu_2Sn$ alloys, the dominating terms of RKKY interaction are ferromagnetic[256, 273].

The Y atoms (*e.g.*, Ru) within the indirect-exchange model can play two roles: they can affect the lattice constant, and they can contribute to the total valence electron count. Both factors *indirectly* influence the exchange interactions between the X atoms. Superexchange depends on orbital overlap between neighboring X-Z atoms and is reduced in magnitude by increasing the lattice constant. RKKY interactions reduce in magnitude and potentially change sign with a change in interatomic distance. Both superexchange and RKKY exchange parameters scale inversely with the energy required to promote an

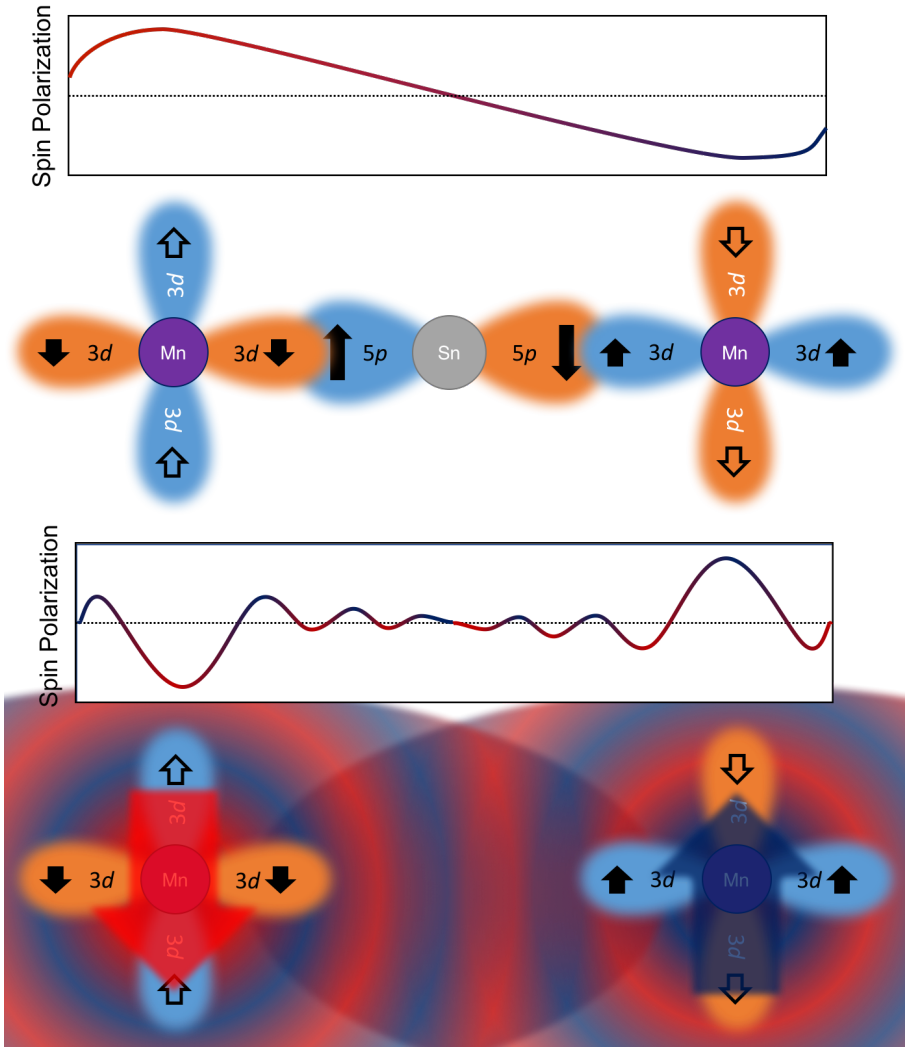

Figure 5.1: (Top) Sn-mediated Superexchange, where AFM orientation of Mn-Mn pairs is driven by overlap between the Mn d orbitals and the Sn p orbitals. The fully-occupied Sn p orbital has alternating signs on either lobe; the large degree of spatial overlap with the partially-occupied Mn d orbitals drives a preference for AFM pairing between the Sn and Mn electrons, and hence, an AFM pairing between the Mn pairs. (Bottom) RKKY exchange, where large, localized magnetic moments on the Mn sites drive an oscillating polarization of the delocalized conduction electrons. While the Mn pairs are spatially separated for direct exchange to be possible, the conduction electrons can transmit information about the magnetic moments across the gap.

electron from a X d-state to the Fermi level and depend on the number and distribution of states both immediately below and above the Fermi level[269, 273]. The exact elec-

tronic configuration of the Y atom (beyond the number of valence electrons) is otherwise considered unimportant in determining magnetic behavior. An assumption is made that the (usually heavy) Y element has sufficiently delocalized electrons as to play no particular role in the overall electronic structure near the Fermi energy. Kübler *et al.* go so far as to state "We find that the [Y] atoms (*e.g.*, Cu, Pd) serve primarily to determine the lattice constant [...]", though they do acknowledge the possibility of Y-mediated exchange in the case of light, ferromagnetic Y elements such as Co and Ni[257].

The scaling of the competing superexchange and RKKY exchange parameters can be qualitatively understood using a perturbative approach, where the coupling constants j_{RKKY} and j_s at the gamma point in reciprocal space ($q \to 0$) reduce to[273]:

$$j_{RKKY}(0) = V^4 D(\epsilon_F)/E_h^2, \tag{5.2}$$

$$j_s(0) = V^4 \sum_{nk}^{\epsilon_{nk}>\epsilon_F} (\epsilon_F - \epsilon_{nk} - E_h)^{-3}. \tag{5.3}$$

V is an electronic mixing parameter, $D(\epsilon_F)$ is the density of states at the Fermi level, ϵ_F is the Fermi energy, ϵ_{nk} is the energy of a state at k-point k in band n, and E_h is the energy required to promote an electron from a d-state of X to the Fermi level. Şaşıoğlu *et al.*[269] performed an in-depth exploration of the competition between j_{RKKY} and j_s, using Mn-based Heuslers as examples. Their general conclusion is that a large number of states at (or just below) the Fermi level favor RKKY-type exchange, while a large number of states just above the Fermi level favor superexchange. The relative stability between FM and AFM behavior can, therefore, be altered by either varying the number of electrons with the chemistry on the X site, or by changing the lattice constant.

5.2.3 Direct Model: X-Y Exchange

The second model of exchange for Heuslers drops the presumption that the Y sites do not participate significantly in exchange. The effects of Y-mediated exchange are explored in-depth by Şaşıoğlu *et al.*[263, 270, 271] in numerous Heusler systems for lighter Y elements such as Co and Fe. Dronskowski *et al.*[259] offer a bonding/antibonding-motivated discussion of the origin of AFM/FM behavior in Heuslers, demonstrating that even in cases where the Y element is a heavier element (*e.g.*, Ru), X-Y exchange interactions play a leading role in determining the magnetic configuration of the Heusler. In cases where Y participates directly in exchange, two types of interactions must be considered for XY_2Z Heuslers: X-Y exchange and Y-Y exchange. As the two Y sites occupy interpenetrating FCC sub-lattices, the Y-Y distance is usually below $2r_Y$, and so direct exchange between the two Y may be significant. The X-Y distance can also be smaller than $r_X + r_Y$, leading to direct X-Y exchange; however, as both X and Y have partially-occupied *d*-states, this mechanism differs from the X-Z superexchange via Z's fully-occupied *sp* states (*e.g.*, Mn-Ru direct exchange would look different than Mn-Sn-Mn superexchange in $MnRu_2Sn$).

The potential Y-Y interactions can be FM or AFM depending on the ratio of interatomic distance to the *d*-orbital radius, in a similar fashion to pure transition metal elements on the Bethe-Slater curve[274]. Similarly, the X-Y interactions can be FM or AFM, while the X-X interactions are presumed to be purely FM owing to the large interatomic separation. The magnitudes of the Y-Y interactions are typically very small compared to those of the X-Y interactions or even the X-X interactions[258, 263], and hence, a simple model can be constructed with three couplings: X-Y (FM or AFM), X-X nearest-neighbor (NN) (always FM), and X-X next-nearest-neighbor (NNN) (FM or AFM, depending on the superexchange-RKKY competition). Even with only three coupling constants, very

complex ordering phenomena can arise, depending on the sign of the X-Y and X-X NNN interaction and on the relative magnitude of all three interactions[237, 275–277].

5.3 Methods

5.3.1 *Ab-Initio* Calculations

General details about the electronic structure calculations performed in this Chapter are available in Section 2.3. All calculations were performed spin polarized unless otherwise noted, with an energy cutoff of 540 eV and a k-point grid with $17 \times 17 \times 17$ divisions in the unit cell (and scaled with reciprocal supercell size). All local properties (*e.g.*, site-specific magnetic moments or atomic charges) were determined using the Wigner Seitz radii provided with the pseudopotentials. Non-neutral calculations were performed utilizing a homogeneous compensating background charge, fixing lattice vectors and atomic coordinates to those of the lattice of the neutral parent structure. The LOBSTER software package[278–280] (version 2.1.0) was used for the calculation of Crystal Orbital Hamilton Populations (COHP) to analyze bonding[281]. We utilized the pbeVaspFit2015 basis set[282] and selected per-element basis functions matching the electrons treated as valence electrons in the pseudopotentials.

5.3.2 Enumeration of Configurations

The energies of all symmetrically-distinct configurations of chemical identity (Fe, Mn) and magnetic spin (negative or positive per-site moment) within supercells containing up to four unit cells were calculated using VASP with the settings described above. One configuration containing six unit cells at $x_{Fe} = 0.33$ was also considered, as the lowest-energy three-unit-cell supercell corresponds to a high-energy, magnetically-

frustrated state.Volume and site relaxations were minor ($0.998 < V/V_0 < 1.009$, and mean-squared-displacement $< 0.7 \times 10^{-3}$ Å); however, magnetic relaxations were significant. While VASP prohibits changes of the magnetic moments that would lower symmetry (*e.g.*, FM to AFM), changes that add additional symmetries, or move to a different magnetic configuration with the same symmetry, are allowed. Multiple instances of AFM structures relaxing to otherwise-enumerated FM structures were found; the initial AFM structures were considered unstable and were removed from further calculations. More interestingly, several cases were found where one AFM or FrM configuration would relax into its spin-reversed twin (*i.e.*, applying the time-reversal operator), and visa-versa ($A \rightarrow B$ and $B \rightarrow A$). In the cases where multiple initial magnetic configurations relaxed onto the same final configuration, the structure with the lowest energy was kept and the others discarded.

5.4 Results and Discussion

5.4.1 Electronic Structure of $MnRu_2Sn$ and $FeRu_2Sn$

To understand the potential causes of complex magnetic behavior in $0 < x < 1$ solid solutions of $Mn_{1-x}Fe_xRu_2Sn$, we first sought to understand the electronic difference between the $x = 0$ and $x = 1$ end-members. $MnRu_2Sn$ possesses $L1_1$ (*i.e.*, (111) spin-up planes alternated by spin-down planes) AFM ordering on the Mn FCC sublattice with a large moment on Mn and no moment on Ru. $FeRu_2Sn$, in contrast, is FM with a large moment on Fe and a small-but-nonzero moment on Ru[44]. In the course of our enumeration, we examined many different AFM and FrM magnetic orderings of the pure Heuslers (Mn,Fe)Ru_2Sn. The experimentally-observed magnetic orderings (AFM for Mn and FM for Fe) were found to be the ground states, with energy differences of 24 meV and

87 meV (per primitive cell) to the next-lowest-energy magnetic orderings for $MnRu_2Sn$ and $FeRu_2Sn$, respectively. In addition to the fully-relaxed structures, we calculated total and local moments of cells having the experimental lattice constants and of cells having an averaged lattice constant between the end-member constants. In both cases the internal ionic DOFs were fully relaxed. Table 5.1 compares calculated total and local site magnetic moments with experimental total saturation magnetizations measured at 5 T and 4 K and per-site moments extracted from Rietveld refinements of neutron powder diffraction data.

Table 5.1: Total and per-site magnetic moments for $MnRu_2Sn$ and $FeRu_2Sn$ obtained from DFT calculations using different lattice constants, as well as experimental measurements.

System	$MnRu_2Sn$ Moments (μ_B)			$FeRu_2Sn$ Moments (μ_B)		
	Total	Mn	Ru	Total	Fe	Ru
DFT (Full Relax)	0.0	3.155	0.078	4.141	3.065	0.497
DFT (Exp. Lat. Const.)	0.0	3.140	0.078	4.136	3.057	0.498
DFT (Mean Lat. Const.)	0.0	3.134	0.071	4.137	3.059	0.498
Experiment	0.0	3.4(1)	0.0	3.4	3.16(4)	0.4(1)

The moments obtained from DFT in all cases compare favorably to the experimental results, except for the saturation magnetization in $FeRu_2Sn$, where the lower-than-anticipated experimental moment in the FM case arises from the dispersion of grain orientations and the presence of grain and magnetic domain boundaries in the experimental sample[44]. The relaxed DFT lattice parameters of 6.22 Å and 6.21 Å for $MnRu_2Sn$ and $FeRu_2Sn$, are also in good agreement with the experimental lattice constants of 6.20 Å and 6.19 Å as measured with neutron diffraction at 15 K by Douglas *et al.*[44]. The fully-relaxed lattice constants are slightly larger than the experimental values; the lattice constant is set by Ru (the element with the largest radius), and PBE is known to systemically overestimate lattice constants for $5d$ elements[283].

The transition from AFM to FM ordering when going from $MnRu_2Sn$ to $FeRu_2Sn$ is somewhat unexpected considering that Mn and Fe differ by only one electron and one proton. We can understand this transition, as well as the likely intermediate states for a disordered Mn/Fe solid solution, by analyzing how the electronic structure around the Fermi level changes with a change in the X element. To most easily compare reciprocal-space properties, all of the following calculations were performed using the mean lattice constant between the experimental $MnRu_2Sn$ and $FeRu_2Sn$ values. The density of states (DOS) of the non-spin-polarized (referred to hereafter as non-magnetic, or NM, for simplicity[2]) Heuslers are shown in Figure 5.2, along with the projected DOS of the Mn/Fe and Ru d-states. Figure 5.2 clearly shows large changes in the states available above and below the Fermi level when going from NM $MnRu_2Sn$ to NM $FeRu_2Sn$. In the Mn Heusler, there are substantially more states just above the Fermi level than below it, while in the Fe Heusler, the reverse is true. Far below the Fermi level the electronic structures of both Heuslers are nearly the same. At the Fermi level, the behavior is closer to a rigid-band model, with the movement focused on the Mn/Fe site.

We can connect these differences in the Fermi-level states back to the indirect-exchange-only model of magnetic ordering, *i.e.*, as a competition between superexchange and RKKY exchange. Both Mn- and Fe-rich Heuslers have a large DOS at the Fermi level, driving a large RKKY term, but in Fe there is a large drop-off just past the Fermi level. The superexchange interaction, j_s in Equation 5.3, is bounded from above by $j_s(0) \leq V^4 N/E_h^3$, where N is the number of unoccupied states near the Fermi level[273]. Therefore, in Mn, where N is large, $|j_s|$ should be greater than $|j_{RKKY}|$, and AFM behavior should dominate. In Fe, where N is smaller, $|j_s|$ should be smaller than $|j_{RKKY}|$, and FM behavior should dominate. It is worth noting here that $D(\epsilon_F)$ in the Fe-Heusler

[2]Non-spin-polarized should not be taken to mean paramagnetic, in this context. While non-spin-polarized calculations have sometimes been used as a proxy for paramagnetic configurations, we stress that this approach is generally incorrect.

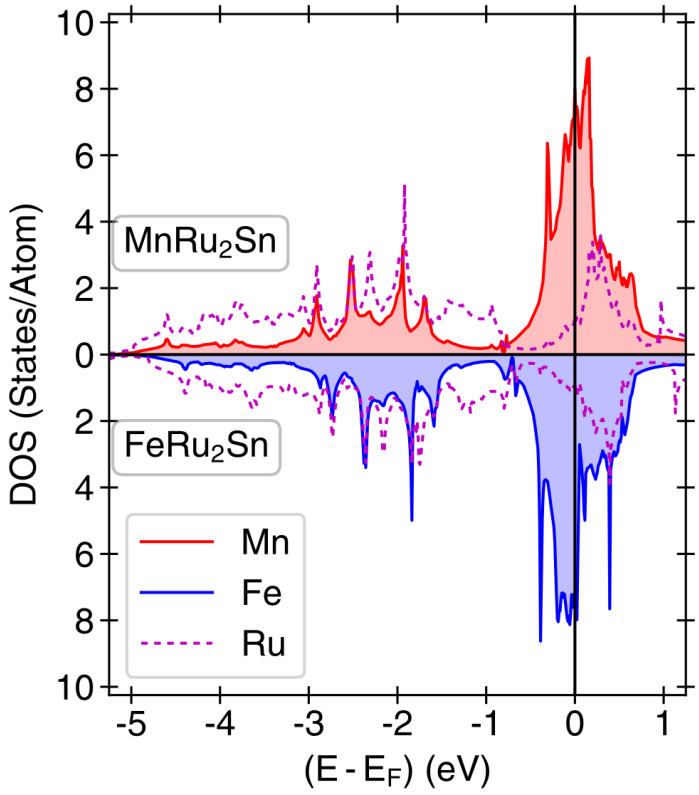

Figure 5.2: Non-spin-polarized site-projected DOS for $MnRu_2Sn$ (above) and $FeRu_2Sn$ (below) for the Mn or Fe and Ru sites; Sn sites contribute states far below the Fermi level (≤ -6 eV) and are not shown. While the states far below the Fermi level are largely unaffected by the addition/subtraction of an extra electron/proton pair, the behavior at the Fermi level changes substantially.

is also smaller than in the Mn-Heusler, and so the overall magnitudes of the coupling constants are expected to be smaller.

The differences in the states near the Fermi level persist into the spin-polarized calculations. The Mn or Fe site-projected DOS for the FM and $L1_1$ AFM configurations are shown in Figures 5.3 a and c, with corresponding formation energies in Table 5.2.

Table 5.2: Relative formation energies per primitive cell of various magnetic and electronic configurations of $MnRu_2Sn$ and $FeRu_2Sn$. All energies represent fully-relaxed structures.

System	FM - NM (eV)	AFM - NM (eV)	FM - AFM (meV/μ_B)
$MnRu_2Sn$	1.305	1.357	16.7
$[MnRu_2Sn]^{-1}$	2.025	2.036	2.6
$FeRu_2Sn$	1.084	0.998	-20.8
$[FeRu_2Sn]^{+1}$	0.716	0.753	11.9

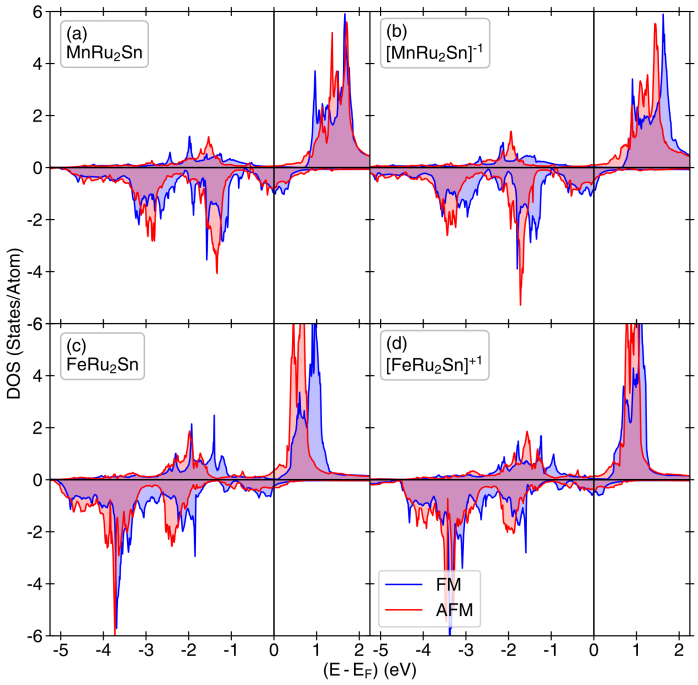

Figure 5.3: Spin-polarized site-projected DOS for $MnRu_2Sn$ (a,b) and $FeRu_2Sn$ (c,d), showing per-site Mn or Fe DOS for both FM and $L1_1$ AFM configurations. Panels (b) and (d) have had an electron added or subtracted, respectively, such that the Mn-Heusler has the same number of electrons as the Fe-Heusler, and vise-versa.

For the Mn-Heusler, the Fermi level resides at approximately the middle of a broad peak of both the total DOS and the projected DOS at the Mn site (see Figure 5.3 (a)). This matches the behavior of the NM states, suggesting dominance of the superexchange interaction over the RKKY interaction, resulting in the energy of the AFM phase being more than a dozen meV (per primitive cell) below that of the FM phase. Both the FM and AFM orderings are also far lower in energy (>1 eV per primitive cell) than the NM state, indicating a large driving force towards magnetization.

The Fermi level in the FM Fe-Heusler lies at the start of a near-gap where the DOS is at a minimum for the minority spin, and just past a peak in the majority spin (see Figure 5.3 (c)). The presence of the majority-spin peak immediately before the Fermi level leads to a large RKKY contribution to the coupling in the FM configuration of the Fe-Heusler. In the AFM configuration, however, the very local maximum immediately after the Fermi level is still smaller than the maximum before the Fermi level in the FM configuration. This implies that the degree of superexchange (AFM-favoring) coupling in

the AFM configuration is far smaller than the degree of RKKY (FM-favoring) coupling in the FM configuration, leading to FM being lower in energy.

To establish the importance of nuclear charge/effective potential on magnetism, we also considered FM and AFM configurations of Mn- and $FeRu_2Sn$ when one electron is added or subtracted, respectively. The change in total electron count serves to give $MnRu_2Sn$ the same valency as $FeRu_2Sn$, and vice-versa. When an additional electron is added to $MnRu_2Sn$, the Fermi level moves to higher energy, but the dispersion of the bands also broadens as the additional electron induces further delocalization, as seen in Figure 5.3 (b). As a consequence, while the energy *difference* between FM and AFM orderings decreases upon addition of an extra electron to $MnRu_2Sn$, there are still a sufficient number of states above the Fermi level to (barely) prefer the AFM ordering.

Conversely, when an electron is subtracted from $FeRu_2Sn$, the states become more localized (owing to less Coulomb repulsion) *and* the Fermi level moves to lower energies, putting the Fermi energy directly in the middle of the large DOS peak in the FM configuration as seen in Figure 5.3 (d). This new distribution of states around the Fermi level implies that $|j_s|$ is now much closer in magnitude to $|j_{RKKY}|$, destabilizing the FM state. In contrast, the removal of an electron from AFM $FeRu_2Sn$ has virtually no effect on the electronic structure near the Fermi level. As a result, the energy change upon removal of an electron penalizes the FM state more than the AFM, so much so that for $FeRu_2Sn$ it alters the ground state from FM to AFM. This effect becomes evident upon inspection of the change in energy when going from the NM state to the FM and AFM states. Table 5.2 shows that the AFM state gains more in energy compared to the FM state relative to the NM state in $FeRu_2Sn$ upon subtraction of an electron (by approximately 100 meV per primitive cell).

There is another subtle, yet relevant difference between $MnRu_2Sn$ and $FeRu_2Sn$: in the FM configuration, Mn and Ru are AFM aligned to one another, while Fe and Ru are

FM to one another. This suggests that there are also interactions that couple the X (*i.e.*, Mn and Fe) and Y (*i.e.*, Ru) sites, and that these couplings may be important. We can estimate the relative strengths of Ru-Ru, Ru-Mn/Fe and Mn/Fe-Mn/Fe interactions by fitting a rudimentary magnetic Hamiltonian to DFT supercell calculations at fixed total moment. The simplest Hamiltonian takes the form

$$E = j_0 + 3j_1\langle\phi^{NN}_{Ru}\rangle + 6j_2\langle\phi^{NN}_{Mn/Fe}\rangle + 3j_3\langle\phi^{NN}_{Mn/Fe}\rangle + 4j_4\langle\phi^{NN}_{Ru,Mn/Fe}\rangle, \tag{5.4}$$

where E is the energy per primitive cell, j_0 can be interpreted as the energy gain from exchange splitting, j_1 is the Ru-Ru coupling, j_2 and j_3 are the nearest-neighbor and next-nearest-neighbor Mn/Fe-Mn/Fe couplings, respectively, and j_4 is the Ru-Mn/Fe coupling. The ϕ are the products of site-projected moments for Ru, Fe, or Mn, for either nearest-neighbor (NN) or next-nearest-neighbor (NNN) pairs. The coefficients 3, 6, 4, and 3 correspond to the number of (next-)nearest-neighbor pairs per primitive cell. We stress that while the j_i are *not* the true exchange constants and are not suitable for building a more complex model, their magnitudes should give an indication of the relative strength of each type of interatomic coupling. Curves of the formation energy (referenced against the NM calculation) versus the net moment as calculated with PBE are shown in Figures 5.4 a and b, with the values of j_0, j_1, j_2, j_3, and j_4 fit to these curves given in Table 5.3.

The leading terms in both $MnRu_2Sn$ and $FeRu_2Sn$ are the j_0 exchange-splitting energy. While the j_1 terms have similar magnitudes as the j_0 terms, the *contributions* from the Ru-Ru interactions are overall small, as the magnitude of the Ru moments are 0.1 to 0.01 times smaller than the Fe or Mn moments, respectively. The calculated contributions of each term for the lowest-energy FM configuration of each Heusler are given in the second part of Table 5.3, making the difference in magnitudes more obvious. These

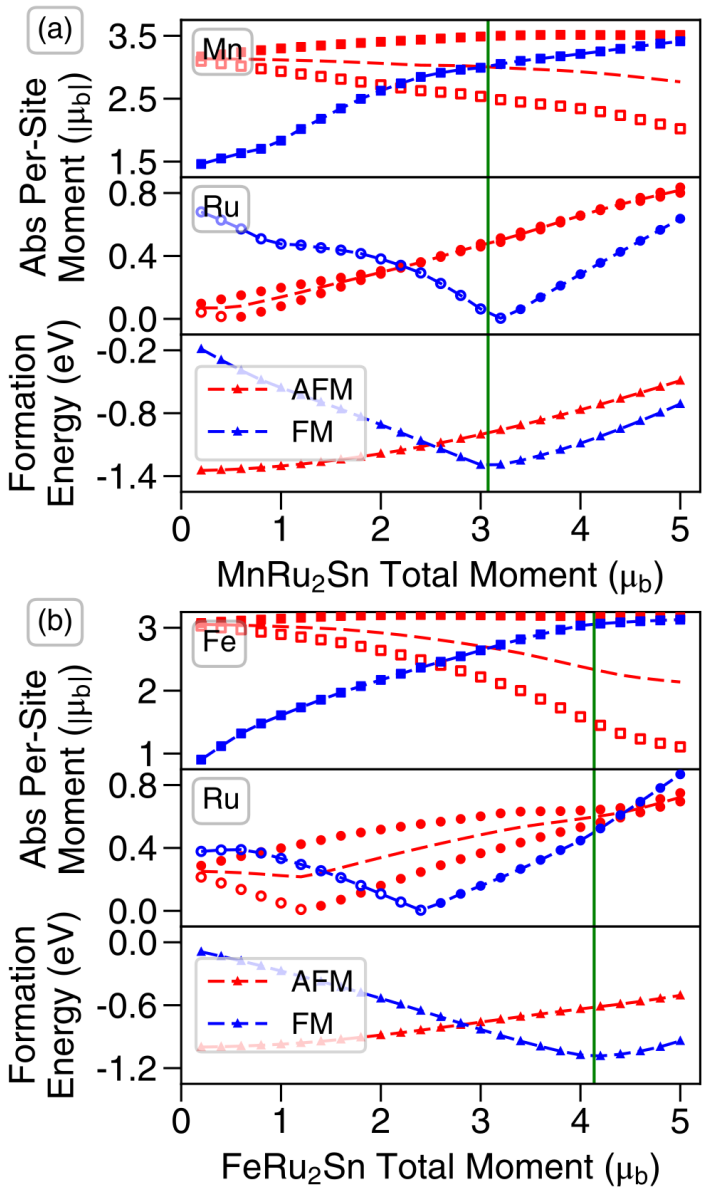

Figure 5.4: Formation energies and site-specific magnetic moments for total-moment-constrained DFT calculations in $MnRu_2Sn$ (a) and $FeRu_2Sn$ (b). Absolute values of magnetic moments are shown in the top two plots of (a) and (b), where the chemical symbol specifies which site-projection is being measured, and full versus hollow symbols indicate a positive or negative sign of the moment, respectively. In the AFM cases, the moments of both the symmetrically-distinct Mn/Fe/Ru sites are indicated, while the average of the absolute value of the moment is given by the dashed line bisecting the sets of markers. Green vertical lines indicate the equilibrium (minimum-energy) total moment.

results tell us three things: (a) Mn-Mn interactions dominate in $MnRu_2Sn$, (b) Fe-Fe interactions are the most important in $FeRu_2Sn$, and (c) Ru-Ru and Ru-Fe interactions are also relatively important in $FeRu_2Sn$. From the signs of the j_i's we can also conclude that Ru-Ru prefers an AFM-type ordering (though the energy change for this preference is small), and that Ru-Mn prefers an AFM-type ordering (again, small), while Ru-Fe prefers a FM-type ordering (larger).

Table 5.3: Estimated coupling constants j_i fit to the results of Figure 5.4 using Equation 5.4, and the magnitude of the terms for the lowest-energy ferromagnetic and antiferromagnetic configuration of each Heusler.

System	Coupling (meV/μ_B^2)				
	j_0	j_1	j_2	j_3	j_4
$MnRu_2Sn$	-353	331	-31.8	33.4	30.9
$FeRu_2Sn$	-85.1	116.3	-33.2	32.1	-15.9
FM State	Contribution (meV)				
	$3j_1\times$ $\langle\phi_{Ru}^{NN}\rangle$	$6j_2\times$ $\langle\phi_{Mn/Fe}^{NN}\rangle$	$3j_3\times$ $\langle\phi_{Mn/Fe}^{NNN}\rangle$	$4j_4\times$ $\langle\phi_{Ru,Mn/Fe}^{NN}\rangle$	
$MnRu_2Sn$	1.8	-1735	911	-15.6	
$FeRu_2Sn$	86.5	-1864	901	97.1	
AFM State	Contribution (meV)				
	$3j_1\times$ $\langle\phi_{Ru}^{NN}\rangle$	$6j_2\times$ $\langle\phi_{Mn/Fe}^{NN}\rangle$	$3j_3\times$ $\langle\phi_{Mn/Fe}^{NNN}\rangle$	$4j_4\times$ $\langle\phi_{Ru,Mn/Fe}^{NN}\rangle$	
$MnRu_2Sn$	0	0	-984	13.8	
$FeRu_2Sn$	0	0	-898	24.8	

We can gain further insight about the relative importance of Ru-Ru, Mn/Fe-Mn/Fe, and Ru-Mn/Fe interactions with the help of a Crystal Orbital Hamiltonian Populations, or COHP, bonding analysis[281] in the style of Kurtulus, *et al*[259]. COHP provides an "energy-resolved visualization of chemical bonding" and enables the easy visualization of the bonding, anti-bonding, or non-bonding behavior between a pair of sites in a solid. The COHP procedure weights the electronic DOS by entries from the Hamiltonian matrix, *i.e.*, overlap of eigenstates, rather than of orbitals as done in a crystal orbital overlap populations analysis. The resulting set of COHP and energy values looks similar to a DOS plot, but conveys different (but related) information: negative values correspond to bonding states, positive values correspond to antibonding states, and values near zero are interpreted as non-bonding states. The integrated COHP (up to the Fermi level)

indicates the total bonding/antibonding/non-bonding character of the interaction; the lowest-energy structure should be the one that maximizes bonding.

Figure 5.5 shows COHP analyses for $MnRu_2Sn$ and $FeRu_2Sn$, respectively, contrasting NM, FM, and AFM configurations. All COHP calculations were performed with the same supercell (containing four primitive cells) and having the mean experimental lattice constant described earlier. In contrast to previously published results on similar systems[259], we find only nonbonding interactions at the Fermi level for the Ru-Ru pair in $MnRu_2Sn$ (with a strong antibonding peak *above* the Fermi level). An antibonding peak is present at the Fermi level for the Mn-Ru pair in the NM state of $MnRu_2Sn$, which is not reduced significantly upon spin-polarization. These results are consistent with our estimates of the various j_i in Table 5.3 and let us strengthen our conclusion that Mn-Mn interactions are the dominating force in determining the magnetic configuration of $MnRu_2Sn$.

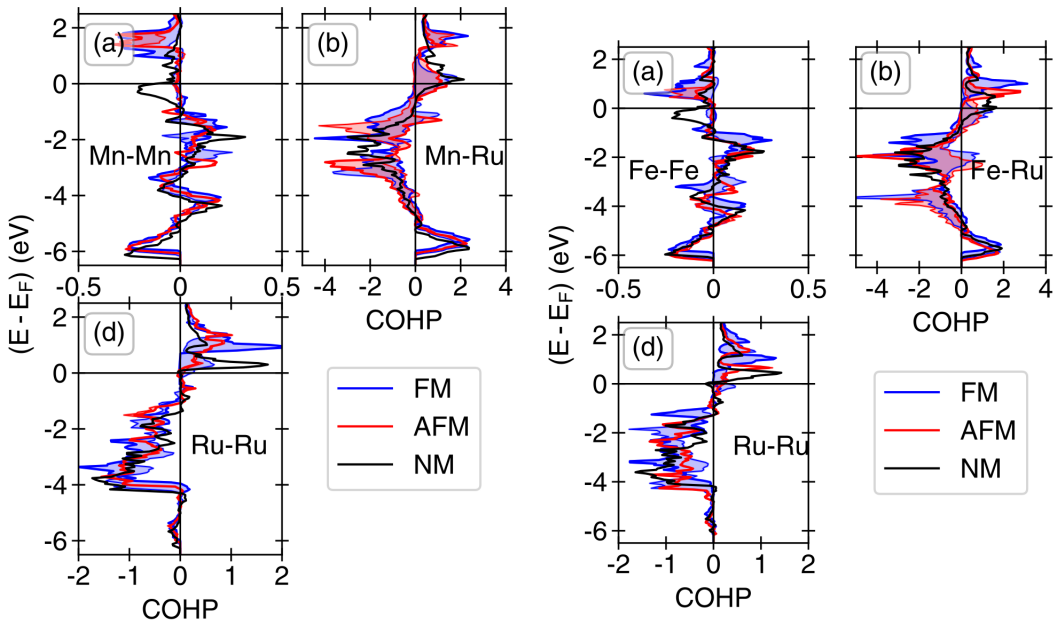

Figure 5.5: COHP bonding analysis for various bonds present in $MnRu_2Sn$ (Left) and $FeRu_2Sn$ (Right) for NM, FM, and AFM configurations. For FM and AFM, the thick line represents the majority spin, while the thin line represents the minority spin.

In $FeRu_2Sn$, the COHP analysis (Figure 5.5, Left) reveals that the Fe-Ru interaction is still anti-bonding at the Fermi level, but not by as much as for the Mn-Ru interaction in $MnRu_2Sn$. For the Ru-Ru pair, spin-polarization turns a bonding interaction into an *anti-bonding* interaction, but the value in both cases is small. For the Fe-Ru pair, spin-splitting allows for an antibonding peak at the Fermi level to shift somewhat more significantly lower in energy than in the Mn-Ru case; this is reflected in the larger j_4 contribution in the Fe-Heusler in Table 5.3. However, none of these results approach the magnitude of changes when going from NM to FM/AFM, as seen in $MnRh_2Ge$ or $MnCo_2Ga$[259],[3].

Overall, our findings imply that magnetism in either the Mn- or the Fe-Heusler is primarily controlled by Mn/Fe-Mn/Fe interactions, with Ru-Fe interactions playing a much smaller secondary role in the Fe-Heusler. Without making a broader statement about all Heuslers, we conclude that a competition between FM-favoring RKKY and AFM-favoring Sn-mediated superexchange determines the magnetic configuration in (Mn/Fe)Ru_2Sn. As a consequence, a reasonable model of magnetism in the disordered Mn/Fe solid solution can be constructed utilizing only the Mn/Fe sublattice, without the need to consider a more complex model that explicitly includes the Ru sublattices. Instead, the Ru moment becomes a dependent variable following the neighboring Fe moments, as the Fe-Ru coupling is several orders of magnitude larger than for Mn-Ru. As the moment on the Sn sites is never larger than 0.001 μ_B, we can also disregard Sn-Mn/Fe contributions. The role of Sn, instead, is to facilitate superexchange via next-nearest-neighboring Mn/Fe sites.

By simplifying to a model dependent only on the properties of the Mn/Fe sublattice, the remaining problem becomes somewhat straightforward: how do Mn and Fe prefer

[3]Ref. [259] reports -COHP per supercell. We report COHP per bond, and so our our results are smaller by a factor of 12 for Mn-Mn, 6 for Rh-Rh, and 8 for Rh-Mn. We have accounted for these in our analysis.

to organize in solution, does anything unexpected happen upon mixing Mn and Fe, and what happens to the d-bands and the Fermi-level occupation in the range of intermediate compositions?

5.4.2 Magnetic and chemical coupling in $Mn_{1-x}Fe_xRu_2Sn$

We considered 193 symmetrically distinct chemical/magnetic configurations on the Mn/Fe sublattice of the full Heusler $Mn_{1-x}Fe_xRu_2Sn$ enumerated in supercells containing up to four copies of the primitive cell (16 total atoms). The calculated formation energies of these structures, referenced against FM $FeRu_2Sn$ and $L1_1$-AFM $MnRu_2Sn$, are shown in Figure 5.6 (a). All formation energies at intermediate compositions x between 0 and 1 are positive, indicating the existence of a chemical miscibility gap at low temperature. In the thermodynamic limit, $Mn_{1-x}Fe_xRu_2Sn$ alloys will, therefore, phase separate into regions that are Mn rich and regions that are Fe rich. At sufficiently high temperatures, a solid solution will become stable in which Mn and Fe are uniformly distributed over the X sublattice of $Mn_{1-x}Fe_xRu_2Sn$, lacking any long-range order. When quenched from such a temperature (*e.g.*, 1173 K as performed by Douglas *et al.*), suggish kinetics can be used to lock in the disordered solid solution.

The absence of long-range order, however, does not mean that the Mn and Fe lack any order at all. Most solid solutions exhibit a substantial degree of short-range order due to strong local energetic interactions that are not completely overwhelmed by entropy. The low energy configurations at intermediate compositions of Figure 5.6 (a) can serve as useful structural models with which to analyze chemical and magnetic interactions in local environments that are representative of the high temperature solid solutions that have been annealed and then quenched. The lowest-energy intermediate-composition phases contain clustered domains of Mn-rich regions next to Fe-rich domains[4].

[4]It is worth noting that, had we enumerated larger supercells, the lowest-energy structures in the

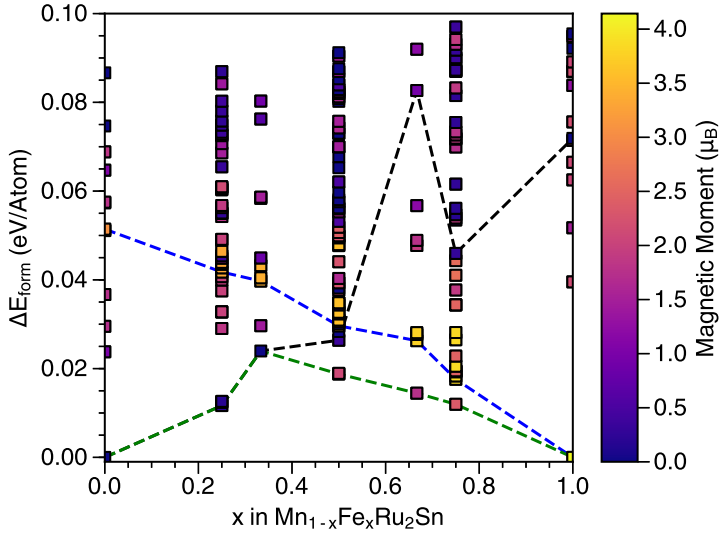

Figure 5.6: Formation energies of the enumerated magnetic and chemical orderings in $Mn_{1-x}Fe_xRu_2Sn$ supercells, colored by the absolute value of the net magnetic moment. The dashed blue and black lines trace the lowest-energy FM ($\mu_B > 3$) and AFM ($\mu_B < 1$) structures, respectively, while the dashed green line joins the overall lowest-energy structures.

In all the structures considered in this study, the per-site magnetic moments for the (Mn,Fe) sites relaxed to values that range from 2.7 to 3.3 μ_B, with lower values at intermediate compositions and higher values for pure Heuslers (Mn,Fe)Ru_2Sn. The magnetic moments on the Ru and Sn sites were universally small, $< 0.7\mu_B$ for Ru and $< 0.022\mu_B$ for Sn. Trends for structures with the lowest (closest to zero) and highest (largest in magnitude) total moments are indicated with the dark dashed lines in Figure 5.6 (a) and show a cross-over at equiatomic composition.

The transition from FM to FrM to AFM is best understood by examining the specific chemical and magnetic configurations of the lowest energy structures as a function of composition. These structures are shown in Figures 5.7(a-g), in order of increasing Fe content. Most striking is the consistency in the ordering: in all cases, variants of the $L1_1$ ordering, consisting of different frequencies of (111) planes that are each chemically and magnetically uniform, were found to have the lowest energy, with Mn-rich regions inducing local AFM behavior. As seen in Figures 5.7e and f, Mn aligns AFM to neighboring

intermediate composition range would asymptotically approach zero. This is a result of the Mn/Fe miscibility gap: larger structures would allow larger and larger volumes of Mn-rich and Fe-rich domains, decreasing the surface-area-to-volume ratio of the interface.

Fe atoms, even when Mn is dilute. These low energy AFM arrangements are facilitated via long-range exchange interactions mediated by the Sn sites. The reverse is not true: in Figure 5.7 (b), the dilute Fe do not induce any local FM ordering in the neighboring Mn planes, resulting in the near-zero net magnetic moments observed at Mn-rich compositions in Figure 5.6 (a). This suggests that in dilute solid solutions the isolated Fe atoms are forced into the AFM configuration favored by the more populous Mn. The price paid for forcing a Mn-dominated structure to accommodate FM behavior is illustrated by the > 10 meV/atom energy difference between two structures at $x_{Fe} = 0.33$ having the same chemical ordering but a different magnetic ordering. These structures are illustrated in Figure 5.7 (c1) and (c2). They differ in the size of their magnetic supercell (three and six unit cells, respectively). In the larger supercell, a smaller fraction of the Mn atoms are forced to participate in FM-like behavior, leading to a lower formation energy.

For each of the low energy chemical configurations, the pure-FM and pure-$L1_1$ AFM magnetic configurations are strictly higher in energy than the FrM magnetic configurations shown in Figures 5.7 (b-f). The energy differences in Table 5.4, normalized per Bohr magneton, demonstrate that transitions to FM configurations are more costly in Mn-dominated structures, while transitions to AFM are more costly in Fe-dominated structures

The calculated magnetic moments in the low energy configurations imply that in a well-mixed disordered solid solution, Fe will remain FM and Mn will remain AFM, yielding the mixed magnetic phase proposed by Douglas *et al.* We can further confirm this assertion by examining how the Mn and Fe *d*-states in the mixed phases compare to the equivalent states of Mn and Fe in the pure Heuslers (Mn,Fe)Ru_2Sn. Figure 5.8 shows a comparison between the site-and-orbital-projected DOS for Mn and Fe in the pure Heuslers Mn- and Fe-projected DOS at each of the intermediate compositions of $Mn_{1-x}Fe_xRu_2Sn$. The DOS of the Mn and Fe sites only change negligibly in the mixed

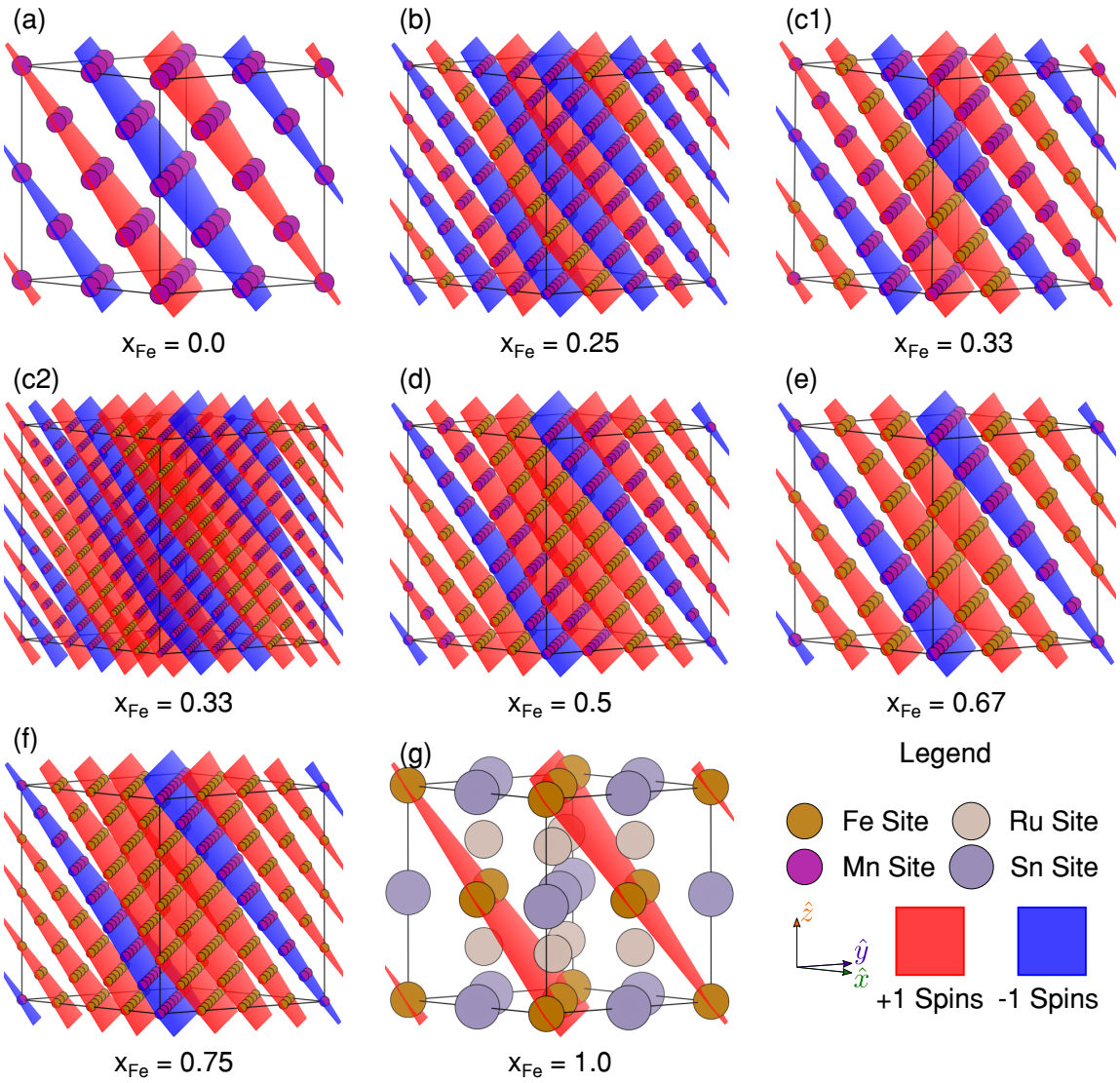

Figure 5.7: The lowest energy chemical and magnetic configurations for $Mn_{1-x}Fe_xRu_2Sn$ for six compositions, showing only the (Mn,Fe)/(Spin Up,Spin Down) sites, except for (g), which shows the full unit cell including Ru and Sn. (c1) and (c2) both represent $x_{Fe} = 0.33$, however, magnetic frustration caused by finite size effects in (c1) results in a significantly larger per-atom energy than the alternate but larger structure (c2). Both chemical and magnetic orderings occur along the [111] direction, creating $L1_1$-like variants across composition space. All visualization were created using the VESTA software package.

phases. This suggests that the Mn and Fe sites behave similarly in the mixed solid solution and in the pure Heuslers (Mn,Fe)Ru_2Sn, and so our analysis of magnetic interactions in Subsection 5.4.1 holds.

Table 5.4: Spin-flip energies in the lowest-energy chemical configurations of $Mn_{1-x}Fe_xRu_2Sn$ as a function of composition, in meV/(μ_B) per primitive cell. The energy differences are calculated as the absolute value of the difference of the energy between the lowest-energy structure at the given x_{Fe}, and the pure FM or AFM variant of that structure, normalized per difference in relaxed magnetic moment and per primitive cell.

x_{Fe}	E_{form}	FrM vs. FM		FrM vs. AFM	
	(meV)	$\Delta\mu_B$ (μ_B)	ΔE (meV/μ_B)	$\Delta\mu_B$ (μ_B)	ΔE (meV/μ_B)
0.25	12.8	3.1	9.4	0[5]	0[a]
0.33	30.1	3.4	8.1	0[a]	0[a]
0.5	18.7	1.5	6.3	2.1	7.2
0.67	15.8	2.0	5.5	1.7	14.7
0.75	12.8	1.5	4.5	2.1	20.0

Our calculated results, combined with the experimental observations of Douglas *et al.*, lead us to a model of isolated magnetic nano-domains of AFM character embedded in a larger FM matrix for Fe concentrations of $0.5 \leq x < 1$. We believe the magnetic hardening can be explained by an exchange-hardening effect, where AFM domains centered on individual Mn atoms or small clusters (< 5 atoms, as no mesoscale ordering is observed experimentally) couple with a single, bulk FM domain carried collectively by the Fe atoms. Such nano-domains would fall below the observation limit of the experimental techniques used to characterize the chemical and magnetic distributions, and offer the simplest phenomenological explanation of the measured magnetic properties.

The Mn and Fe DOS of Figure 5.8 suggest the possibility of half-metallic behavior. Half-metallic behavior is (relatively) common among Heuslers, showing up in multiple members of the $X(Co,Ni,Mn)_2Z$ families of alloys[260–263]. For spintronics, half-metallicity is considered a promising route to achieve the necessary spin-polarized currents. Antiferromagnetic (or rather, fully-compensated ferrimagnetic) half-metals are of particular interest for their net-zero (macroscopic) magnetization, increasing the range

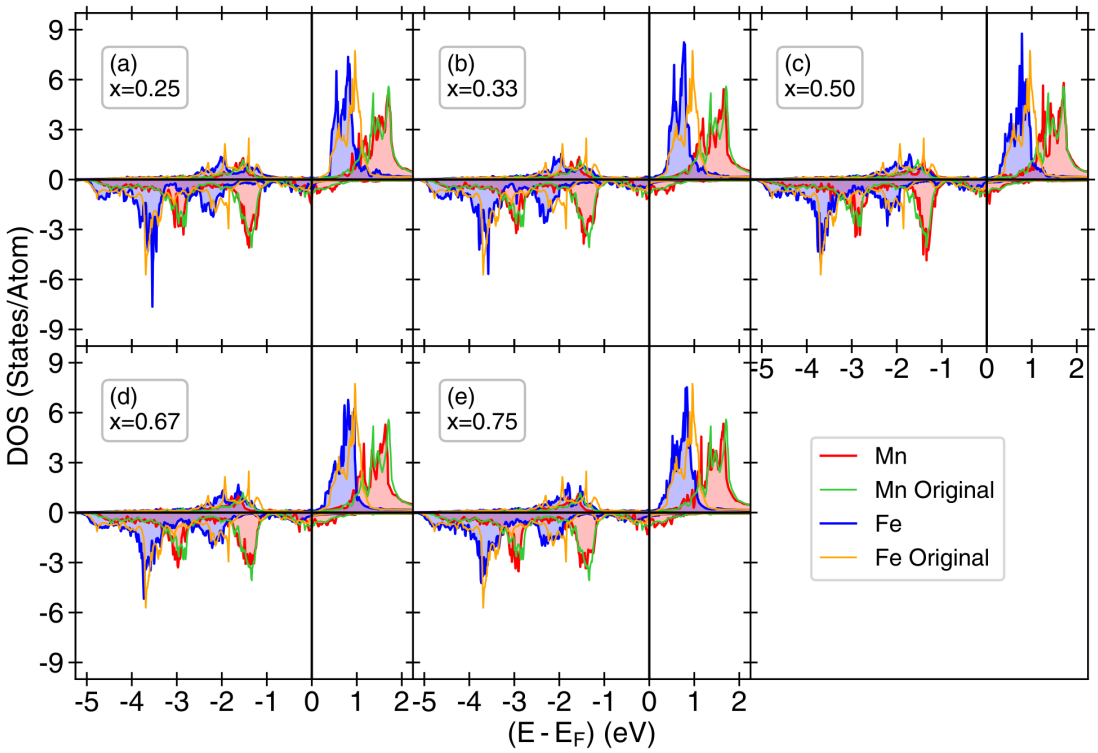

Figure 5.8: Site- and orbital-projected DOS for the d-states of Mn and Fe sites in $Mn_{1-x}Fe_xRu_2Sn$, compared against states of the pure Heuslers (Mn,Fe)Ru_2Sn. Thin green/orange lines indicate d-states from pure Heuslers, while thick red/blue lines with shading indicate the Mn or Fe site-projected DOS from the mixed phase.

of their potential applications[284]. The total DOS for each of the lowest-energy intermediate composition structures is given in Figure 5.9; in no cases is a true gap achieved in either spin channel. Previous *ab-initio* calculations of the electronic properties of $MnRu_2Sn$ indicate a gap in the minority-spin DOS at and around the Fermi level; however, these calculations were performed on the ferromagnetic configuration[262]. As is clear in Figure 5.9 (a), there is no such gap in the AFM ground state[6]. Though other works have performed electronic structure calculations on $FeRu_2Sn$, we are not aware of publications reporting the electronic DOS.

[6]While the choice of functional (*e.g.*, GGA-PBE vs. LDA) is known to influence the *size* of the gap, the choice of functional should not impact whether a gap is observed at all.[285]

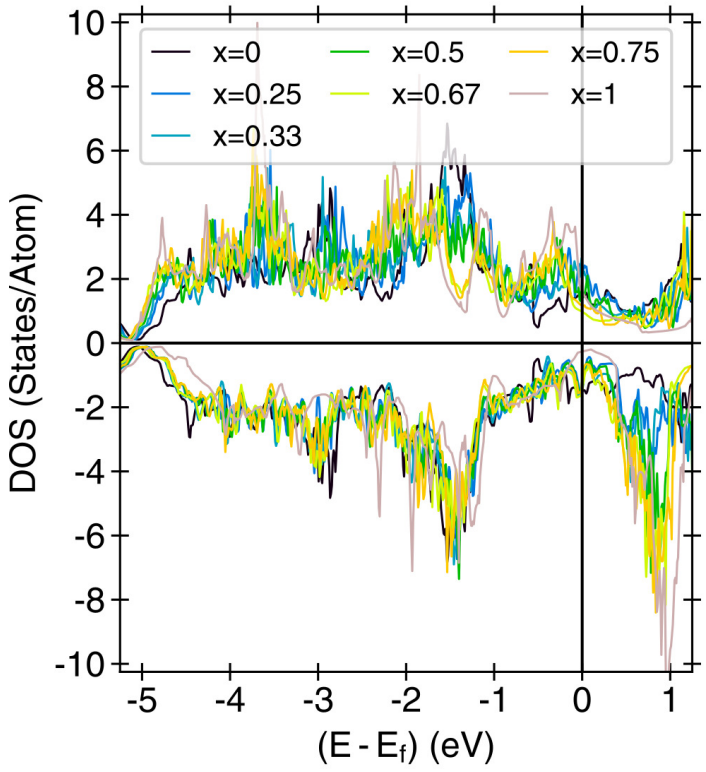

Figure 5.9: Total DOS for various compositions of $Mn_{1-x}Fe_2Ru_2Sn$, showing several "near-gap" occupations in the minority spin channel, but no true half-metals.

5.5 Conclusion

In this Chapter, we have performed a systematic first-principles investigation of both the chemical and magnetic DOFs in the $Mn_{1-x}Fe_xRu_2Sn$ Heusler alloy to determine the origins of exchange hardening in a single phase that is chemically uniform. Careful analysis of the electronic structure of the $MnRu_2Sn$ and $FeRu_2Sn$ end members has shown that magnetic ordering phenomena on the Mn/Fe sub-lattice is determined by a competition between Sn-mediated superexchange, and conduction-electron-mediated RKKY exchange, with Ru serving only to set the lattice constant. Our results demonstrate that the transition from $L1_1$ antiferromagnetic ordering in $MnRu_2Sn$, to ferromagnetic ordering in $FeRu_2Sn$, can be explained by a shifting and narrowing of d-states near the Fermi level. In $MnRu_2Sn$, the Fermi level bisects a d-peak, leaving more states immediately above the Fermi level than below as to favor superexchange, while in $FeRu_2Sn$, the Fermi

level falls immediately after a d-peak, favoring RKKY-type exchange.

The magnetic ordering phenomena of the pure Heuslers (Mn,Fe)Ru_2Sn are not disrupted when Mn and Fe are mixed. First-principles calculations predict that the $Mn_{1-x}Fe_xRu_2Sn$ alloy should phase separate in the thermodynamic limit. Low energy Mn/Fe orderings at intermediate concentrations consist of alternating (111) layers that are chemically and magnetically uniform. The calculated total magnetic moments of the intermediate phases follow the trend of moments measured in quenched solid solutions. An analysis of the density of states of low energy structures confirms that the conclusions for pure Heuslers (Mn,Fe)Ru_2Sn remain valid at intermediate compositions. While several configurations present a near-gap in the minority spin channel, no true half-metals were discovered in $Mn_{1-2x}Fe_xRu_2Sn$.

Chapter 6

A Cluster Expansion Approach to Magnetic Hardening in (Mn,Fe)Ru_2Sn Solid Solutions

> The most that can be expected from any model is that it can supply a useful approximation to reality: All models are wrong; some models are useful
>
> *George Box*, from "Statistics for Experimenters"

This Chapter is the second part of a set, with Chapter 6, exploring the pseudo-binary Heusler (Mn,Fe)Ru_2Sn. Having determined that the magnetic DOF is (1) confined to the (Mn,Fe) lattice site and (2) independent of the moment of the Sn or Ru lattice sites, we construct a Cluster Expansion Hamiltonian to explore the effects of configurational entropy on the magnetic and chemical DOFs. We construct a model capable of exploring

the chemical metastable solid solution, and use that to analyze the interplay between local composition and magnetic ordering phenomena. We find that (1) ferromagnetic behavior dominates the Fe sites, and (2) the Mn sites bifurcate into two populations, one preferring ferromagnetic ordering, and one preferring antiferromagnetic ordering. The preference for the Mn sites comes from the local chemical environment, and the small fluctuations in local composition present in a disordered solid solution.

6.1 Introduction

Heuslers, characterized by four interpenetrating face-centered-cubic (FCC) sub-lattices and a chemical composition of XY_2Z, with X and Y as transition metals and Z as a main-group metal, have attracted renewed attention in the last decade for their unique magnetic properties[48, 53, 254, 255]. Recently, Douglas *et al* demonstrated significant magnetic hysteresis in the pseudo-binary Heusler $Mn_{1-x}Fe_xRu_2Sn$ for $0.25 \leq x \leq 0.75$[44]. Unexpectedly, despite discovering significant evidence for an exchange-hardening-type effect implying two magnetic *and* chemical phases, their results indicate a disordered solid solution on the Mn/Fe sub-lattice and no phase segregation. Traditionally, exchange-hardening arises as a product of two chemical phases, one preferring ferromagnetic (FM) ordering, and one preferring antiferromagnetic (AFM) ordering, existing together in a nanostructured fashion[264, 265]. At the interface between FM and AFM regions, a spin-pinning effect occurs where spins in the AFM phase (which are only perturbed by very large external fields) prevent neighboring spins in the FM phase from being flipped by an external field[286].

$Mn_{1-x}Fe_xRu_2Sn$ and $Mn_{1-x}Fe_xRu_2Ge$ have both demonstrated the rare phenomenon of exchange hardening in a disordered solid solution[44, 262], with neutron diffraction data suggesting a second AFM phase in the bulk FM phase. However, small-angle scattering

experiments were unable to resolve any evidence of a distinct AFM domain, and the AFM-associated peaks disappeared in $Mn_{1-x}Fe_xRu_2Sn$ around 350 K. Both the Sn- and Ge-based Heuslers display a remarkable tunability in the exchange hardening with a change in chemical composition, offering an excellent system to study the phenomenon in a solid solution.

Both experimental studies offered a phenomenologically-driven hypothesis of mictomagnetism to explain the exchange hardening once bulk phase separation was ruled out. A recent *ab-initio* investigation[287] supports this theory via in-depth analysis of the underlying exchange phenomena, but focuses on pure $MnRu_2Sn$ and $FeRu_2Sn$ with only limited analysis of some *ordered* intermediate-composition phases. Neither experimental or *ab-initio* prior work is equipped to fully describe or explain the magnetic ordering behavior present in the chemically-disordered solid solution at finite temperature. To fully explore the micro- and mesoscale magnetic ordering phenomena, we have constructed a coupled chemical-magnetic Cluster Expansion (CE) Hamiltonian[28, 288] suitable for determining ensemble-averaged properties in a disordered solid solution at experimentally-relevant length-scales and temperatures[31, 137, 165].

Our model allows for simultaneous exploration of microscale magnetic ordering and of ensemble-averaged properties not easily accessible via experiment. Using our model, we can demonstrate how magnetic hardening behavior originates from AFM "nano-domains" localized on Mn sites interacting with a bulk FM phase formed by Fe *and* Mn sites. The subtler outcome: that only *some* of the Mn sites organize antiferromagnetically, is surprising, and can only be observed with a stochastic simulation technique. In addition to verifying the experimentally-observed phenomena, we demonstrate that the Mn sites sub-divide into two distinct populations as a bimodal distribution of magnetic order parameter. This sub-division can be linked to minute fluctuations in nearest-neighbor composition that arise in a *disordered* solid solution.

6.2 Methods

Full details on the electronic structure calculations can be found in Section 5; we use these results to fit our CE Hamiltonian. Both the chemical (Mn versus Fe) and magnetic ($\uparrow$ vs $\downarrow$) degrees-of-freedom (DOFs) reside on one FCC sublattice. As previously demonstrated in Chapter 5, while the two Ru sites have a small[44] but finite magnetic moment ($0.1\mu_B \leq \mu_{\mathrm{Ru}} \leq 0.5\mu_B$ dependent on x), this moment is a strictly *dependent* DOF and does not contribute meaningfully to the energy. To construct a set of CEs, 193 symmetrically-distinct magnetic and chemical configurations were enumerated using the CASM[31, 135–137] software package. We expand here on the CE formalism, first described in Section 2.2, to describe our simultaneous use of a magnetic and chemical DOF.

6.2.1 Cluster expansion

To describe both the chemical and magnetic DOFs present in our system, we have employed a CE Hamiltonian employing two per-site DOFs[289]: the site chemistry x_i and moment m_i, both of which can be ± 1. The occupation variable σ_i, traditionally describing a site, is now an occupation vector $\overline{\sigma}_i = [x_i, m_i]$. Any given chemical and magnetic configuration can be described by a microstate vector, $\overline{\sigma}$, and any scalar property of configuration $\overline{\sigma}$ can be expanded in a basis of cluster functions $\phi_\delta^{(\gamma)}(\overline{\sigma})$. The cluster functions have the following form:

$$\phi_\delta^{(\gamma)}(\overline{\sigma}) = \prod_{\substack{i \in \delta \\ \mathbf{J} \in \gamma}} [x_i, 1]\, \mathbf{J} \begin{bmatrix} 1 \\ \\ m_i \end{bmatrix} \tag{6.1}$$

where δ denotes a set of sites, i.e., the cluster's geometry, and γ denotes a set of DOFs, i.e.,

$$\mathbf{J} = \begin{bmatrix} a_i & b_i \\ 0 & c_i \end{bmatrix} \quad \forall \mathbf{J} \in \gamma,$$

where exactly one of (a, b, c) can be 1, and the rest are 0, denoting whether site i contributes its chemical identity ($a = 1$), its magnetic spin ($b = 1$), or both ($c = 1$). Each cluster function $\phi_\delta^{(\gamma)}(\overline{\sigma})$ therefore is defined as a product of the chemical and/or magnetic DOFs of the sites belonging to the cluster.

Many of the $\phi_\delta^{(\gamma)}(\overline{\sigma})$ are related to each other by symmetry operations. We can define a reduced set of cluster geometries α such that an orbit Ω_α contains all δ that map onto α by a symmetry operation of the lattice. If we then color members of the prototype cluster α by the DOFs contributed by each site, chosen by γ, we can define an orbit Ω_β that contains all colored clusters that map back onto a reference colored cluster β, i.e., a combination of geometry and chosen DOFs, by a symmetry operation of the lattice. Any scalar property S of a microstate $\overline{\sigma}$ can then be expressed as:

$$S(\overline{\sigma}) = \sum_\alpha \sum_\beta V_{(\alpha,\beta)} \sum_{\delta \in \Omega_\alpha} \sum_{\gamma \in \Omega_\beta} \phi_\delta^{(\gamma)}. \tag{6.2}$$

Depending on both the scalar property being queried, there are additional symmetries that must be considered if we assume that magnetic configurations related by the time-reversal operator are degenerate (or explicitly anti-degenerate) in the given property[290]. For example, if we consider energy (absent an external magnetic field), we want to ensure that flipping *all* the spins doesn't change the energy, e.g., that $E(\uparrow\uparrow\uparrow) = E(\downarrow\downarrow\downarrow)$. This means that $V_{\alpha,\beta}$ must equal 0 for clusters $\phi_\delta^{(\gamma)}$ that contain an odd number of magnetic terms. Conversely, if we consider the total magnetic moment M of a configuration,

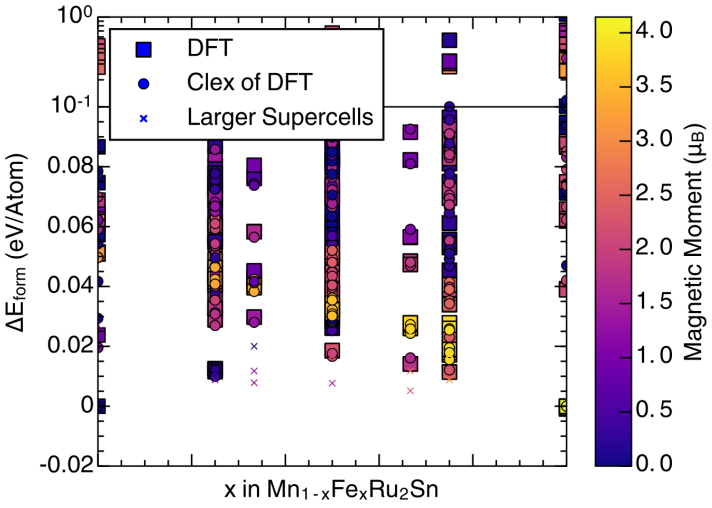

Figure 6.1: Convex hull for (Mn,Fe)Ru_2Sn showing the goodness-of-fit of both formation energy and magnetic moment at different chemical and magnetic configurations at various chemical compositions. The formation energies of larger supercells was also calculated using the CE; entries lying below the miscibility gap correspond to larger block-segregated regions of Mn and Fe, split along the [111] direction.

clusters containing an *even* number of magnetic terms must have $V_{\alpha,\beta} = 0$, as the net moment *must* change sign if we flip all the spins, e.g., $M(\uparrow\uparrow\uparrow) = -M(\downarrow\downarrow\downarrow)$.

6.3 Results

Two CEs were produced for two properties: formation energy per primitive cell, and net magnetic moment per primitive cell. For both expansions, configurations were weighted as $\exp -\Delta E_F/(-0.05\text{eV})$ during the fitting process. Figure 6.1 shows an overlay of predicted versus calculated formation energy and moment. The weighted RMS errors per primitive cell were 2.4 meV for the formation energy and 0.031 μ_B for the magnetic moment, while the CV scores per primitive cell (using shuffled k-fold with 10 folds) were and 2.7 meV and 0.033 μ_B, respectively.

Two types of grand-canonical Monte Carlo (MC) simulations were performed: fully-equilibrated calculations where both DOFs were relaxed during cooling, and metastable calculations where the chemistry was sampled at 1173 K (i.e, the experimental annealing temperature) and then frozen, allowing only the magnetic spins to relax while cooling. In

the latter set of calculations, 100 snapshots[1], taken 1000 passes apart (one pass: successful moves = number of sites), were captured at each chemical potential at 1173 K, cooled, and re-averaged at each temperature to produce an ensemble measurement. All calculations utilized a cubic simulation cell containing 4000 primitive cells, with temperature steps of ±5K. Simulations were considered converged when the energy was converged to within 10 meV/unit cell and the composition converged to within 0.01, using a 95% confidence interval for both measurements[291]. The local chemical and magnetic nearest-neighbor correlations,

$$\phi_2(\overline{\sigma}_i) = \frac{1}{12} \sum_{j \in NN} \begin{bmatrix} x_i \times x_j \\ \\ m_i \times m_j \end{bmatrix} = \begin{bmatrix} \eta_x(i) \\ \\ \eta_m(i) \end{bmatrix}, \tag{6.3}$$

were used as order parameters $\eta_\sigma(i)$ to measure the local chemical and magnetic environments of each MC site (i.e., one with a magnetic/chemical DOF). Positive values correspond to homogeneous/ferromagnetic environments (e.g., a Fe surrounded by Fe, an Up surrounded by Up), negative values correspond to anti-site defects/antiferromagnetic environments (e.g., a Mn surrounded by Fe, a Down surrounded by an Up), and zero values correspond to $L1_1$ ordering of chemistry or magnetism.

Our use of a discrete (e.g., Ising-like) spin variable to represent the magnetic DOF has implications for the observed Curie/Neel temperatures. As compared to continuous DOF (e.g., a vector on a unit sphere, like that in a Heisenberg model), the number of unique microstates (and hence the total possible entropy) is far smaller in a two-state system than a continuous system[292]. As a result, the ordering/disordering temperatures in our system must be scaled by a factor of ≈ 0.31 to match experimental results. This factor of 0.31 comes from the ratio of the Neél/Curie temperatures between a Heisenberg-like mode and an Ising-like model (calculated with identical $V_{\alpha,\beta}$) in the pure $MnRu_2Sn$ and

[1] 100 was chosen as moment and energy varied by $< 1\%$ with increasing numbers of snapshots

$FeRu_2Sn$ Heuslers, shown in Figure 6.2. When approaching zero kelvin the two models converge: the number of relevant microstates collapses towards one, and hence the energy contribution from entropy approaches zero.

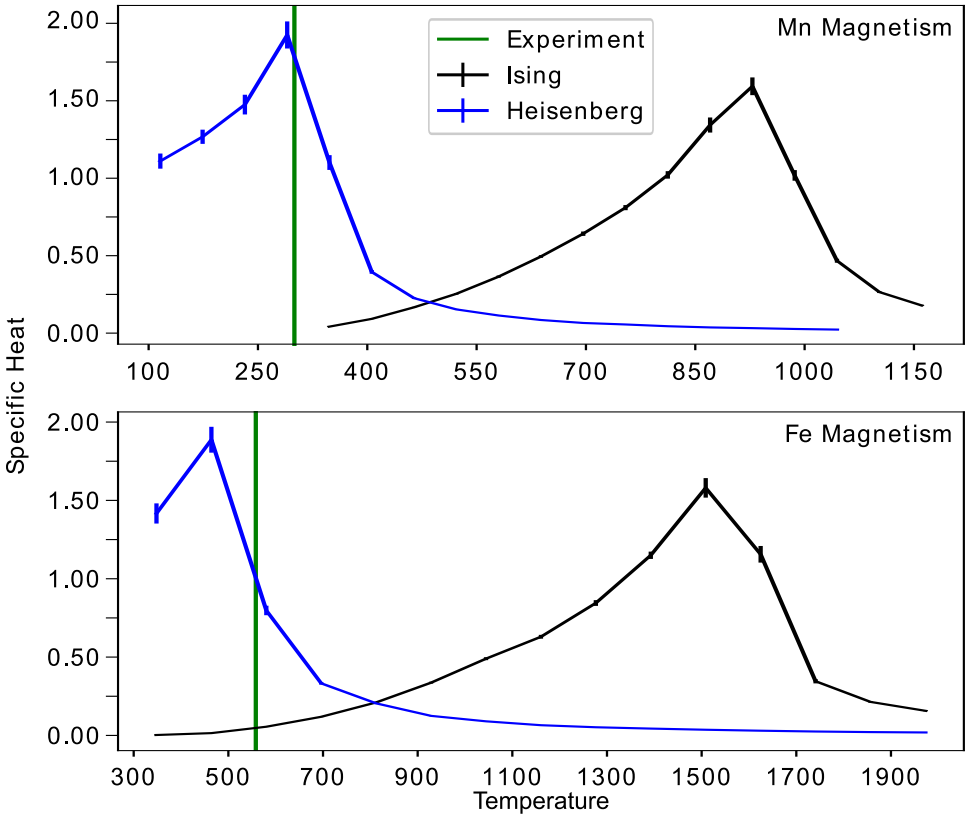

Figure 6.2: Heat capacities (unitless) versus temperature (kelvin) for pure $MnRu_2Sn$ (top) and $FeRu_2Sn$ (bottom).The scaling behavior differs depending on whether a continuous (Heisenberg) or discrete (Ising) DOF is used. A scaling factor of 0.31 brings the two models in agreement for the specific clusters and ECIs used in this study.

Phase diagrams, colored by heat capacity, are shown in Figures 6.3(a) and (b). In Figure 6.3(a), where both chemical and magnetic DOFs were equilibrated, the Néel/Curie temperatures occur above a miscibility gap. Figure 6.3(b) emulates the chemically metastable conditions achieved by Douglas *et al*[44], i.e., a high-temperature annealed sample quenched into a disordered solid solution, then cooled. There is no miscibility gap or chemical phase transition, but there is still a series of magnetic phase transitions. At

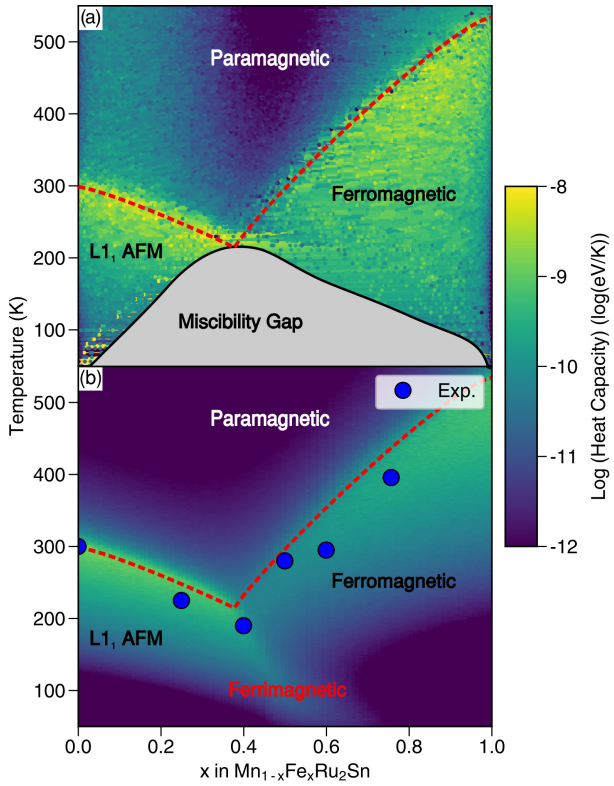

Figure 6.3: Phase diagrams, colored by heat capacity, of (a) the fully-equilibrated system where both magnetic and chemical DOFs were relaxed, and of (b) the metastable system, where the chemistry was frozen at 1173 K but the magnetic spins were allowed to relax to 0 K. A scale factor of 0.31 was applied to the temperatures to account for the use of a discrete DOF for the magnetism. The red, dashed line indicates the NeéL/Curie temperatures estimated from the heat capacity. A second phase transition from a ferromagnetic to ferrimagnetic ordering occurs in the metastable system for $0.4 < x < 0.67$.

$x < 0.4$ and $x > 0.67$ there exists one Neel or Curie temperature, respectively. However, for $0.4 \leq x \leq 0.67$ (where the experimental coercivity significantly increases), two phase transitions occur in series: an initial ferromagnetic ordering, followed by transition to a ferrimagnetic phase.

To understand the short-range ordering behavior of the mixed magnetic phase we tracked the evolution of the magnetic order parameter η_m for all of the Mn- and Fe-occupied sites. Figure 6.4 shows representative low-temperature snapshots of the magnetic configurations for different disordered compositions, colored by magnetic order parameter, while Figures 6.5 shows 2D histograms of η_m and η_x of both species (Mn and Fe) at each composition shown in Figure 6.4, collected across all 100 snapshots per composition. As visible in Figure 6.4, especially panels (a) versus (b), regions of FM ordering emerge with increasing Fe content, eventually forming one large FM domain studded with 1-5 atom AFM "nano-domains". From the corresponding panels in Figure 6.5, we

see that: (1) Fe atoms with a Fe neighbor form FM domains of increasing size with increasing Fe content, and (2) Above a critical Fe concentration, the Mn population splits into FM-favoring Mn and AFM-favoring AFM, dependent on the local environment of the Mn atom in question.

Comparison with Experiment

Powder x-ray diffraction data, simulated using RIETAN-FP[293] and shown in Figure 6.6(a), demonstrates the lack of chemical order present in the snapshots taken at 1173 K. All of the visible peaks can be accounted for in the diffraction spectrum of the generic Heusler lattice. While the Mn and Fe are randomly distributed on the (Mn,Fe) sublattice, within that random distribution some Mn will have more or fewer Mn neighbors than others (and similarly, for Fe). These fluctuations in local neighborhood, while not contributing to any short- or long-range chemical order, are still sufficient to change

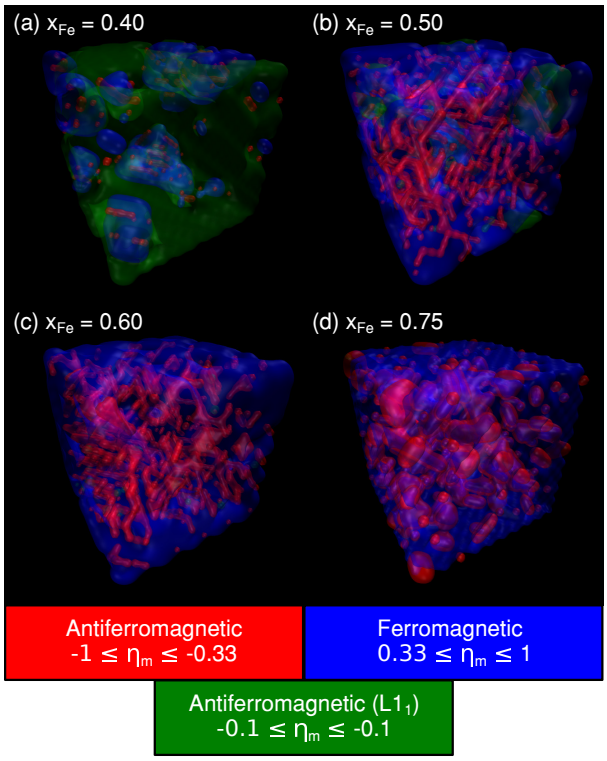

Figure 6.4: Snapshots of short-range magnetic orderings in chemically-disordered $Mn_{1-x}Fe_xRu_2Sn$ Heuslers, colored by local magnetic order parameter. Snapshots at $x = 0.25$ are not shown, as in all cases the magnetic configuration is completely $L1_1$ AFM (i.e., it would be a solid green cube).

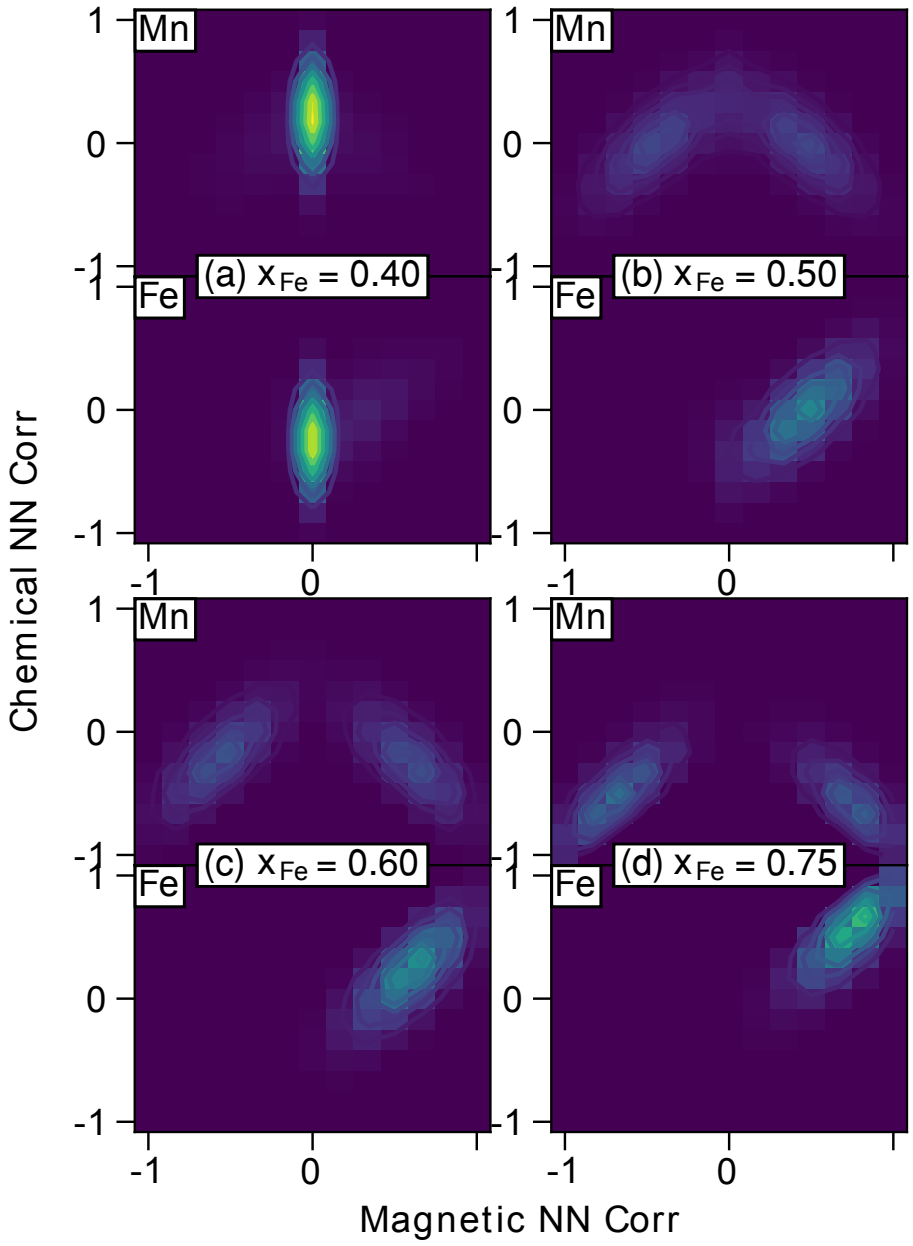

Figure 6.5: 2D histograms of the per-species collected η_x and η_m for all Mn and all Fe sites at each collection of 100 snapshots at selected compositions. Negative values of either order parameter indicates a strongly antiferromagnetic/heterogeneous environment (e.g., $[\downarrow,\uparrow,\downarrow]$ or [Fe,Mn,Fe]), while positive values indicate a ferromagnetic/homogeneous environment (e.g., $[\uparrow,\uparrow,\uparrow]$ or [Fe,Fe,Fe]; $\eta_m = 0$ corresponds to the $L1_1$ AFM ordering.

the magnetic preference of a Mn or Fe site.

The low-temperature mean magnetic moment resulting from our MC simulations,

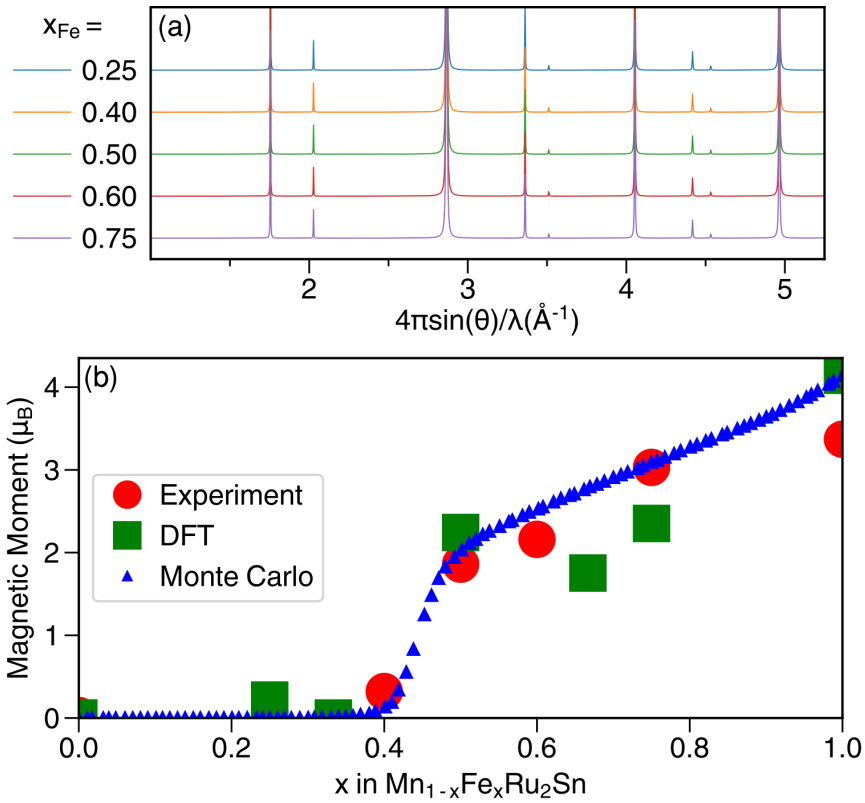

Figure 6.6: (a) Simulated powder diffraction patterns of chemical orderings at selected compositions. All visible peaks originate from the Heusler lattice; no (Mn,Fe) sublattice ordering is present. (b) Low-temperature magnetism, compared between experiment (at 4 K and in a field of 5T), DFT (at 0 K and no field), and the MC simulations carried out here (at 5 K and no field).

compared against both DFT calculations of low-energy ordered structures at 0 K and against experimental measurements made at 4 K and in a field of 5T, can be seen in Figure 6.6(b). The DFT and MC calculations overestimate the magnetic moment at Fe-rich compositions because of multicrystallinity and imperfectly-aligned magnetic domains present in the experimental sample. Most notable in the results is the progression from L11 AFM-dominated behavior to ferrimagnetic behavior to predominantly FM behavior with increasing Fe-content.

The moment is not fully saturated at $x = 0.75$ as some portion of the sparse Mn-sites are still antiferromagnetically aligned, seen in Figure 6.4 (d). At $x = 0.25$, however, the

moment is uniformly zero, as the sparse Fe sites relax into the $L1_1$ antiferromagnetic configuration. At $x = 0.40$ where the coercivity is the greatest but the moment is very small, we can see in Figure 6.4 (a) that some small number of FM domains (themselves containing tiny AFM centers) manage to form, and have a large $L1_1$ AFM phase to couple to. Overall, our results quantitatively and qualitatively match those from experiment, while snapshots let us visually verify our hypothesis of antiferromagnetic Mn-centered "nano-domains" leading to exchange-hardening behavior.

6.4 Conclusion

Our analysis demonstrates that antiferromagnetic Mn-centered nano-domains exist within bulk ferromagnetic domains present in (Mn,Fe)Ru_2Sn Heusler alloys. Despite complete chemical disorder on the (Mn,Fe) sublattice, there effectively exists two magnetic phases at low temperatures and compositions of $x > 0.25$, giving rise to the large coercivities observed experimentally. These nano-domains are the result of extremely slight fluctuations in local environment leading to Mn nano-clusters of 5 or fewer atoms; far too small to be observed using traditional experimental techniques. In this Chapter, we have constructed a pair of coupled chemical-magnetic CEs and used them to explore the unique magnetic behavior of $Mn_{1-x}Fe_xRu_2Sn$. Our analysis, building upon a solid foundation of experimental work, allows for a richer and more-complete landscape of this Heusler to be explored than either technique alone.

Chapter 7

Conclusion

Transition metal alloys, especially those with magnetic properties, offer great promise in domains of future technological interest. However, the combinatorial space of alloys encompasses a domain far too large to be explored by traditional experimental methods[1], especially as ternaries, quaternaries, and quinaries become the focuses of innovation. *Ab-initio* methods, especially Density Functional Theory (DFT), offer a new approach to querying the expensive parameter space of yet-undiscovered alloys. As many promising materials themselves have applications in computing, the *ab-initio* driven materials discovery process forms a positive feedback cycle, providing more advanced computers capable of simulating alloys previously unimaginable by man or machine. Through theory and simulation we can now not only replicate the phenomena observed in complex alloys systems, but now predict the behaviors of materials not yet made, and measure properties otherwise unobservable through classical interrogation techniques.

The overarching theme of this thesis was to develop a better understanding of transition metal alloys through an *ab-initio* framework, and to improve our ability to simulate said alloys. We have presented two strongly-contrasting tales of DFT applied to tran-

[1] i.e., "shake and bake" metallurgy[294]

sition metals: one a failure, and one a success. The common elements are d electrons, magnetism, and the use of a Cluster Expansion (CE) Hamiltonian to understand the finite-temperature implications of the electronic structure calculations. In both cases we have gained new insights into the fundamental physics underpinning the alloys in question and explored the important contributions of configurational entropy. Sandwiched in-between these two stories is a description of an alternate path to a CE Hamiltonian, one utilizing experimental measurements rather than *ab-initio* calculations. Via this new approach, we offer a new approach to examining alloy physics, starting with the free energy and then stripping away the configurational entropy. Our new technique offers a means of verifying the accuracy of *ab-initio* calculations, and a new route to alloy thermodynamics when said calculations prove unreliable or too expensive. Together, these three projects represent incremental but important steps in improving our ability to *accurately* simulate yet-undiscovered alloys.

Studying the Co-Pt binary, we verified a previously hinted-at failure case of the popular functional PBE. By using a CE Hamiltonian and Monte Carlo (MC) simulations, we provided a thermodynamic connection between zero kelvin electronic structure calculations and high-temperature experimental measurements. Our results proved that neither configurational nor vibrational entropy could neither account for the differences in formation energy, nor the unusual set of ground states predicted. We explored the assumptions and approximations made in common functionals used in DFT, and those assumptions lead to serious problems in the case of simulating alloys in the Co-Pt system.

These problems were not limited to Co-Pt alone, and instead extended to numerous other alloy systems. These systemic failings motivated us to determine a means by which a CE Hamiltonian could be constructed *without ab-initio* simulations. By considering the cluster functions and their energy coefficients themselves as pairs of thermodynamic variables, we determined a relationship between measurable ensemble averages and the

energy coefficients that would allow us to parameterize a Hamiltonian from experimental data. To bypass the known sparsity problem of CE Hamiltonians, we then utilized an entropy-maximization approach to selecting the *correct* set of clusters to include in a Hamiltonian. We demonstrated our approach on a variety of model systems, proving that our technique can reconstruct full phase diagrams from only high-temperature measurements of the disordered solid solution of an alloy.

Though transition metals can pose unusual challenges to the methods presently available in DFT, there are many successes. Despite (or perhaps in spite of) our earlier troubles in the Co-Pt system, we simulated and characterized the chemical and magnetic ordering phenomena in the (Mn,Fe)Ru_2Sn pseudo-binary Heusler system using DFT and a CE Hamiltonian within MC simulations. From the electronic structure calculations, we determined the origin of magnetic behavior in both $MnRu_2Sn$ and $FeRu_2Sn$, and explored why the simple addition/subtraction of one electron and proton transformed the system from ferromagnetic to L11 antiferromagnetic order, accompanied by a large change in the magnetic ordering temperature. Having sampled a large space of chemical and magnetic configurations, we constructed a CE Hamiltonian utilizing both degrees-of-freedom, and parameterized it from our *ab-initio* simulations. Using MC simulations designed to emulate the annealing and quenching critical to synthesis of the metastable disordered solid solution, we were able to determine the origin of the anomalous exchange-hardening observed experimentally.

Ab-initio simulations improve every year, both with the development of better approximations to the true all-electron physics, and with the development of more powerful computers capable of solving larger, harder problems. The techniques we have utilized — DFT calculations and CE Hamiltonians — are growing both more commonplace and more powerful. Projects involving thousands of electronic structure calculations are now routine; exploring the parameter space of ternaries, quaternaries, and quinaries is a matter

of patience rather than impossibility. A new focus on verification, validation, and uncertainty quantification has arisen in the materials science community. High-throughput techniques, both experimental and *ab-initio*, are revolutionizing research. The work put forward in this thesis is only a sliver of the progress being made, but it is important. We have drawn attention to a previously overlooked categorical failure of commonly-used techniques. We have offered a new approach to utilizing a powerful thermodynamic tool. And we have demonstrated the success possible when both techniques — DFT and CE Hamiltonians — are at their peak.

Bibliography

[1] E. Schrödinger *Phys. Rev.* **28** (1926) 1049–1070, [arXiv:1112.5320].

[2] P. A. Dirac *R. Soc.* **117** (1928), no. 778 610–624.

[3] *Computing and the Manhattan Project*, 2014.

[4] K. H. Johnson *J. Chem. Phys.* **45** (1966) 3085–3095.

[5] W. Kohn and L. J. Sham *Phys. Rev.* **140** (1965) A1133–A1138, [PhysRev.140.A1133].

[6] W. Hohenberg, P.; Kohn *Phys. Rev.* **136** (1964) B864–B871, [arXiv:1108.5632].

[7] D. R. Hartree *Math. Proc. Cambridge Philos. Soc.* **24** (1928) 89.

[8] D. R. Hartree *Math. Proc. Cambridge Philos. Soc.* **24** (1928) 111.

[9] J. C. Slater *Phys. Rev.* **34** (1929) 1293–1322, [PhysRev.34.1293].

[10] V. Fock *Zeitschrift fr Phys.* **61** (1930) 126–148.

[11] L. H. Thomas *Math. Proc. Cambridge Philos. Soc.* **23** (1927) 542–548.

[12] E. Fermi *Rend. Accad. Naz. Lincei* **6** (1927) 602–607.

[13] J. C. Slater *Phys. Rev.* **81** (1951) 385–390.

[14] V. Heine, *European Collaboration in Ab-Initio Computer Simulation*, tech. rep., 2002.

[15] C. Corminboeuf, F. Tran, and J. Weber *J. Mol. Struct. THEOCHEM* **762** (2006) 1–7.

[16] D. M. Ceperley and B. J. Alder *Phys. Rev. Lett.* **45** (1980) 566–569, [0201087].

[17] J. P. Perdew, J. A. Chevary, S. H. Vosko, K. A. Jackson, M. R. Pederson, D. J. Singh, and C. Fiolhais *Phys. Rev. B* **46** (1992) 6671–6687.

[18] J. P. Perdew, J. A. Chevary, S. H. Vosko, K. A. Jackson, M. R. Pederson, D. J. Singh, and C. Fiolhais *Phys. Rev. B* **46** (1992) 6671–6687.

[19] M. J. Frisch, G. W. Trucks, H. B. Schlegel, G. E. Scuseria, M. A. Robb, J. R. Cheeseman, G. Scalmani, V. Barone, G. A. Petersson, H. Nakatsuji, X. Li, M. Caricato, A. V. Marenich, J. Bloino, B. G. Janesko, R. Gomperts, B. Mennucci, H. P. Hratchian, J. V. Ortiz, A. F. Izmaylov, J. L. Sonnenberg, D. Williams-Young, F. Ding, F. Lipparini, F. Egidi, J. Goings, B. Peng, A. Petrone, T. Henderson, D. Ranasinghe, V. G. Zakrzewski, J. Gao, N. Rega, G. Zheng, W. Liang, M. Hada, M. Ehara, K. Toyota, R. Fukuda, J. Hasegawa, M. Ishida, T. Nakajima, Y. Honda, O. Kitao, H. Nakai, T. Vreven, K. Throssell, J. A. Montgomery, {Jr.}, J. E. Peralta, F. Ogliaro, M. J. Bearpark, J. J. Heyd, E. N. Brothers, K. N. Kudin, V. N. Staroverov, T. A. Keith, R. Kobayashi, J. Normand, K. Raghavachari, A. P. Rendell, J. C. Burant, S. S. Iyengar, J. Tomasi, M. Cossi, J. M. Millam, M. Klene, C. Adamo, R. Cammi, J. W. Ochterski, R. L. Martin, K. Morokuma, O. Farkas, J. B. Foresman, and D. J. Fox, *Gaussian16 {R}evision {A}.03*, 2016.

[20] G. Kresse and J. Furthmüller *Comput. Mater. Sci.* **6** (1996) 15, [0927-0256(96)00008].

[21] G. Kresse and J. Hafner *Phys. Rev. B* **47** (1993) 558–561, [0927-0256(96)00008].

[22] G. Kresse and J. Hafner *Phys. Rev. B Condens. Matter Mater. Phys.* **49** (1994), no. 20 14251–14269.

[23] R. O. Jones *Rev. Mod. Phys.* **87** (2015) 897–923, [1412.8405].

[24] K. Burke *J. Chem. Phys.* **136** (2012) 150901, [1201.3679].

[25] P. C. Hohenberg, W. Kohn, and L. J. Sham *Adv. Quantum Chem.* **21** (1990), no. C 7–26.

[26] B. B. Laird, R. B. Ross, and T. Ziegler *Symp. A Q. J. Mod. Foreign Lit.* (1996) 1–17.

[27] W. Kohn, *Walter Kohn - Biographical*, 1998.

[28] J. M. Sanchez, F. Ducastelle, and D. Gratias *Phys. A Stat. Mech. its Appl.* **128** (1984) 334–350.

[29] D. D. Fontaine *Solid State Phys. - Adv. Res. Appl.* **47** (1994), no. C 33–176.

[30] J. M. Sanchez *Phys. Rev. B* **48** (1993) 14013–14015.

[31] B. Puchala and A. Van der Ven *Phys. Rev. B Condens. Matter Mater. Phys.* **88** (2013) 094108.

[32] E. Decolvenaere, M. J. Gordon, and A. Van der Ven *Phys. Rev. B* **92** (2015) 085119, [arXiv:1508.0273].

[33] A. A. Belak and A. Van der Ven *Phys. Rev. B* **91** (2015) 224109.

[34] A. R. Natarajan, E. L. Solomon, B. Puchala, E. A. Marquis, and A. Van der Ven *Acta Mater.* **108** (2016) 367–379.

[35] A. E. Mattsson, P. A. Schultz, M. P. Desjarlais, T. R. Mattsson, and K. Leung *Model. Simul. Mater. Sci. Eng.* **13** (2005) R1–R31.

[36] A. J. Cohen, P. Mori-Sánchez, W. Yang, W. Y. P. Mori-Sánchez, P. Mori-Sánchez, and W. Yang *Science (80-.).* **321** (2008) 792–4.

[37] C. J. Cramer and D. G. Truhlar *Phys. Chem. Chem. Phys.* **11** (2009) 10757–10816.

[38] A. E. Mattsson and J. M. Wills *Int. J. Quantum Chem.* **116** (2016) 834–846.

[39] J. H. Perepezko *Science (80-.).* **326** (2009), no. 5956 1068–1069.

[40] C. M. F. Rae *Mater. Sci. Technol.* **25** (2009) 479–487.

[41] T. E. Jones, M. E. Eberhart, S. Imlay, C. MacKey, and G. B. Olson *Phys. Rev. Lett.* **109** (2012) 125506.

[42] M. C. Troparevsky, J. R. Morris, P. R. C. Kent, A. R. Lupini, and G. M. Stocks *Phys. Rev. X* **5** (2015) 011041.

[43] J. W. Yeh, S. K. Chen, S. J. Lin, J. Y. Gan, T. S. Chin, T. T. Shun, C. H. Tsau, and S. Y. Chang *Adv. Eng. Mater.* **6** (2004) 299–303+274.

[44] J. E. Douglas, E. E. Levin, T. M. Pollock, J. C. Castillo, P. Adler, C. Felser, S. Krämer, K. L. Page, and R. Seshadri *Phys. Rev. B* **94** (2016) 094412.

[45] O. Gutfleisch, M. A. Willard, E. Brück, C. H. Chen, S. G. Sankar, and J. P. Liu *Adv. Mater.* **23** (2011) 821–842.

[46] S. Mizusaki, A. Douzono, T. Ohnishi, T. C. Ozawa, H. Samata, Y. Noro, and Y. Nagata *J. Alloys Compd.* **510** (2011) 141–146.

[47] J. D. Bocarsly, E. E. Levin, C. A. Garcia, K. Schwennicke, S. D. Wilson, and R. Seshadri *Chem. Mater.* **29** (2017) 1613–1622.

[48] T. Graf, S. S. P. Parkin, and C. Felser *IEEE Trans. Magn.* **47** (2011) 367–373.

[49] M. Meinert, J.-M. Schmalhorst, and G. Reiss *J. Phys. Condens. Matter* **23** (2011) 36001.

[50] J. Ma, V. I. Hegde, K. Munira, Y. Xie, S. Keshavarz, D. T. Mildebrath, C. Wolverton, A. W. Ghosh, and W. H. Butler *Phys. Rev. B* **95** (2017) 024411.

[51] L. Bainsla and K. G. Suresh *Appl. Phys. Rev.* **3** (2016) 031101.

[52] M. Siewert, M. E. Gruner, A. Dannenberg, A. Chakrabarti, H. C. Herper, M. Wuttig, S. R. Barman, S. Singh, A. Al-Zubi, T. Hickel, J. Neugebauer, M. Gillessen, R. Dronskowski, and P. Entel *Appl. Phys. Lett.* **99** (2011) 191904.

[53] A. Planes, L. Mañosa, and M. Acet *J. Phys. Condens. Matter* **21** (2009) 1–29.

[54] S. Bhattacharya and G. K. H. Madsen *Phys. Rev. B* **92** (2015) 085205.

[55] M. W. Gaultois, T. D. Sparks, C. K. H. Borg, R. Seshadri, W. D. Bonificio, and D. R. Clarke *Chem. Mater.* **25** (2013) 2911–2920.

[56] G. L. W. Hart, S. Curtarolo, T. B. Massalski, and O. Levy *Phys. Rev. X* **3** (2014) 041035.

[57] S. Curtarolo, G. L. W. Hart, M. B. Nardelli, N. Mingo, S. Sanvito, and O. Levy *Nat. Mater.* **12** (2013) 191–201.

[58] Y. Mishin, M. Asta, and J. Li *Acta Mater.* **58** (2010), no. 4 1117–1151.

[59] M. Jahnátek, O. Levy, G. L. W. Hart, L. J. Nelson, R. V. Chepulskii, J. Xue, and S. Curtarolo *Phys. Rev. B Condens. Matter Mater. Phys.* **84** (2011) 214110.

[60] C. Wang, J. Meyer, N. Teichert, A. Auge, E. Rausch, B. Balke, A. Hütten, G. H. Fecher, and C. Felser *J. Vac. Sci. Technol. B Microelectron. Nanom. Struct.* **32** (2014) 020802.

[61] R. Roy *Phys. Rev. B* **79** (2009) 195322, [0607531].

[62] M. Müller, P. Erhart, and K. Albe *J. Phys. Condens. Matter* **19** (2007) 326220.

[63] M. Militzer *Curr. Opin. Solid State Mater. Sci.* **15** (2011), no. 3 106–115.

[64] M. Militzer, J. J. Hoyt, N. Provatas, J. Rottler, C. W. Sinclair, and H. S. Zurob *JOM* **66** (2014) 740–746.

[65] X. Zhang, T. Hickel, J. Rogal, S. Fähler, R. Drautz, and J. Neugebauer *Acta Mater.* **99** (2015) 281–289.

[66] E. Decolvenaere, M. J. Gordon, and A. Van der Ven arXiv:1609.0717.

[67] C. E. Shannon *Bell Syst. Tech. J.* **27** (1948) 379–423, [9411012].

[68] E. T. Jaynes *Phys. Rev.* **106** (1957) 620–630.

[69] E. T. Jaynes *Phys. Rev.* **108** (1957) 171–190, [1011.1669].

[70] E. T. Jaynes *IEEE Trans. Syst. Sci. Cybern.* **4** (1968), no. 3 227–241.

[71] E. T. Jaynes *Proc. IEEE* **70** (1982), no. 9 939–952.

[72] E. T. Jaynes, *The Relation of Bayesian and Maximum Entropy Methods*, 1988.

[73] T. W. Anderson and L. A. Goodman *Ann. Math. Stat.* **28** (1957) 89–110.

[74] W. K. Hastings *Biometrika* **57** (1970), no. 1 97–109.

[75] N. Metropolis, A. W. Rosenbluth, M. N. Rosenbluth, A. H. Teller, and E. Teller *J. Chem. Phys.* **21** (1953) 1087–1092, [5744249209].

[76] M. Born and R. Oppenheimer *Ann. Phys.* **389** (1927), no. 20 457–484, [arXiv:1206.4239].

[77] E. Teller *Rev. Mod. Phys.* **34** (1962) 627–631, [1011.1669].

[78] W. Heisenberg *Zeitschrift fr Phys.* **38** (1926) 411–426.

[79] P. A. M. Dirac *Proc. R. Soc. London. Ser. A* **112** (1926), no. 762 661–677.

[80] A. E. Mattsson *Science (80-.).* **298** (2002) 759–760.

[81] J. P. Perdew and K. Schmidt *AIP Conf. Proc.* **577** (2001) 1–20.

[82] A. I. Liechtenstein, V. I. Anisimov, and J. Zaanen *Phys. Rev. B* **52** (1995) R5467–R5470.

[83] V. I. Anisimov, J. Zaanen, and O. K. Andersen *Phys. Rev. B Condens. Matter Mater. Phys.* **44** (1991) 943–954.

[84] S. L. Dudarev, S. Y. Savrasov, C. J. Humphreys, and A. P. Sutton *Phys. Rev. B* **57** (1998) 1505–1509.

[85] V. I. Anisimov, F. Aryasetiawan, and A. I. Lichtenstein *J. Phys. Condens. Matter* **9** (1999) 767–808.

[86] B. Himmetoglu, A. Floris, S. De Gironcoli, and M. Cococcioni *Int. J. Quantum Chem.* **114** (2014) 14–49, [1309.3355].

[87] R. Armiento and A. E. Mattsson *Phys. Rev. B Condens. Matter Mater. Phys.* **72** (2005) 085108.

[88] A. E. Mattsson and R. Armiento *Int. J. Quantum Chem.* **110** (2010) 2274–2282.

[89] J. P. Perdew, K. Burke, and M. Ernzerhof *Phys. Rev. Lett.* **77** (1996) 3865–3868.

[90] A. Jain, S. P. Ong, G. Hautier, W. Chen, W. D. Richards, S. Dacek, S. Cholia, D. Gunter, D. Skinner, G. Ceder, and K. A. Persson *APL Mater.* **1** (2013) 011002.

[91] S. Curtarolo, W. Setyawan, S. Wang, J. Xue, K. Yang, R. H. Taylor, L. J. Nelson, G. L. W. Hart, S. Sanvito, M. Buongiorno-Nardelli, N. Mingo, and O. Levy *Comput. Mater. Sci.* **58** (2012) 227–235.

[92] J. E. Saal, S. Kirklin, M. Aykol, B. Meredig, and C. Wolverton *JOM* **65** (2013) 1501–1509.

[93] N. W. Ashcroft and N. D. Mermin *Solid. State. Electron.* **9** (1976), no. 10 939–942, [1011.1669].

[94] P. Schwerdtfeger *ChemPhysChem* **12** (2011) 3143–3155.

[95] D. Hamann, M. Schlüter, and C. Chiang *Phys. Rev. Lett.* **43** (1979) 1494–1497, [1011.1669].

[96] G. B. Bachelet, D. R. Hamann, and M. Schlüter *Phys. Rev. B* **26** (1982) 4199–4228.

[97] D. Vanderbilt *Phys. Rev. B* **41** (1990) 7892–7895, [1011.1669].

[98] P. E. Blöchl *Phys. Rev. B Condens. Matter Mater. Phys.* **50** (1994) 17953–17979.

[99] P. Janthon, S. A. Luo, S. M. Kozlov, F. Viñes, J. Limtrakul, D. G. Truhlar, F. Illas, F. Vi??es, J. Limtrakul, D. G. Truhlar, and F. Illas *J. Chem. Theory Comput.* **10** (2014) 3832–3839.

[100] R. Peverati and D. G. Truhlar *Phys. Chem. Chem. Phys.* **14** (2012) 16187–91.

[101] V. Stevanović, S. Lany, X. Zhang, and A. Zunger *Phys. Rev. B Condens. Matter Mater. Phys.* **85** (2012) 115104.

[102] T. M. Henderson, J. Paier, and G. E. Scuseria *Phys. Status Solidi B Basic Res.* **248** (2011) 767–774.

[103] G. I. Csonka, J. P. Perdew, A. Ruzsinszky, P. H. T. Philipsen, S. Lebègue, J. Paier, O. A. Vydrov, and J. G. Ángyán *Phys. Rev. B* **79** (2009) 155107.

[104] P. Haas, F. Tran, and P. Blaha *Phys. Rev. B Condens. Matter Mater. Phys.* **79** (2009) 085104.

[105] J. P. Perdew, A. Ruzsinszky, G. I. Csonka, L. A. Constantin, and J. Sun *Phys. Rev. Lett.* **103** (2009) 026403.

[106] J. Paier, M. Marsman, K. Hummer, G. Kresse, I. C. Gerber, and J. G. Angyán *J. Chem. Phys.* **124** (2006) 154709.

[107] J. N. Harvey *Annu. Reports Sect. "C" (Physical Chem.* **102** (2006), no. 0 203.

[108] F. Furche and J. P. Perdew *J. Chem. Phys.* **124** (2006) 044103.

[109] K. Lejaeghere, G. Bihlmayer, T. Björkman, P. Blaha, S. Blügel, V. Blum, D. Caliste, I. E. Castelli, S. J. Clark, A. Dal Corso, S. de Gironcoli, T. Deutsch, J. K. Dewhurst, I. Di Marco, C. Draxl, M. Dułak, O. Eriksson, J. A. Flores-Livas, K. F. Garrity, L. Genovese, P. Giannozzi, M. Giantomassi, S. Goedecker, X. Gonze, O. Grånäs, E. K. U. Gross, A. Gulans, F. Gygi, D. R. Hamann, P. J. Hasnip, N. A. W. Holzwarth, D. Iuan, D. B. Jochym, F. Jollet, D. Jones, G. Kresse, K. Koepernik, E. Küçükbenli, Y. O. Kvashnin, I. L. M. Locht, S. Lubeck, M. Marsman, N. Marzari, U. Nitzsche, L. Nordström, T. Ozaki, L. Paulatto, C. J. Pickard, W. Poelmans, M. I. J. Probert, K. Refson, M. Richter, G.-M. Rignanese, S. Saha, M. Scheffler, M. Schlipf, K. Schwarz, S. Sharma, F. Tavazza, P. Thunström, A. Tkatchenko, M. Torrent, D. Vanderbilt, M. J. van Setten, V. Van Speybroeck, J. M. Wills, J. R. Yates, G.-X. Zhang, and S. Cottenier *Science (80-.).* **351** (2016), no. 6280 aad3000.

[110] W. Gordon *Zeitschrift fr Phys.* **50** (1928) 630–632.

[111] G. Pilania, C. Wang, X. Jiang, S. Rajasekaran, and R. Ramprasad *Sci. Rep.* **3** (2013) 2810.

[112] K. Hansen, G. Montavon, F. Biegler, S. Fazli, M. Rupp, M. Scheffler, O. A. Von Lilienfeld, A. Tkatchenko, and K. R. M??ller *J. Chem. Theory Comput.* **9** (2013) 3404–3419.

[113] F. Faber, A. Lindmaa, O. A. Von Lilienfeld, and R. Armiento *Int. J. Quantum Chem.* **115** (2015) 1094–1101, [arXiv:1503.0740].

[114] K. Fujimura, A. Seko, Y. Koyama, A. Kuwabara, I. Kishida, K. Shitara, C. A. J. Fisher, H. Moriwake, and I. Tanaka *Adv. Energy Mater.* **3** (2013) 980–985.

[115] G. Hautier, C. C. Fischer, A. Jain, T. Mueller, and G. Ceder *Chem. Mater.* **22** (2010) 3762–3767.

[116] M. Rupp, A. Tkatchenko, K.-R. Müller, V. Lilienfeld, and O. Anatole *Phys. Rev. Lett.* **108** (2012) 58301, [arXiv:1109.2618].

[117] D. B. Laks, L. G. Ferreira, S. Froyen, and A. Zunger *Phys. Rev. B* **46** (1992) 12587–12605, [1011.1669].

[118] J. W. D. Connolly and A. R. Williams *Phys. Rev. B* **27** (1983) 5169–5172.

[119] A. Van de Walle and G. Ceder *Rev. Mod. Phys.* **74** (2002) 11–45, [0106490].

[120] H. Y. Geng, M. H. F. Sluiter, and N. X. Chen, *Cluster expansion of electronic excitations: Application to fcc Ni-Al alloys*, in *J. Chem. Phys.*, vol. 122, p. 214706, American Institute of Physics, jun, 2005.

[121] G. D. Garbulsky and G. Ceder *Phys. Rev. B* **49** (1994) 6327–6330.

[122] A. Franceschetti, S. V. Dudiy, S. V. Barabash, A. Zunger, J. Xu, and M. Van Schilfgaarde *Phys. Rev. Lett.* **97** (2006) 047202.

[123] A. Franceschetti and A. Zunger *Nature* **402** (1999) 60–63.

[124] A. van de Walle *Nat. Mater.* **7** (2008) 455–458.

[125] G. L. W. Hart, V. Blum, M. J. Walorski, and A. Zunger *Nat. Mater.* **4** (2005) 391–394.

[126] L. J. Nelson, G. L. W. Hart, F. Zhou, and V. Ozoliš *Phys. Rev. B* **87** (2013) 035125, [arXiv:1208.0030].

[127] L. J. Nelson, V. Ozoliš, C. S. Reese, F. Zhou, and G. L. W. Hart *Phys. Rev. B Condens. Matter Mater. Phys.* **88** (2013) 155105, [arXiv:1307.2938].

[128] T. Mueller and G. Ceder *Phys. Rev. B Condens. Matter Mater. Phys.* **80** (2009) 024103.

[129] G. Kresse *Phys. Rev. B Condens. Matter Mater. Phys.* **54** (1996), no. 16 11169–11186.

[130] G. Kresse and D. Joubert *Phys. Rev. B Condens. Matter Mater. Phys.* **59** (1999) 1758–1775.

[131] S. H. Vosko, L. Wilk, and M. Nusair *Can. J. Phys.* **58** (1980) 1200–1211.

[132] Monkhors H. and J. Pack *Phys. Rev. B Solid State* **13** (1976) 5188–5192.

[133] M. Methfessel and A. T. Paxton *Phys. Rev. B Condens. Matter Mater. Phys.* **40** (1989) 3616–3621.

[134] P. E. Blöchl, O. Jepsen, and O. K. Andersen *Phys. Rev. B Condens. Matter Mater. Phys.* **49** (1994) 16223–16233.

[135] J. C. Thomas and A. Van der Ven *Phys. Rev. B Condens. Matter Mater. Phys.* **88** (2013) 214111.

[136] B. Puchala, M. Radin, N. S. H. Gunda, J. Goiri, L. Decolvenaere, A. R. Natarajan, and J. C. Thomas.

[137] A. Van der Ven, J. C. Thomas, Q. Xu, and J. Bhattacharya *Math. Comput. Simul.* **80** (2010) 1393–1410.

[138] A. D. Becke *J. Chem. Phys.* **140** (2014) 18A301.

[139] A. Jain, G. Hautier, C. J. Moore, S. Ping Ong, C. C. Fischer, T. Mueller, K. A. Persson, and G. Ceder *Comput. Mater. Sci.* **50** (2011) 2295–2310.

[140] O. Levy, J. Xue, S. Wang, G. L. W. Hart, and S. Curtarolo *Phys. Rev. B Condens. Matter Mater. Phys.* **85** (2012) 012201.

[141] S. Curtarolo, D. Morgan, and G. Ceder *Calphad Comput. Coupling Phase Diagrams Thermochem.* **29** (2005) 163–211, [0502465].

[142] G. Ghosh, A. van de Walle, and M. Asta *Acta Mater.* **56** (2008) 3202–3221.

[143] O. Levy, G. L. W. Hart, and S. Curtarolo *Phys. Rev. B* **81** (2010) 174106, [arXiv:1002.2822].

[144] S. B. Maisel, T. C. Kerscher, and S. Müller *Acta Mater.* **60** (2012) 1093–1098.

[145] P. J. Feibelman, B. Hammer, J. K. Nørskov, F. Wagner, M. Scheffler, R. Stumpf, R. Watwe, and J. Dumesic *J. Phys. Chem. B* **105** (2000) 4018–4025.

[146] F. Zhou, C. A. Marianetti, M. Cococcioni, D. Morgan, and G. Ceder *Phys. Rev. B Condens. Matter Mater. Phys.* **69** (2004) 201101, [0404631v2].

[147] Y. Zhang, G. Kresse, and C. Wolverton *Phys. Rev. Lett.* **112** (2014) 075502.

[148] V. Ozoliš, C. Wolverton, and A. Zunger *Phys. Rev. B Condens. Matter Mater. Phys.* **57** (1997), no. 11 19, [9710225].

[149] M. Sanati, L. G. Wang, and A. Zunger *Phys. Rev. Lett.* **90** (2003) 045502.

[150] R. V. Chepulskii and S. Curtarolo *Appl. Phys. Lett.* **99** (2011) 261902.

[151] S.-L. Shang, Y. Wang, D. E. Kim, C. L. Zacherl, Y. Du, and Z. K. Liu *Phys. Rev. B Condens. Matter Mater. Phys.* **83** (2011) 144204.

[152] S. V. Barabash, R. V. Chepulskii, V. Blum, and A. Zunger *Phys. Rev. B Condens. Matter Mater. Phys.* **80** (2009) 220201.

[153] R. V. Chepulskii, S. V. Barabash, and A. Zunger *Phys. Rev. B Condens. Matter Mater. Phys.* **85** (2012) 144201.

[154] D. E. Kim, J. E. Saal, L. Zhou, S.-L. Shang, Y. Du, and Z. K. Liu *Calphad Comput. Coupling Phase Diagrams Thermochem.* **35** (2011) 323–330.

[155] R. A. Oriani *Acta Metall.* **2** (1954) 608–615.

[156] R. A. Oriani and W. K. Murphy *Acta Metall.* **10** (1962) 879–885.

[157] R. A. Walker and J. B. Darby *Acta Metall.* **18** (1970) 1261–1266.

[158] R. Kessel, J. R. Beckett, and E. M. Stolper *Am. Mineral.* **86** (2001) 1003–1014.

[159] K. R. Coffey, M. a. Parker, and J. K. Howard *IEEE Trans. Magn.* **31** (1995), no. 6 2737–2739.

[160] K. Sato, B. Bian, and Y. Hirotsu *Jpn. J. Appl. Phys.* **39** (2000) L1121–L1123.

[161] D. Suess, T. Schrefl, R. Dittrich, M. Kirschner, F. Dorfbauer, G. Hrkac, and J. Fidler, *Exchange spring recording media for areal densities up to 10 Tbit/in 2*, in *J. Magn. Magn. Mater.*, vol. 290-291 PA, pp. 551–554, apr, 2005.

[162] R. Ferrando, J. Jellinek, and R. L. Johnston *Chem. Rev.* **108** (2008) 845–910.

[163] G. W. Qin, Y. P. Ren, N. Xiao, B. Yang, L. Zuo, and K. Oikawa *Int. Mater. Rev.* **54** (2009) 157–179.

[164] S. Takenoiri, S. Matsuo, and T. Fujihira *FUJI Electr. Rev.* **57** (2011), no. 2 32–36.

[165] A. Van der Ven, J. C. Thomas, Q. Xu, B. Swoboda, and D. Morgan *Phys. Rev. B Condens. Matter Mater. Phys.* **78** (2008) 104306.

[166] M. Born and K. Huang, *Dynamical theory of crystal lattices*. International series of monographs on physics. Clarendon Press, 1954.

[167] K. Parlinski, Z. Li, and Y. Kawazoe *Phys. Rev. Lett.* **78** (1997), no. 21 4063–4066.

[168] S. Wei and M. Y. Chou *Phys. Rev. Lett.* **69** (1992), no. 19 2799–2802, [0000135489].

[169] X. Gonze and C. Lee *Phys. Rev. B* **55** (1997), no. 16 10355–10367.

[170] A. van de Walle and G. Ceder *Rev. Mod. Phys.* **74** (2002) 11–45.

[171] M.-H. Chen, B. Puchala, and A. Van der Ven *Calphad* **51** (2015) 292–298.

[172] G. Inden, *The Mutual Influence of Magnetic and Chemical Ordering*, in *Mater. Res. Soc. Symp. Proc.* (L. Bennett, T. Massalki, and B. Gissen, eds.), vol. 19, pp. 175–188, Elsevier Science Publishing Co., Inc., 1983.

[173] C. Leroux *J. Phys. F Met. Phys.* **18** (1988), no. 9 2033.

[174] K. Momma and F. Izumi *J. Appl. Crystallogr.* **44** (2011) 1272–1276.

[175] J. M. Sanchez, J. L. Moran-Lopez, C. Leroux, and M. C. Cadeville *J. Phys. Condens. Matter* **1** (1999) 491–496.

[176] J. B. Newkirk, R. Smoluchowski, A. H. Geisler, and D. L. Martin *J. Appl. Phys.* **22** (1951), no. 3 290–298.

[177] P. S. Rudman and B. L. Averbach *Acta Metall.* **5** (1957), no. 2 65–73.

[178] M. Asta, R. McCormack, and D. de Fontaine *Phys. Rev. B Condens. Matter Mater. Phys.* **48** (1993), no. 2 748–766.

[179] G. Ceder *Comput. Mater. Sci.* **1** (1993) 144–150.

[180] M. Uhl and J. Kübler *Phys. Rev. Lett.* **77** (1996) 334–337.

[181] A. V. Ruban and I. A. Abrikosov *Reports Prog. Phys.* **71** (2008) 046501.

[182] P. Mori-Sánchez, A. J. Cohen, and W. Yang *Phys. Rev. Lett.* **100** (2008) 146401, [arXiv:0708.3688].

[183] A. Sakuma *J. Phys. Soc. Japan* **63** (1994), no. 8 3053–3058.

[184] L. Uba, S. Uba, V. Antonov, A. Yaresko, and R. Gontarz *Phys. Rev. B Condens. Matter Mater. Phys.* **64** (2001) 125105.

[185] O. Šipr, J. Minár, S. Mankovsky, and H. Ebert *Phys. Rev. B Condens. Matter Mater. Phys.* **78** (2008) 144403.

[186] S. Karoui, H. Amara, B. Legrand, and F. Ducastelle *J. Phys. Condens. Matter* **25** (2013) 056005, [1204.5845].

[187] A. V. Krukau, O. A. Vydrov, A. F. Izmaylov, and G. E. Scuseria *J. Chem. Phys.* **125** (2006) 224106.

[188] J. Heyd, G. E. Scuseria, and M. Ernzerhof *J. Chem. Phys.* **118** (2003), no. 18 8207–8215.

[189] A. Sorouri, W. M. C. Foulkes, and N. D. M. Hine *J. Chem. Phys.* **124** (2006) 64105.

[190] J. Paier, M. Marsman, K. Hummer, G. Kresse, I. C. Gerber, and J. G. Angyan *J. Chem. Phys.* **125** (2006) 249901.

[191] A. Stroppa, K. Termentzidis, J. Paier, G. Kresse, and J. Hafner *Phys. Rev. B Condens. Matter Mater. Phys.* **76** (2007) 32, [arXiv:0706.3615].

[192] J. H. Rose, J. R. Smith, and J. Ferrante *Phys. Rev. B Condens. Matter Mater. Phys.* **28** (1983) 1835–1845.

[193] F. Tran, D. Koller, and P. Blaha *Phys. Rev. B Condens. Matter Mater. Phys.* **86** (2012) 134406, [1209.6247].

[194] P. Heimann, E. Marschall, H. Neddermeyer, M. Pessa, and H. F. Roloff *Phys. Rev. B Solid State* **16** (1977) 2575–2583.

[195] S. F. Lin, D. T. Pierce, and W. E. Spicer *Phys. Rev. B Solid State* **4** (1971) 326–329.

[196] C. H. Cheng, C. T. Wei, and P. A. Beck *Phys. Rev.* **120** (1960) 426–436.

[197] G. E. Shoemake and J. A. Rayne *Phys. Lett. A* **26** (1968) 222–223.

[198] R. Küntzler, *Physics of Transition Metals, 1980*, in *Phys. Transit. Met. 1980* (P. Rhodes, ed.), (London), p. 397, Inst. of Physics, 1981.

[199] D. E. Eastman, F. J. Himpsel, and J. A. Knapp *Phys. Rev. Lett.* **44** (1980) 95–98.

[200] J. E. Moussa, P. A. Schultz, and J. R. Chelikowsky *J. Chem. Phys.* **136** (2012) 11, [arXiv:1205.4999].

[201] J. Tao, J. P. Perdew, V. Staroverov, and G. Scuseria *Phys. Rev. Lett.* **91** (2003) 146401.

[202] Y. Zhao and D. G. Truhlar *J. Chem. Phys.* **125** (2006) 194101.

[203] L. Schimka, J. Harl, and G. Kresse *J. Chem. Phys.* **134** (2011) 024116.

[204] M. Cococcioni and S. de Gironcoli *Phys. Rev. B Condens. Matter Mater. Phys.* **71** (2005) 18, [0405160].

[205] A. Pasquarello, M. S. Hybertsen, and R. Car *Lett. to Nat.* **396** (1998) 58–60.

[206] H. R. Rüter and R. Redmer *Phys. Rev. Lett.* **112** (2014) 145007.

[207] Y. Wang, W. D. Richards, S. P. Ong, L. J. Miara, J. C. Kim, Y. Mo, and G. Ceder *Nat Mater* **14** (2015) 1–23.

[208] A. P. Thompson, L. P. Swiler, C. R. Trott, S. M. Foiles, and G. J. Tucker *J. Comput. Phys.* **285** (2015) 316–330.

[209] M. S. Daw and M. I. Baskes *Phys. Rev. B* **29** (1984) 6443–6453.

[210] J. Tersoff *Phys. Rev. B* **37** (1988) 6991–7000.

[211] W. Zhong, D. Vanderbilt, and K. M. Rabe *Phys. Rev. Lett.* **73** (1994) 1861–1864, [9406049].

[212] K. M. Rabe and U. V. Waghmare *Phys. Rev. B* **52** (1995) 13236–13246, [9411006].

[213] W. Zhong, D. Vanderbilt, and K. M. Rabe *Phys. Rev. B* **52** (1995) 6301–6312, [9502004].

[214] T. S. Bush, J. D. Gale, C. R. A. Catlow, and P. D. Battle *J. Mater. Chem.* **4** (1994), no. 6 831.

[215] A. C. T. van Duin, S. Dasgupta, F. Lorant, and G. W. A. *J. Phys. Chem. A* **105** (2001) 9396–9409.

[216] R. Drautz and M. Fähnle *Phys. Rev. B* **69** (2004) 104404.

[217] R. Drautz, X. W. Zhou, D. A. Murdick, B. Gillespie, H. N. G. Wadley, and D. G. Pettifor, *Analytic bond-order potentials for modelling the growth of semiconductor thin films*, 2007.

[218] J. Bhattacharya and A. Van der Ven *Acta Mater.* **56** (2008), no. 16 4226–4232.

[219] J. C. Wojdeł, P. Hermet, M. P. Ljungberg, P. Ghosez, and J. Íñiguez *J. Phys. Condens. Matter* **25** (2013) 305401, [1301.5731].

[220] T. P. Senftle, S. Hong, M. M. Islam, S. B. Kylasa, Y. Zheng, Y. K. Shin, C. Junkermeier, R. Engel-Herbert, M. J. Janik, H. M. Aktulga, T. Verstraelen, A. Grama, and A. C. T. van Duin *npj Comput. Mater.* **2** (2016) 15011.

[221] A. Zunger, L. G. Wang, G. L. W. Hart, and M. Sanati *Model. Simul. Mater. Sci. Eng.* **10** (2002) 685–706.

[222] B. P. Burton and A. van de Walle *Calphad* **39** (2012) 97–103.

[223] D. Chang, M. H. Chen, and A. Van Der Ven *Chem. Mater.* **27** (2015) 7593–7600.

[224] B. Sadigh and P. Erhart *Phys. Rev. B* **86** (2012) 134204.

[225] J. Bhattacharya and A. Van der Ven *Phys. Rev. B Condens. Matter Mater. Phys.* **83** (2011) 144302.

[226] V. Vaithyanathan, C. Wolverton, and L. Chen *Acta Mater.* **52** (2004) 2973–2987.

[227] A. Zunger, *First-principles statisitcal mechanics of semiconductor alloys and intermetallic compounds*, in *Statics Dyn. Alloy Phase Trans- Form.*, p. 361. Springer US, 1994.

[228] P. D. Tepesch, G. D. Garbulsky, and G. Ceder *Phys. Rev. Lett.* **74** (1995) 2272–2275.

[229] V. Blum and A. Zunger *Phys. Rev. B Condens. Matter Mater. Phys.* **70** (2004) 155108.

[230] A. Van der Ven and G. Ceder *Phys. Rev. B Condens. Matter Mater. Phys.* **71** (2005) 054102.

[231] F. Zhou, T. Maxisch, and G. Ceder *Phys. Rev. Lett.* **97** (2006) 155704, [0612163].

[232] A. Seko, K. Yuge, F. Oba, A. Kuwabara, and I. Tanaka *Phys. Rev. B Condens. Matter Mater. Phys.* **73** (2006) 184117.

[233] B. P. Burton, A. Van De Walle, and U. Kattner *J. Appl. Phys.* **100** (2006), no. 11 113528.

[234] K. Yuge and R. Okawa *Intermetallics* **44** (2014) 60–63.

[235] J. G. Goiri and A. Van der Ven *Phys. Rev. B* **94** (2016) 094111.

[236] J. C. Thomas and A. Van der Ven *Phys. Rev. B Condens. Matter Mater. Phys.* **90** (2014) 224105.

[237] F. Ducastelle, *Order and Phase Stability in Alloys*, in *Interat. Potential Struct. Stab. SE - 14*, vol. 114, pp. 133–142. North-Holland, 1993.

[238] F. Livet *Acta Met.* **35** (1987), no. 12 2915–2919.

[239] R. Tibshirani *J. R. Stat. Soc. Ser. B (Statistical Methodol.* **73** (2011) 273–282, [11/73273].

[240] B. Efron, T. Hastie, I. Johnstone, R. Tibshirani, H. Ishwaran, K. Knight, J. M. Loubes, P. Massart, D. Madigan, G. Ridgeway, S. Rosset, J. I. Zhu, R. A. Stine, B. A. Turlach, S. Weisberg, T. Hastie, I. Johnstone, and R. Tibshirani *Ann. Stat.* **32** (2004) 407–499, [0406456].

[241] James Glosli; Michael Plischke *Can. J. Phys.* **61** (1983), no. 11 1515–1527.

[242] Z. W. Lu, S.-H. Wei, A. Zunger, S. Frota-Pessoa, and L. G. Ferreira *Phys. Rev. B* **44** (1991) 512–544.

[243] V. Gerold and J. Kern *Acta Metall.* **35** (1987) 393–399.

[244] K. Mosegaard and A. Tarantola *J. Geophys. Res.* **100** (1995) 12431–12447.

[245] K. Mosegaard and M. Sambridge *Inverse Probl.* **18** (2002) R29–R54.

[246] J. Albert and R. H. Swendsen *Phys. Procedia* **57** (2014) 99–103.

[247] A. Cerezo, P. H. Clifton, M. J. Galtrey, C. J. Humphreys, T. F. Kelly, D. J. Larson, S. Lozano-Perez, E. A. Marquis, R. A. Oliver, G. Sha, K. Thompson, M. Zandbergen, and R. L. Alvis *Mater. Today* **10** (2007) 36–42.

[248] K. Sohlberg, T. J. Pennycook, W. Zhou, and S. J. Pennycook *Phys. Chem. Chem. Phys.* **17** (2015) 3982–4006.

[249] M. M. J. Treacy, J. M. Gibson, L. Fan, D. J. Paterson, and I. McNulty *Reports Prog. Phys.* **68** (2005) 2899–2944.

[250] S. Cadars, A. Lesage, N. Hedin, B. F. Chmelka, and L. Emsley *J. Phys. Chem. B* **110** (2006) 16982–91.

[251] G. D. Garbulsky and G. Ceder *Phys. Rev. B* **49** (1994) 6327–6330.

[252] F. Pedregosa, G. Varoquaux, A. Gramfort, V. Michel, B. Thirion, O. Grisel, M. Blondel, P. Prettenhofer, R. Weiss, V. Dubourg, J. Vanderplas, A. Passos, D. Cournapeau, M. Brucher, M. Perrot, and E. Duchesnay *J. Mach. Learn. Res.* **12** (2011) 2825–2830, [arXiv:1201.0490].

[253] M. Advani and S. Ganguli *Phys. Rev. X* **6** (2016) 031034.

[254] T. Graf, C. Felser, and S. S. Parkin *Prog. Solid State Chem.* **39** (2011), no. 1 1–50.

[255] M. Yin, J. Hasier, and P. Nash, *A review of phase equilibria in Heusler alloy systems containing Fe, Co or Ni*, sep, 2016.

[256] M. B. Stearns *J. Magn. Magn. Mater.* **15-18** (1980) 301–302.

[257] J. Kübler, A. R. Williams, and C. B. Sommers *Phys. Rev. B* **28** (1983) 1745–1755, [0411737v2].

[258] Y. Kurtulus, R. Dronskowski, G. D. Samolyuk, and V. P. Antropov *Phys. Rev. B* **71** (2005) 014425, [0406588].

[259] Y. Kurtulus, M. Gilleßen, and R. Dronskowski *J. Comput. Chem.* **27** (2006) 90–102.

[260] I. Galanakis, P. H. Dederichs, and N. Papanikolaou *Phys. Rev. B* **66** (2002) 174429.

[261] I. Galanakis, P. Mavropoulos, and P. H. Dederichs *J. Phys. D. Appl. Phys.* **39** (2006) 765–775, [0510276].

[262] S. Ishida, S. Fujii, S. Kashiwagi, and S. Asano *J. Phys. Soc. Japan* **64** (1995) 2152–2157.

[263] E. aolu, L. M. Sandratskii, P. Bruno, and I. Galanakis *Phys. Rev. B* **72** (2005) 184415.

[264] A. C. Pebley, P. E. Fuks, T. M. Pollock, and M. J. Gordon *J. Magn. Magn. Mater.* **419** (2016) 29–36.

[265] A. Pebley, E. Decolvenaere, T. M. Pollock, and M. J. Gordon *Nanoscale*.

[266] I. Galanakis, P. H. Dederichs, and N. Papanikolaou *Phys. Rev. B* **66** (2002) 134428.

[267] I. Galanakis and P. Dederichs, eds., *Half-metallic Alloys*, vol. 676 of *Lecture Notes in Physics*. Springer Berlin Heidelberg, Berlin, Heidelberg, 2005.

[268] A. R. Williams, V. L. Moruzzi, C. D. Gelatt, and J. Kübler *J. Magn. Magn. Mater.* **31-34** (1983) 88–94.

[269] E. aiolu, L. M. Sandratskii, and P. Bruno *Phys. Rev. B - Condens. Matter Mater. Phys.* **77** (2008) 064417, [0712.0158].

[270] E. aiolu, L. M. Sandratskii, and P. Bruno *Phys. Rev. B - Condens. Matter Mater. Phys.* **70** (2004) 024427, [0404162].

[271] E. aiolu, L. M. Sandratskii, and P. Bruno *J. Phys. Condens. Matter* **17** (2005) 995–1001, [0504679].

[272] S. Picozzi, A. Continenza, and A. J. Freeman *Phys. Rev. B* **66** (2002) 094421.

[273] Z. P. Shi, P. M. Levy, and J. L. Fry *Phys. Rev. B* **49** (1994) 15159–15178.

[274] K. Azumi and J. E. Goldman *Phys. Rev.* **93** (1954) 630–631.

[275] W. Selke *Phys. Rep.* **170** (1988), no. 4 213–264.

[276] D. de Fontaine and J. Kulik *Acta Metall.* **33** (1985), no. 2 145–165.

[277] G. Inden, *Atomic Ordering*. 2005.

[278] V. L. Deringer, A. L. Tchougréeff, and R. Dronskowski *J. Phys. Chem. A* **115** (2011) 5461–5466.

[279] S. Maintz, V. L. Deringer, A. L. Tchougréeff, and R. Dronskowski *J. Comput. Chem.* **34** (2013) 2557–2567.

[280] S. Maintz, M. Esser, and R. Dronskowski *Acta Phys. Pol. B* **47** (2016), no. 4 1165–1175.

[281] R. Dronskowski and P. E. Blöchl *J. Phys. Chem.* **97** (1993) 8617–8624.

[282] S. Maintz, V. L. Deringer, A. L. Tchougréeff, and R. Dronskowski *J. Comput. Chem.* **37** (2016) 1030–1035.

[283] L. Schimka, R. Gaudoin, J. Klimeš, M. Marsman, and G. Kresse *Phys. Rev. B - Condens. Matter Mater. Phys.* **87** (2013) 214102.

[284] I. Galanakis and P. Mavropoulos *J. Phys. Condens. Matter* **19** (2007) 315213, [0610827].

[285] D. P. Rai, Sandeep, A. Shankar, A. P. Sakhya, T. P. Sinha, R. Khenata, M. P. Ghimire, and R. K. Thapa *Mater. Res. Express* **3** (2016) 075022.

[286] E. E. Fullerton, J. S. Jiang, and S. D. Bader *J. Magn. Magn. Mater.* **200** (1999) 392–404.

[287] E. Decolvenaere, M. J. Gordon, R. Seshadri, and A. Van der Ven *Phys. Rev. B* **In Submiss** (2017).

[288] D. D. Fontaine *Solid State Phys. - Adv. Res. Appl.* **47** (1994), no. C 33–176.

[289] M. Y. Lavrentiev, D. Nguyen-Manh, and S. L. Dudarev *Phys. Rev. B* **81** (2010) 184202.

[290] R. Singer and M. Fähnle *J. Math. Phys.* **47** (2006), no. 11 113503.

[291] S. DeWitt, E. Solomon, A. Natarajan, V. Araullo-Peters, S. Rudraraju, L. Aagesen, B. Puchala, E. Marquis, A. van der Ven, K. Thornton, and J. Allison *Acta Mater.* **136** (2017) 378–389.

[292] C. Domb and M. F. Sykes *Phys. Rev.* **128** (1962) 168–173.

[293] F. Izumi and K. Momma *Solid State Phenom.* **130** (2007) 15–20.

[294] D. Voss, *Synopsis: Beyond Shake and Bake*, 2012.

Some Thoughts

I entered graduate school in 2012 intending to do experiments. I was going to use microplasmas to grow exotic nanostructured materials — I would "tame lightning". At the time, I considered myself unfit for theory — programming scared me, quantum mechanics terrified me, and all I could recall from thermo was that "fugacity is an abstraction of an abstraction". When I found myself with a plan of research involving experiments *and* simulation, I was told that the simulations would be quick, they would be easy, and I would be back in the lab constructing my own reactor in no time.

I have no regrets about the outcome, even if where I am now was not where I could've imagined going. Five years, three classes on density functional theory, >10,000 lines of python, and >1,000,000 CPU hours later, I can't imagine doing anything *but* theory and simulation. I (think I) understand what a k-point is. I make terrible DFT jokes. Magnetism has begun to make sense in some small way. There is still so much that I don't know, but it no longer terrifies me. I know that I can learn. And I look forward to learning it!

Sitting down and writing this thesis, trying to make a unified story from a disjointed jumble of projects that seem to have each come up by happenstance, has involved a great deal of reflection. Becoming a PhD has involved both a great quantity of growth, and a greater part of luck. I will be proud to call myself a Doctor. But I will also be sad, as it will mean my time at UCSB has ended. Working with the Van der Ven and Gordon Groups, as well as the professors and students of IRG 3, has been an honor and a privilege. Collaborating with my mentors at Sandia has been an invaluable gift. Making the friends I've made has been a joy. When I leave, it will be with the strangest mixture of heartbreak and excitement, because I know that the future is bright, it is an irreversible transition[2].

[2]As a friend once said about graduating: "You can visit, but it will never be Home again"

Thank you for reading.